

**STRUCTURAL ENGINEERING OF HALIDE
PEROVSKITES AND THEIR ASSOCIATION WITH
ORGANICS FOR OPTOELECTRONIC
APPLICATIONS**

**A Thesis Submitted to
the Graduate School of Engineering and Sciences of
İzmir Institute of Technology
in Partial Fulfillment of the Requirements for the Degree of**

DOCTOR OF PHILOSOPHY

in Materials Science and Engineering

by

Hürriyet YÜCE ÇAKIR

**June 2022
İZMİR**

ACKNOWLEDGMENTS

I would like to first thank my advisor, Prof. Mustafa M. Demir, for his guidance and support. I would like to acknowledge my co-advisor Assoc. Prof. Kıvılcım Yüksel Aldoğan and my thesis committee members; Assoc. Prof. Umut Adem, Prof. Hasan Şahin, Prof. Ceylan Zafer, and Prof. Cem Tozlu for their support and useful feedback.

I would also like to thank Prof. Juan-Pablo Correa-Baena for introducing me to the exciting world of solar cells and providing an international research atmosphere.

I thank Yenal Yalçınkaya for his collaboration and insightful discussion.

I would like to express my gratitude to all Demir Lab (IZTECH) and Energy Materials Lab (Georgia Tech) members for their friendship, support, and collaboration.

Finally, I would like to thank my parents for their understanding (a lot!), love, and incredible support. Last but not the least; my special thanks go to my lovely husband, Özgür. His excitement about my achievements has always increased my motivation during my Ph.D. studies. Nothing I have done would have been as pleasant without his support, his optimistic outlook, and of course his love!

ABSTRACT

STRUCTURAL ENGINEERING OF HALIDE PEROVSKITES AND THEIR ASSOCIATION WITH ORGANICS FOR OPTOELECTRONIC APPLICATIONS

Halide perovskites show great potential for next-generation optoelectronic applications due to their unique photophysical properties with low production costs. However, their stability issues still prevent their commercialization on a large scale. The main objective of this dissertation is to understand the additive engineering strategy to improve the quality of halide perovskite films and nanocrystals for solar cells and light-emitting diodes. There are two sections to this dissertation: The first section focuses on halide perovskite films and solar cells while the second one focuses on halide perovskite nanocrystals and white light-emitting diodes.

In the first section of this dissertation, in Chapter 2-3, the improvement of Sn-Pb and methylammonium-free Pb-based halide perovskite films by additives are investigated. The suppression of defects via additives is demonstrated through structural, elemental, and optical analyses. The improved performance of perovskite solar cells by decreasing defects is also shown. In Chapter 4-5, the change in stability and optical properties of the halide perovskite nanocrystals by means of additive engineering and their applications in white light-emitting diode are studied.

The results in this dissertation represent a new approach to improving the structural and photophysical properties of halide perovskites and introduce a new perspective of additive engineering method in the field of halide perovskite-based optoelectronic applications.

ÖZET

HALOJENÜR PEROVSKİTLERİN YAPISAL MÜHENDİSLİĞİ VE OPTOELEKTRONİK UYGULAMALAR İÇİN ORGANİKLER İLE İLİŞKİSİ

Halojenür perovskitler, düşük üretim maliyetleri ve eşsiz fotofiziksel özellikleri sebebiyle yeni nesil optoelektronik uygulamalar için büyük bir potansiyel göstermektedir. Ancak, kararlılık sorunları hala büyük ölçekte ticarileşmelerini engellemektedir. Bu tezin temel amacı, güneş hücreleri ve ışık yayan diyotlar için halojenür perovskit filmlerin ve nanokristallerin kalitesini artırmak için katkılama stratejisini anlamaktır. Bu tezin iki bölümü vardır: İlk bölüm halojenür perovskit filmler ve güneş hücrelerine odaklanırken, ikinci bölüm halojenür perovskit nanokristaller ve beyaz ışık yayan diyotlara odaklanmaktadır.

Bu tezin ilk bölümünde, Bölüm 2-3'te, Sn-Pb ve metilamonyum içermeyen Pb esaslı halojenür perovskit filmlerin katkılama ile iyileştirilmesi araştırılmaktadır. Katkılama ile kusurların bastırılması, yapısal, elementel ve optik analizler ile gösterilmektedir. Kusurları azaltarak perovskit güneş hücrelerinin performansının arttığı da gösterilmiştir. Bölüm 4-5'te beyaz ışık yayan diyot uygulamaları için katkılama yoluyla halojenür perovskit nanokristallerin kararlılığı ve optik özelliklerindeki değişim incelenmiştir.

Bu tezdeki sonuçlar, halojenür perovskitlerin yapısal ve fotofiziksel özelliklerini iyileştirmeye yönelik yeni bir yaklaşımı temsil etmekte ve halojenür perovskite dayalı optoelektronik uygulamalar alanında yeni bir katkılama mühendisliği yöntemi perspektifi sunmaktadır.

Dedicated to my lovely husband, Özgür...

TABLE OF CONTENTS

LIST OF FIGURES	viii
LIST OF TABLES	xii
LIST OF ABBREVIATIONS	xiii
CHAPTER 1. INTRODUCTION	1
1.1. Overview of Perovskite Materials	1
1.2. Crystal Structure of Metal Halide Perovskites.....	1
1.3. Optoelectronic Properties of Metal Halide Perovskites.....	4
1.4. Physics of Solar Cells	7
1.4.1. Shockley-Queisser Limit	8
1.4.2. Solar Cell Parameters.....	9
1.5. Halide Perovskites in White Light Emitting Diodes.....	12
CHAPTER 2. EFFECTS OF STRONTIUM ADDITIVE ON LEAD-TIN PEROVSKITE FILMS.....	14
2.1. Introduction.....	14
2.2. Experimental Section	15
2.3. Results and Discussion	16
2.3.1. Morphological and Structural Analysis	16
2.3.2. Optical Analysis.....	19
2.3.3. Elemental Analysis	20
2.4. Conclusion	25
CHAPTER 3. IMPROVING PERFORMANCE OF PEROVSKITE SOLAR CELLS WITH ALKALINE EARTH METAL ADDITIVES.....	26
3.1. Introduction.....	26
3.2. Experimental Section	27
3.3. Results and Discussion	29
3.3.1. Morphological and Structural Analysis	29
3.3.2. Optical Analysis.....	32

3.3.3. Elemental Analysis	33
3.3.4. Solar Cell Characterization	37
3.4. Conclusion	41
CHAPTER 4. IMPROVING PHOTOPHYSICAL PROPERTIES OF PEROVSKITE NANOCRYSTALS FOR WHITE LIGHT EMITTING DIODES	42
4.1. Introduction	42
4.2. Experimental Procedure	43
4.3. Results and Discussion	46
4.3.1 Elemental Analysis	46
4.3.2. Morphology of CsPbBr ₃ NCs	48
4.3.3. Structural and Optical Properties of CsPbBr ₃ NCs.....	49
4.3.4. Morphology of Mn ²⁺ :CsPb(Br,Cl) ₃ NCs	52
4.3.5. Structural and Optical Properties of Mn ²⁺ :CsPb(Br,Cl) ₃ NCs.....	53
4.3.6. White Light Generation by Using Perovskite NCs.....	55
4.4. Conclusion	56
CHAPTER 5. INCREASED STABILITY OF PEROVSKITE NANOCRYSTALS BY LIGAND ENGINEERING	57
5.1. Introduction	57
5.2. Experimental Procedure	58
5.3. Results and Discussion	59
5.3.1. Morphological and Structural Analysis	59
5.3.2. Optical Analysis.....	61
5.4. Conclusion	65
CHAPTER 6. CONCLUSION	66
REFERENCES.....	68
APPENDICES	
APPENDIX A. SUPPORTING INFORMATION	90

LIST OF FIGURES

<u>Figure</u>	<u>Page</u>
Figure 1.1. Crystal structure of the perovskite ABX ₃ form.....	2
Figure 1.2. Tolerance factor of ABX ₃ (B=Pb, X=I) perovskites with different sizes of A monovalent cations	3
Figure 1.3. a) Tilted octahedra b) optimal cubic, and c) stretched octahedra of ABX ₃ perovskite structures	3
Figure 1.4. Shockley-Queisser efficiency for PSCs bandgap energy ranges of the Pb- and Pb/Sn-based perovskites.....	4
Figure 1.5. a) The colors under UV light, b) PL spectra, and c) absorption spectra of CsPbX ₃ NCs depending on the halide composition.....	5
Figure 1.6. Band structure of metal halide perovskites through the hybridization of lead and iodine orbitals	6
Figure 1.7. Defect states in conventional semiconductors and halide perovskites.....	6
Figure 1.8. a) Layer structure of a typical perovskite solar cell and b) required band alignment of the layers.....	8
Figure 1.9. J-V curve of a solar cell under illumination	10
Figure 1.10. For model 1, a) schematic diagram of WLED designed using halide perovskite with a UV chip b) perovskite-based WLED by using UV chip, and c) electroluminescent spectra of the WLED. For model 2, d) schematic representation of WLED designed using halide perovskite with a blue chip and e) electroluminescence spectra of the WLED.....	12
Figure 2.1. a) SEM images (Scale bar: 2 μm) and b) Grain size distributions of (FASnI ₃) _{0.8} (MAPbBr ₃) _{0.2} perovskite films with the addition of 0%, 0.1%, 0.5%, 1.0%, 2.0%, and 5.0% SrI ₂	17
Figure 2.2. a) XRD pattern and b) microstrain and Urbach energies of the perovskite films with varying SrI ₂ concentrations.	19
Figure 2.3. Optical properties of the films. a) UV-vis absorption, b) Tauc Plot, and (c) PL spectra.	20
Figure 2.4. XPS survey spectra of the perovskite films.....	21
Figure 2.5. XPS spectra of a) Pb 4f b) Sn 3d c) I 3d, and d) Br 3d in perovskite films.	22

<u>Figure</u>	<u>Page</u>
Figure 2.6. XPS spectra of Sn 3d peaks of a) pristine b) 0.1% Sr c) 0.5% Sr d) 1.0% Sr e) 2.0% Sr and f) 5.0% SrI ₂ perovskite films.	22
Figure 2.7. Atomic ratio of Sn ⁴⁺ /Sn ²⁺ at different SrI ₂ concentrations.	23
Figure 2.8. XPS spectra of O 1s peaks of a) pristine, b) 0.1%, c) 0.5%, d) 1.0%, e) 2.0%, and f) 5.0% SrI ₂ added perovskite films.	24
Figure 2.9. Atomic ratio (%) of metal oxide / [(C-OH) + (C=O)] for each sample as calculated from deconvoluted from XPS measurements.	25
Figure 3.1. Images of a) perovskite solar cell pixels and b) measurement setup for the solar cell performance.	29
Figure 3.2. SEM images of a) pristine, b) Sr ²⁺ and c) Ca ²⁺ added perovskite with the concentration of 0.1%, 0.5%, and 1.0%. d) Illustration of the proposed microstructure of perovskite films. The left and right sides indicate pristine and Sr ²⁺ /Ca ²⁺ added perovskite films, respectively. Excess metal halides at the grain boundaries are indicated by green spheres. Bar size is 500 nm for all micrographs.	31
Figure 3.3. XRD signals of a) Sr ²⁺ and b) Ca ²⁺ additive perovskite series. (c) Calculated microstrains of the perovskite films.	31
Figure 3.4. Tauc plots of a) Sr ²⁺ and b) Ca ²⁺ additive perovskite series by using absorption spectra. PL spectra of c) Sr ²⁺ and d) Ca ²⁺ additive perovskite series.	33
Figure 3.5. XPS survey spectra of a) Sr ²⁺ and b) Ca ²⁺ additive perovskite series. XPS spectra of c) Pb 4f/Sr 3d and d) Ca 2p core levels of the perovskite films.	34
Figure 3.6. XPS spectra of Cs 3d, I 3d and Pb 4f for a) Sr ²⁺ and b) Ca ²⁺ additive perovskite series. The energy shifts in the different elemental core level peaks of c) Sr ²⁺ and d) Ca ²⁺ perovskite films.	35
Figure 3.7. XPS spectra of C 1s, N 1s, and O 1s for a) Sr ²⁺ and b) Ca ²⁺ additive perovskite series.	36
Figure 3.8. Solar cell parameters of Voc, FF, Jsc, and PCE for a) Sr ²⁺ and b) Ca ²⁺ additive series. c) n-i-p architecture of fabricated solar cells. d) <i>J-V</i> curves of PSCs for additive series with the pristine.	38
Figure 3.9. Calculated solar cell parameters of Voc, FF, Jsc, and PCE from reverse and forward <i>J-V</i> curves for a) Sr ²⁺ and b) Ca ²⁺ PSCs.	40

<u>Figure</u>	<u>Page</u>
Figure 3.10. Hysteresis indices in the J-V curves of a) Sr ²⁺ and b) Ca ²⁺ additive series.	41
Figure 4.1. Illustration of a) CsPbBr ₃ and b) Sr ²⁺ :CsPbBr ₃ perovskite NCs synthesis with their images under daylight and UV light.	44
Figure 4.2. Illustration of a) Mn ²⁺ :CsPb(Br,Cl) ₃ and b) 2%Sr ²⁺ :Mn ²⁺ :CsPb(Br,Cl) ₃ perovskite NCs synthesis with their images under daylight and UV light. .	45
Figure 4.3. Pictures of perovskite NCs/PMMA composite films under daylight and UV light.	46
Figure 4.4. Actual Sr ²⁺ and Pb ²⁺ percentages depending on the added Sr ²⁺ concentrations for CsPbBr ₃ NCs as obtained by ICP-MS.	47
Figure 4.5. a) Illustration of Sr ²⁺ -doping into CsPbBr ₃ crystal lattice and STEM images of b) 0%, c) 1%, d) 2%, e) 5%, and f) 10% Sr ²⁺ doped CsPbBr ₃ NCs. All inset in each figure shows NC size distribution in the relevant sample. Bar size is 50 nm.	49
Figure 4.6. a) XRD patterns, b) lattice parameters, c) microstrain values obtained by W-H plot, d) PL/Absorption spectra, e) TRPL plot, and f) PLQY distribution of pristine and Sr ²⁺ :CsPbBr ₃ NCs.	50
Figure 4.7. Tauc plots of a) pristine, b) 1%, c) 2%, d) 5%, and e) 10% Sr ²⁺ :CsPbBr ₃ NCs with bandgap of 2.39 eV.	50
Figure 4.8. PL emissions of pristine, 1%, 2%, 5%, and 10% Sr ²⁺ :CsPbBr ₃ NCs.	51
Figure 4.9. STEM images of a) Mn ²⁺ :CsPb(Br,Cl) ₃ and b) 2% Sr ²⁺ :Mn ²⁺ :CsPb(Br,Cl) ₃ NCs. Bar size is 50 nm.	52
Figure 4.10. a) XRD patterns, b) the comparisons of XRD signal positions for CsPbBr ₃ , Mn ²⁺ :CsPb(Br,Cl) ₃ and Sr ²⁺ :Mn ²⁺ :CsPb(Br,Cl) ₃ perovskite NCs c) microstrain and lattice constant parameters. d) PL/Absorption and 2%Sr ²⁺ :Mn ²⁺ :CsPb(Br,Cl) ₃ NCs.	53
Figure 4.11. Tauc plots of a) Mn ²⁺ :CsPb(Br,Cl) ₃ (E _g = 2.70 eV) and b) 2% Sr ²⁺ :Mn ²⁺ :CsPb(Br,Cl) ₃ NCs (E _g = 2.69 eV).	54
Figure 4.12. PL spectra of WLEDs based on a) 0% and 2% Sr ²⁺ doped CsPbBr ₃ and Mn ²⁺ :CsPb(Br,Cl) ₃ drop casted films; b) corresponding CIE coordinates.	55
Figure 5.1. Illustration of a) CsPbI ₃ and b) 5% 4-HBA:CsPbI ₃ perovskite NCs synthesis with their images under daylight and UV light.	59

<u>Figure</u>	<u>Page</u>
Figure 5.2. STEM images of perovskite samples, for a) 0%, b) 2.5%, c) 5.0%, d) 10%, and e) 20% 4-HBA perovskites. Bar size is 200 nm.	60
Figure 5.3. a) XRD patterns and b) relative shift in the peak at 28.5° of perovskite NC samples.	61
Figure 5.4. a) Tauc plots, b) PL spectra, c) Urbach energy comparison, and d) TRPL data of CsPbI ₃ NCs with various 4-HBA amounts.	62
Figure 5.5. Images of CsPbI ₃ NCs with varying 4-HBA concentrations after ethanol exposure under daylight and UV light. The vials are ordered with the concentration of 4-HBA at 0%, 2.5%, 5%, 10%, and 20%, respectively from left to right.	63
Figure 5.6. PL spectra of CsPbI ₃ NCs with various 4-HBA amounts after ethanol exposure depending on time.	64
Figure 5.7. Absorption spectra of CsPbI ₃ NCs with various 4-HBA amounts depending on ambient air exposure time.	64

LIST OF TABLES

<u>Table</u>	<u>Page</u>
Table 3.1. Atomic percentage in sample for element to Pb ratio (Z:Pb)	34
Table 3.2. The shifts in binding energies of the perovskite films for Cs 3d, I 3d, and Pb 4f XPS spectra.	35
Table 3.3. Average device parameters of pristine, Sr ²⁺ , and Ca ²⁺ additive PSCs for reverse and forward scan	39
Table 4.1. Actual Sr ²⁺ / Pb ²⁺ +Sr ²⁺ for Sr ²⁺ :CsPbBr ₃ NCs (determined by ICP-MS).....	47
Table 4.2. Actual mole ratio (%) of Sr ²⁺ and Mn ²⁺ / Pb ²⁺ +Mn ²⁺ +Sr ²⁺ (determined by ICP-MS) and Br ⁻ /Cl ⁻ (determined by IC) for Mn ²⁺ :CsPb(Br,Cl) ₃ NC samples.....	48

LIST OF ABBREVIATIONS

CIE	International Commission on Illumination
ETL	Electron Transporting Layer
FF	Fill Factor
HTL	Hole Transporting Layer
Jsc	Short Circuit Current Density
NC	Nanocrystal
PCE	Power Conversion Efficiency
PL	Photoluminescence
PLQY	Photoluminescence Quantum Yield
SEM	Scanning Electron Microscopy
SQ	Shockley-Queisser
TRPL	Time-Resolved Photoluminescence
UV	Ultraviolet
WLED	White Light Emitting Diode
XPS	X-ray Photoelectron Spectroscopy
XRD	X-ray Diffraction
Voc	Open Circuit Voltage

CHAPTER 1

INTRODUCTION

1.1. Overview of Perovskite Materials

Perovskite is a material having the same chemical formula with calcium titanium oxide (CaTiO_3) that was discovered in the Ural Mountains in 1839 by the mineralogist Gustav Rose, and it was named after the mineralogist Lev A. Perovski.¹ The term of perovskite materials is generally attributed to all compounds which have the same structure as CaTiO_3 . The general formula of the perovskites is ABX_3 . In this structure, both A and B are monovalent and divalent cations, respectively and X is an anion. Inorganic perovskite oxides (e.g., CaTiO_3 , BaTiO_3 , LaMnO_3 , etc.) have been widely investigated during the last several decades due to their varied uses in superconductive ferroelectric²⁻⁴ and solid oxide fuel cell⁵ applications.

Halide perovskites are distinguished from oxide perovskites by the presence of halide anions rather than oxide anions in the X site of the ABX_3 structure. Owing to the photophysical properties of halide perovskites, there are a large number of works on the applications of halide perovskites, such as photovoltaics, light-emitting diodes (LEDs), lasers and photodetectors⁶.

1.2. Crystal Structure of Metal Halide Perovskites

In three dimensional (3D) metal halide perovskites with the chemical formula ABX_3 , A site is one/composed of monovalent organic methylammonium (MA^+), formamidinium (FA^+), or inorganic Cs^+/Rb^+ cations; B is a metal cation (e.g., Pb^{2+} , Sn^{2+}); the X site is occupied by the halides which are I^- , Br^- , or Cl^- (Figure 1.1).⁷⁻⁹ In the perovskite structure, the A site cations are surrounded by an octahedral cage of $[\text{PbX}_6]^{4-}$ ¹⁰. Depending on the unit cell lengths of the perovskite crystal structure, different phases of the perovskite structure are formed.

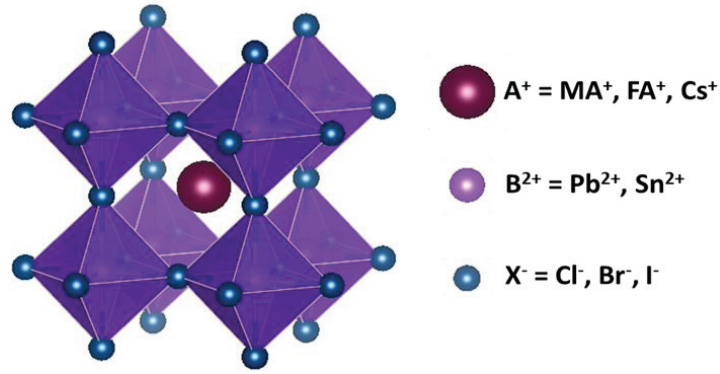


Figure 1.1. Crystal structure of the perovskite ABX_3 form. (adapted from¹⁰)

Goldschmidt tolerance factor (t) can be used to predict the structural stability of the 3D halide perovskite structure. This prediction is based on the ionic radii of all A, B, and X ions in the ABX_3 structure as in the following formula¹¹:

$$t = \frac{r_A + r_X}{\sqrt{2}(r_B + r_X)} \quad (1.1)$$

Based on this prediction, a stable 3D perovskite structure is usually formed when the t value is between 0.8 and 1.0^{12,13} and the phases of halide perovskites around boundary t values are meta-stable (Figure 1.2). For example, the tolerance factor of the most widely studied $MAPbI_3$ is 0.912¹³. However, in contrast to the non-perovskite phases, the perovskite phases of the $FAPbI_3$ and $CsPbI_3$ are meta-stable at room temperature. Many techniques have been devised to stabilize these metastable perovskite phases, allowing them to be used in optoelectronic applications^{14–16}. The most common strategy is to tune the tolerance factor by alloying A cations. For instance, $Cs_{1-x}FA_xPbI_3$ is a more stable perovskite phase¹⁷ compared to its pure Cs^+ or FA^+ based counterparts. Additionally, alloyed two or three Cs^+ , MA^+ , and FA^+ cations in the A site improve photophysical properties and stability of 3D lead halide perovskites and the highest performances achieved by perovskite solar cells are based on alloyed A-cations^{18,19}.

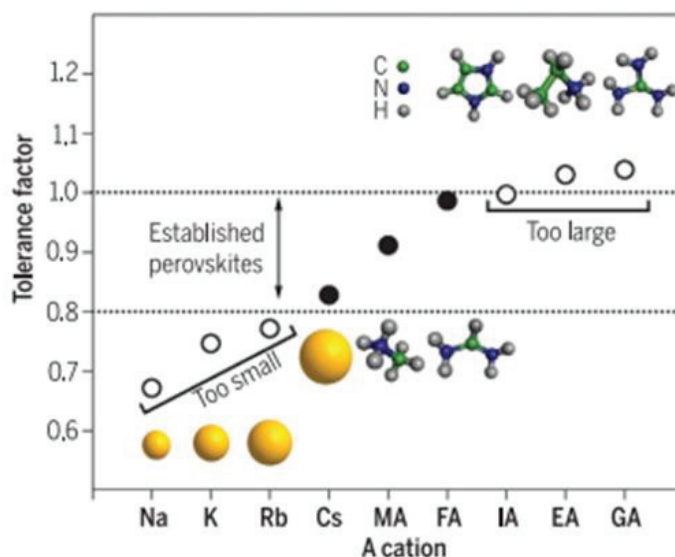


Figure 1.2. Tolerance factor of ABX_3 ($B=Pb$, $X=I$) perovskites with different sizes of A monovalent cations.²⁰

The sizes of the A-cations influence the tilting of BX_6 octahedra in perovskite structure and determine the availability of a stable perovskite. In addition, the size of the A cations alters the optoelectronic properties of the perovskites. Smaller A-cations lead to perovskite cages with octahedral tilting (Figure 1.3a), while larger A-cations cause the formation of a stretched BX_6 octahedra and perovskite cages (Figure 1.3c). Smaller or larger A-cations create structural distortions in perovskites and distort the ideal cubic symmetry (Figure 1.3b).

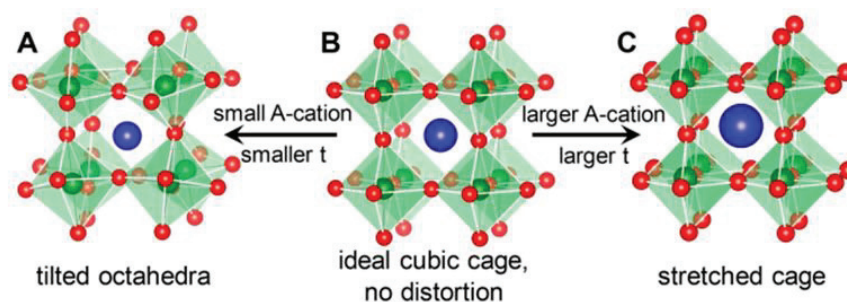


Figure 1.3. a) Tilted octahedra b) optimal cubic, and c) stretched octahedra of ABX_3 perovskite structures.¹³

1.3. Optoelectronic Properties of Metal Halide Perovskites

Metal halide perovskites are impressive materials for optoelectronic applications. Extreme interest in understanding the fundamental material properties and photo-physics of halide perovskite materials has contributed to the development of extremely effective optoelectronics based on perovskites over the last decade or so. There are some main characteristics that differentiate perovskites from the other semiconductors, such as bandgap tunability²¹, high charge carrier mobility ($> \sim 10 \text{ cm}^2\text{V}^{-1}\text{s}^{-1}$)²², long diffusion length ($> 1 \mu\text{m}$)²¹, low exciton binding energy (between 2-50 meV)²³, and low trap density ($< 10^{16} \text{ cm}^{-3}$)²¹.

In case a semiconductor material has a tunable bandgap, it provides a large range of applications in optoelectronic devices. The bandgap of the perovskites can be tuned by changing elemental composition, stoichiometry, and the dimensionality of the perovskites. As an absorber material, halide perovskites have a wide range of bandgap energy by mixing the B-site cation and the X site anion (Figure 1.4 and Figure 1.5). The bandgap energies of perovskites between 1.3 eV and 1.6 eV are suitable for single-junction perovskite solar cells²⁴. Wider bandgap energies between 1.6 eV and 1.7 eV are appropriate for the top cell in tandem devices with silicon bottom cells^{25,26} while narrow bandgap energy ($\sim 1.25 \text{ eV}$)²⁷, obtained in Sn-based perovskite cells is suitable for perovskite/perovskite tandem solar cells.

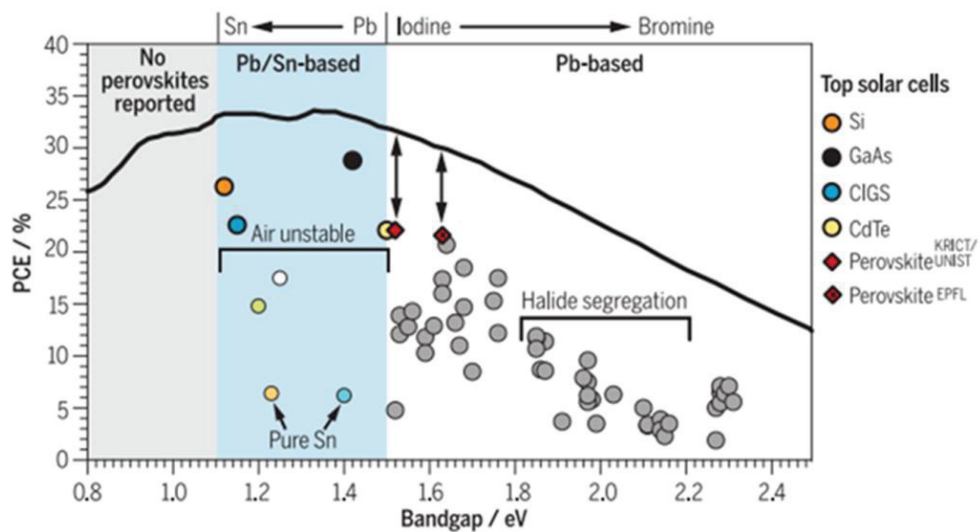


Figure 1.4. Shockley-Queisser efficiency for PSCs bandgap energy ranges of the Pb- and Pb/Sn-based perovskites.²⁰

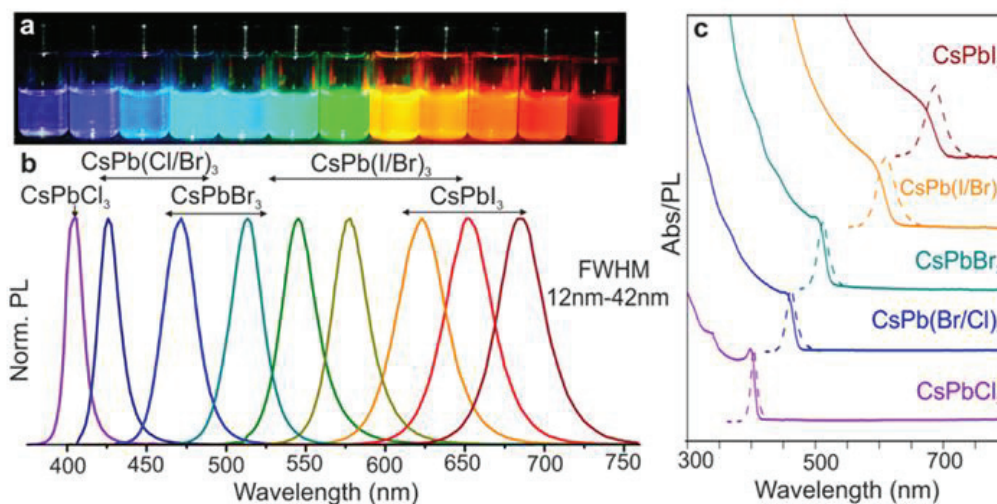


Figure 1.5. a) The colors under UV light, b) PL spectra, and c) absorption spectra of CsPbX₃ NCs depending on the halide composition.²⁸

Halide perovskite nanocrystals (NCs) also show incredible optoelectronic properties. Lead halide perovskite NCs stand in the spotlight of optoelectronic materials due to their tunable optical properties, high photoluminescence quantum yield (PLQY), low full-width half-maxima of photoluminescence, and high defect tolerance²⁹. These promising properties enabled their usage in applications such as solar cells, light-emitting devices, solar concentrators, photodetectors, etc.^{30–32}

As shown in Figure 1.5, the absorption and light emission wavelengths of the CsPbX₃ NCs are mainly determined by the X anion which can be Cl⁻, Br⁻, or I⁻. Furthermore, all the wavelengths of the visible color spectrum can be achieved via mixing these halides. Amongst these materials, CsPbI₃ NCs draw attention owing to their low energy bandgap and red-light emission. However, CsPbI₃ NCs suffer from thermodynamically unstable unlike their CsPbBr₃ and CsPbCl₃ counterparts which construct some challenges in the synthesis and fabrication processes. This situation leads to the requirement of better methods like composition or ligand engineering to fabricate CsPbI₃ NCs³³.

The band structure illustration of metal halide perovskites is given in Figure 1.6. The conduction band of the perovskite material is formed from the antibonding orbitals of the hybridization of Pb 6p orbitals and the outer p orbitals of the halogens while the valence band is formed from the antibonding states of the hybridization of Pb 6s orbitals and the halide p orbitals⁹.

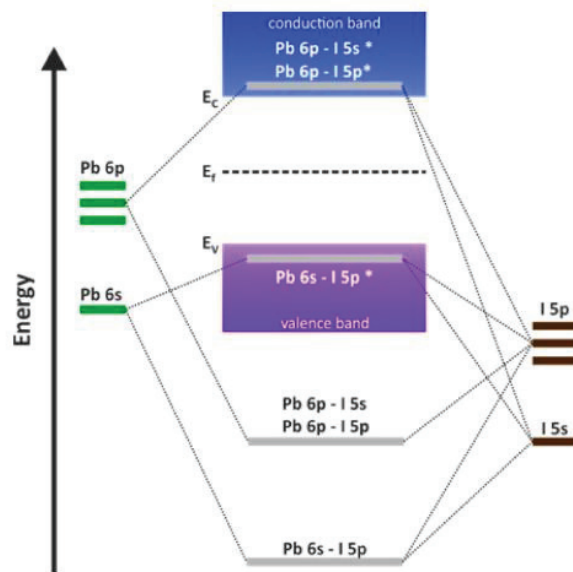


Figure 1.6. Band structure of metal halide perovskites through the hybridization of lead and iodine orbitals.⁹

One significant feature of halide perovskites is their defect tolerance which is their ability to stay unaffected or mildly affected by a large density of defects. Compared to conventional semiconductors, the energy states of the defects in halide perovskite materials are close to or within the electronic bands of the perovskites themselves, causing the formation of mostly shallow trap states^{34,35} (Figure 1.7).

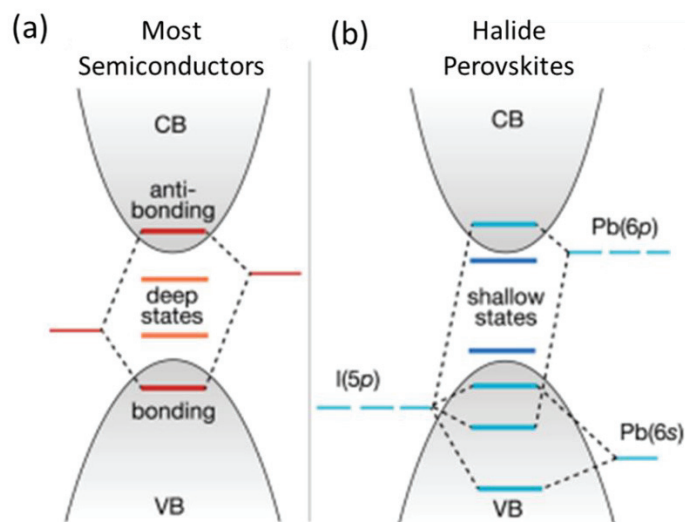


Figure 1.7. Defect states in conventional semiconductors and halide perovskites.³⁵

One other important prospect of metal halide perovskite NCs is their high PLQY. Contrary to conventional quantum dots (QD), metal halide perovskite NCs can show high PLQY values even in absence of a passivating shell³⁶. Inorganic CsPbX₃ NCs show PLQY values between 50-95%. This is the result of the defect tolerance of these materials and the formation of mostly shallow trap states³⁷ (Figure 1.7b).

One aspect that affects the optoelectronic properties of metal halide perovskite NCs is quantum confinement. Quantum confinement is observed in metal halide perovskite NCs when the size of the NCs is below the Bohr exciton radius in at least one dimension. In this case, the absorption and PL of the NCs blue-shift due to their increased bandgap energies. Furthermore, the confinement of the charge carriers causes an increment in exciton binding energy due to lowered screening of Coulomb interaction. In CsPbX₃ NCs, the Bohr exciton radii are ultra-low as they are 5 nm, 7 nm, and 12 nm for CsPbCl₃, CsPbBr₃, and CsPbI₃, respectively³⁸. Furthermore, the absorption edge observed in metal halide perovskite films and nanocubes evolves into a blue-shifted exciton peak^{39,40}. However, this band structure adjustment via quantum confinement comes at a price which is the lower PLQY for higher quantum confinement. This is the result of reduced dielectric screening of charge carriers that causes incomplete polaron formation. Furthermore, high quantum confinement causes charge carriers to be more fragile against defects and polar optical phonons⁴¹.

1.4. Physics of Solar Cells

A perovskite solar cell consists of a cathode, an electron transport layer (ETL), a solar absorber layer, a hole transport layer (HTL), and an anode. In order to minimize the charge recombination and maximize the charge transport, ETL-perovskite (absorber layer)-HTL must form heterojunctions between layers. When perovskite as the solar absorber layer is exposed to the light, electrons are excited to the conduction band, i.e. electron-hole pairs are formed. Due to the band alignment of the solar cell layers, electrons are transported with ETL while holes are transported with HTL as shown in Figure 1.8.

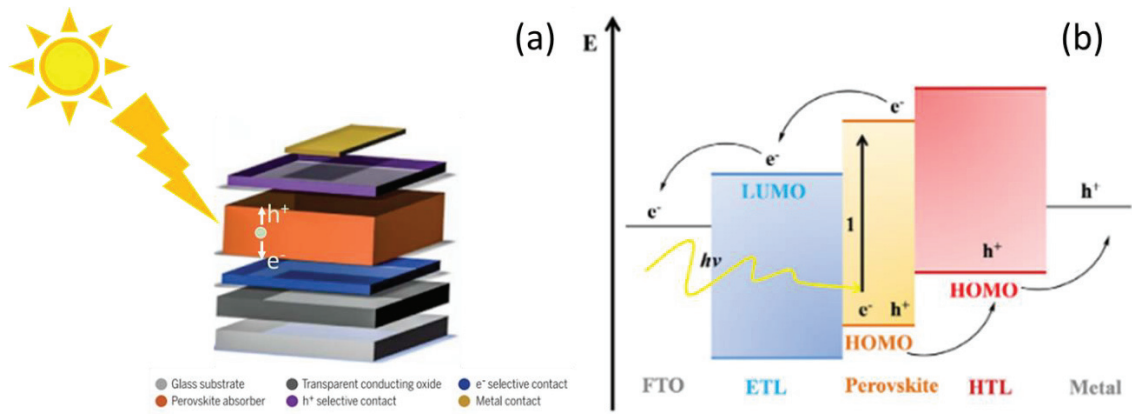


Figure 1.8. a) Layer structure of a typical perovskite solar cell²⁰ and b) required band alignment of the layers.⁴²

1.4.1. Shockley-Queisser Limit

In 1961, Shockley and Queisser determined the limits of photovoltaic solar cells by utilizing the basic thermodynamic principle of detailed balance. The result of their study is referred to as the Shockley-Queisser (SQ) model and the limit for the photovoltaic energy conversion according to the SQ model is referred to as the SQ limit. There are some assumptions that were used for the determination of the SQ limit. These assumptions are as follows⁴³:

1. One electron-hole pair is generated per absorbed photon.
2. Absorptivity of photons changes from 0 to 1 at E_g .
3. Carrier temperature is equal to the cell temperature and ambient temperature.
4. Charge recombination only occurs radiatively.
5. Ohmic losses are not present.

In the SQ model, the cell exchanges electrons with the external electrical circuit and heat with a temperature reservoir to keep constant the cell temperature. Here, the cell temperature is kept constant and it is equal to the ambient temperature without solar excitation. In this model, the photon absorber is a semiconductor material and has conduction and valence bands. Under light illumination, the electrons in the valence band are excited to the conduction band, leaving a hole in the valence band. This electron-hole pair is considered free charges and they can move in their respective bands. In order to generate free charge carriers, the energy of the incident photon must be higher than the

energy of the bandgap of the absorber material. When electron and hole recombination happens, the energy released is assumed as a photon.

According to the SQ model, there are no losses due to contacts, photon absorption, temperature, or non-radiative recombination. With these assumptions, the SQ model gives a certain output for an ideal solar cell in ideal conditions. The maximum solar cell efficiency can be obtained with a 1.1 eV bandgap and cannot exceed 30% efficiency. However subsequent calculations involving global solar spectra (AM1.5G) and surface back mirror resulted in maximum efficiency of 33.7% for a bandgap of 1.34 eV⁴⁴.

1.4.2. Solar Cell Parameters

There are four main parameters to measure in order to quantify the properties of a perovskite solar cell⁴⁵:

- Open circuit voltage, V_{OC}
- Short circuit current density, J_{SC}
- Fill factor, FF
- Power conversion efficiency (PCE), η

These parameters are determined via a J-V measurement of a solar cell. J-V measurement is carried out by applying an external bias and measuring the current with or without light. The measurements performed with a solar simulator under light illumination are called light measurements, whereas the measurements performed without light are called dark measurements. Furthermore, the external bias is applied as forward bias and backward bias and when the forward J-V curve does not overlap the backward J-V curve, hysteresis behavior is said to be observed. Figure 1.9 shows an example of a J-V curve for solar cells.

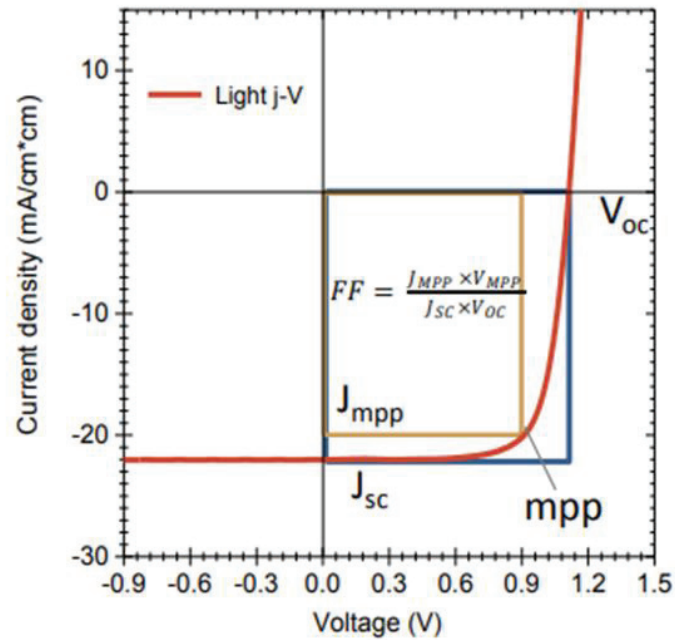


Figure 1.9. J-V curve of a solar cell under illumination.⁴⁶

Open circuit voltage describes the maximum potential difference a solar cell generates at zero current. The main limitation of V_{OC} is the bandgap of the absorber material. The higher the bandgap of the absorber layer leads to the higher the potential difference between the electrodes. Therefore the higher bandgap of the perovskite causes higher V_{OC} . Moreover, the band alignment of the other layers in a perovskite solar cell also affects V_{OC} . The real V_{OC} value of a perovskite solar cell is determined by the potential difference between the conduction band minimum of the electron transporting layer (ETL) and the valence band maximum of the hole transporting layer (HTL). One other factor affecting V_{OC} is the defects in the perovskite layer. Mid-gap and trap states within the perovskite layer can reduce V_{OC} . However, the effect of defects on V_{OC} is relatively small since the trapped charge carriers have long lifetimes. Therefore, the synthesis of high quality perovskite film can increase V_{OC} . In addition, any factor that reduces the perovskite film quality such as humidity can also reduce V_{OC} .

A short circuit current (I_{SC}) describes the current a solar cell proves at short circuit conditions with zero electric load. I_{SC} is dependent on the number of photo-excited charge carriers. In principle, the more light is absorbed by the perovskite, the higher the number of charge carriers. The higher number of charge carriers causes a higher I_{SC} . As the bandgap of the perovskite decreases, I_{SC} increases. Similarly, any factor that increases the number of charge carriers causes higher I_{SC} values. The area of the solar cell affects the

photo-excitation area, thus the number of charge carriers. Therefore, a larger solar cell area means a larger I_{SC} value. Similarly, energy and the intensity of the excitation light source also affect the generation of charge carriers. Therefore, light sources with higher energy light and/or higher light intensities cause larger I_{SC} values. The collection probability, which is the probability of photon absorption by the solar cell to generate a charge carrier, also affects I_{SC} . Furthermore, since the collection probability is highly dependent on the absorption coefficient (fixed) and the thickness of the absorber layer, the thickness of the perovskite can enhance J_{SC} . In addition to absorption, reducing the reflection of light at solar cell surfaces is also a crucial task for larger I_{SC} values. In order to achieve that, the pathway of light to the perovskite layer must be as transparent as possible. It is not the number of photo-generated charge carriers but the number of charge carriers reaching the electrodes which is the main factor that affects J_{SC} . Therefore, any charge trapping effects such as defects or interfaces may cause recombination of charges and thus cause J_{SC} losses. Due to that, all layers in the solar cell including the perovskite layer must be as defect-free as possible and contacts between the layers must not lack quality.

The fill factor (FF) determines the maximum power output of a solar cell. It is determined by the ratio of actual power output the solar cell gives and the theoretical maximum power output from V_{OC} and I_{SC} . The squareness of the I-V curve gives information about the FF. As the area below the I-V curve increases the maximum power output and thus FF increases. FF is also dependent on shunt resistance which is the resistance of the solar cell against internal short circuit currents. Shunt resistance is usually related to defects and pinholes in the layers that might cause direct transport of charges between ETL and HTL.

Power conversion efficiency (PCE) can be described as the outcome of all other values of a solar cell that was described above. It is the efficiency of converting light into electricity via solar cells. It is defined as the ratio of the power output of the solar cell compared to the energy of the incident light.

$$P_{max} = V_{OC} I_{SC} FF \quad (1.2)$$

$$\eta = \frac{V_{OC} I_{SC} FF}{P_{in}} \quad (1.3)$$

1.5. Halide Perovskites in White Light Emitting Diodes

For perovskite based white light emitting diodes (WLEDs), there are two models with CsPbX_3 perovskite NCs as a PL-converter. The first one is the combinations of red/green/blue (RGB) perovskites excited by a UV-LED⁴⁷ and the second one is the combinations of red/green (RG) perovskites excited by a blue-LED⁴⁸. Here, in CsPbX_3 perovskite NCs, the halogen content X-site anions can be tuned to alter emission color, e.g., the CsPbI_3 , CsPbBr_3 , and CsPbCl_3 NCs can be used for the red (~ 1.7 eV), green (~ 2.4 eV), and blue (~ 3.0 eV) emitters, respectively³⁸. For the first model, an ultraviolet (UV) chip/LED is used in order to excite the emitters absorbing the UV light and this model converts the UV light to multicolor luminescence or a broadband white light as shown in Figure 1.10a-c. For the second model, a blue chip/LED is coated with green and red emitter materials as shown in Figure 1.10d-e. The blue light generated from the blue LED is absorbed by emitter materials and these emitter materials are used to form a complementary color resulting in a white light⁴⁹.

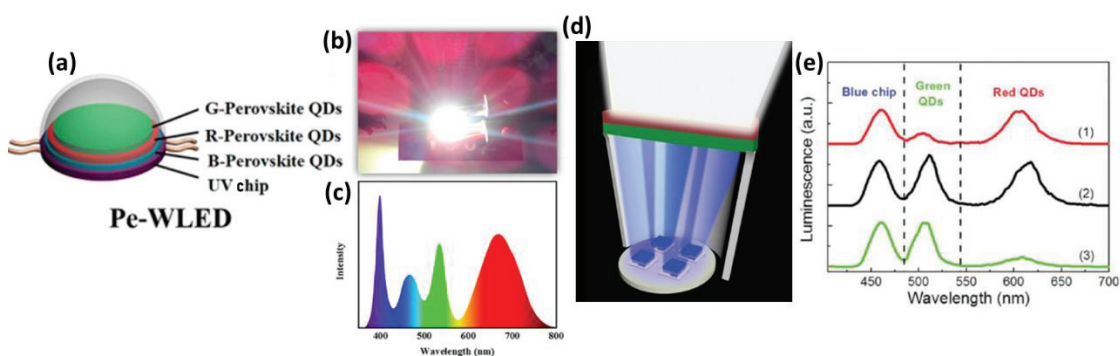


Figure 1.10. For model 1, a) schematic diagram of WLED designed using halide perovskite with a UV chip b) perovskite-based WLED by using UV chip, and c) electroluminescent spectra of the WLED⁵⁰. For model 2, d) schematic representation of WLED designed using halide perovskite with a blue chip and e) electroluminescence spectra of the WLED.⁴⁸

Despite the excellent optoelectronic properties of metal halide perovskites, the anion exchange reactions and unstable nature of the perovskites are issues for devices in real-life applications. In order to resolve these kinds of problems, poly(methyl methacrylate) (PMMA) polymer is used to hinder the contact of halide perovskites with each other resulting in ion exchange⁴⁸. In this way, ethyl cellulose with its passivation

effect was used to increase the stability of perovskite materials. Similarly, poly(maleic anhydride-alt-1-octadecene) is used as a protective layer⁵¹ in order to improve the stability of perovskites. Metal ion doping is also another strategy to increase stability and the PLQY by passivating the surface defects^{52,53}.

An ideal white light source requires an emitting both continuous and broad spectrum similar to natural sunlight with the international commission on illumination (CIE) coordinates of (0.33, 0.33)⁵⁴. The following indicators are routinely used to measure the quality of a white light source: Color rendering index (CRI) and luminous efficiency (η).

Color Rendering Index, CRI: CRI has a scale of 0 to 100 and CRI measures the ability of a light source to restore the true color of a lighted object in comparison to natural light⁵⁵. In order to obtain the exact color of an object, the light source requires a higher CRI⁵⁵.

Luminous Efficiency (η): Luminous efficiency shows energy conversion efficiency, which is measured in lumens per watt and can be represented using the equation⁵⁵.

$$\eta = \frac{\Phi_v}{P_l} \quad (1.4)$$

where Φ_v and P_l stand for the total luminous flux and total lamp power input (or radiant power emitted).

CHAPTER 2

EFFECTS OF STRONTIUM ADDITIVE ON LEAD-TIN PEROVSKITE FILMS

2.1. Introduction

Organic-inorganic halide perovskites have been identified as very promising materials for photovoltaic applications in terms of their strong benefits of low cost and simple process²⁰. Perovskite solar cells (PSCs) have achieved power conversion efficiency (PCE) exceeding 25%, which makes them a viable option for future photovoltaic applications⁵⁶. However, lead halide perovskites suffer from the toxicity of lead, which has led some researchers to investigate lead-free halide perovskites. Environmentally friendly alternatives include Sn⁵⁷ and Ge⁵⁸. Mixed halide metals, such as Sn/Ge⁵⁹, Pb/Sn⁶⁰, or Pb/Sn/Cu⁶¹ in perovskite structure are also possible. Organic-inorganic lead halide perovskites exhibit bandgap tunability by modifying the X-site portion of the ABX₃ structure⁶². The X-site is typically a halide, including Cl, Br, and I, or a combination of them. Modification of the X-site can result in bandgaps values in the range of 1.48-2.3 eV⁶³. In order to achieve the optimum bandgap of ~ 1.4 eV for single junction solar cells regarding the Shockley-Queisser model⁶⁴, another option is to modify the B-metal site in the perovskite structure by mixing Sn and Pb since the ratio of Pb:Sn has the ability to change the bandgap of the perovskites ranging from 1.17 to 1.55 eV⁶⁵.

However, the main problem of Sn perovskites is the oxidation of Sn²⁺ to Sn⁴⁺ when exposed to ambient conditions⁶⁶. Considering the standard redox potentials (E_o) of Sn and Pb oxidation states, E_o (Sn²⁺/Sn⁴⁺) = 0.15 V and E_o (Pb²⁺/Pb⁴⁺) = 1.67 V, Sn oxidation is more likely to occur in comparison to the oxidation of Pb²⁺ to Pb⁴⁺⁶⁷. The oxidation results in the disruption of structural stability and charge neutrality of the perovskite⁶⁸. Sn²⁺ in the perovskite structure is oxidized to Sn⁴⁺ and this oxidation plays a role on the structure as a p-type dopant by a self-doping process^{69,70}. SnF₂ additives reduce the generation of Sn⁴⁺ in Sn perovskite films^{71,72}. In order to overcome the oxidation problem of Sn-based perovskites, the addition of SnF₂ to Sn-based perovskite as a reducing agent enhances photovoltaic device performance⁷³⁻⁷⁵. According to some

reports, the excessive addition of SnF₂ leads to pinhole formation of Sn-based perovskite films and negatively affects photovoltaic performance in the devices^{76,77}. The addition of SnF₂ does not lead to a significant change in crystal lattice parameters, and the substitution of F⁻ ion for I⁻ or Br⁻ ions does not take place since F⁻ has a smaller ionic radius compared to that of I⁻/ Br⁻ ions⁷⁸. While these works have shown that Sn perovskite can be more stable, there is still much more to understand about the mechanisms and how other compounds prevent degradation.

In this work (Yuce H. et al.)⁷⁹, it is aimed to show the stabilization of the Sn-based perovskite by the addition of SrI₂, which is expected to suppress Sn²⁺ oxidation to the Sn⁴⁺ state. The Sr²⁺ (118 pm)⁸⁰ ion has a similar ionic radius to those of Sn²⁺ and Pb²⁺ (119 pm)⁸¹ and Sr²⁺ ions were added at different concentrations to a solution containing (FASnI₃)_{0.8}(MAPbBr₃)_{0.2}. The composition was chosen to exploit the optimal bandgap of ~1.4 eV, ideal for single junction solar cells. This work aims to understand the effects of the SrI₂ additive with various concentrations of 0.1, 0.5, 1.0, 2.0, and 5.0 mol % on Sn/Pb based perovskite films. The structural and optical properties of the perovskite films with SrI₂ additive were investigated. X-ray Diffraction (XRD) was employed to investigate the structural features of perovskite films. By using the Williamson-Hall plot from the XRD and Urbach energy calculations, a doping and passivation mechanism caused by SrI₂ addition to the perovskite is proposed. Moreover, a detailed X-ray photoelectron spectroscopy (XPS) elemental analysis in order to examine the effects of SrI₂ on Sn²⁺ oxidation was performed. It is shown that SrI₂ additive causes to reduce Sn²⁺ oxidation by XPS and improves optical properties of the perovskite film. These results are important in the quest to stabilize and passivate the Sn perovskite films to achieve less toxic photo-absorbers with an optimal bandgap and improved stability in single junction perovskite solar cells.

2.2. Experimental Section

Chemicals: Methylammonium bromide (CH₃NH₃Br) and formamidinium iodide (CH(NH₂)₂I) were purchased from Dyenamo. Tin iodide (SnI₂) and strontium iodide (SrI₂) were purchased from Alfa Aesar. Dimethylformamide (DMF) and dimethyl sulfoxide (DMSO) were purchased from Acros Organics. Lead bromide (PbBr₂) was bought from TCI America, and tin fluoride (SnF₂) was obtained from Sigma Aldrich.

Perovskite Film Fabrication: 2.5×2.5 cm² glass and FTO glass substrates were ultrasonically cleaned first in 2% Hellmanex solution, then in DI water, acetone, and IPA, in that order. SnI₂ and PbBr₂ powders were dissolved separately in DMF/DMSO (4:1) solvent, and 10% mol SnF₂ was added to the SnI₂ solution. FAI and MABr powders were dissolved in SnI₂ and PbBr₂ solutions, respectively. By mixing the solutions, 1.2M (FASnI₃)_{0.8}(MAPbBr₃)_{0.2} final perovskite solution was obtained. Finally, SrI₂ powder was dissolved in DMSO at a concentration of 1.0 M, and added to the final perovskite solution to achieve molar ratios (SrI₂ to Pb/Sn) of 0.1, 0.5, 1.0, 2.0, and 5.0%. The perovskite solution was deposited on glass substrates by two-step spin coating: first at 1000 rpm for 5 s and then at 4000 rpm for 30 s. During spin coating, 2.5-3 mL of diethyl ether were dropped on the substrate 20 s after the program started. Then, the films were annealed at 100 °C for 15 min in a nitrogen filled glove box.

Perovskite Film Characterization: Morphology of perovskite film surface was obtained by using the Hitachi SU-8230 scanning electron microscope (SEM). XRD measurements were carried out using a Malvern PANalytical Empyrean using Cu K α radiation (λ = 1.54 nm) with a scan step size of 0.0131°. The chemical states of elements were probed by an XPS spectrometer (Thermo K-Alpha XPS) equipped using an Al K α (1486.6 eV) monochromatic source with a spot size of 400 μ m. Absorption spectra were collected by using the Carry 500 UV-Visible-NIR spectrophotometer. Hyperspectral PL (Photon etc) measurements were performed by exciting with Nd:YAG laser light samples at 532 nm. SEM and XPS analyses were carried out on perovskite coated on FTO/glass substrates, whereas XRD and optical measurements were performed on perovskite coated on glass substrates. SnI₂ reference film for XRD measurements was coated under the same conditions with perovskite films on glass substrates.

2.3. Results and Discussion

2.3.1. Morphological and Structural Analysis

To observe the effects of the SrI₂ addition into the Sn/Pb perovskite films on morphology, SEM images of the perovskite films with (ranging from 0.1% to 5.0%) and without SrI₂ are shown in Figure 2.1a. The films have different morphologies, with smaller grains forming with increasing SrI₂ concentration. Even though small grains are

formed, and the number of small grains increases, there are still large grains present in the structure for concentrations up to 2.0% SrI₂. When increasing the concentration from 2.0% to 5.0%, all large grains completely disappear, and it is clearly seen that the area and the number of pinholes significantly decrease. Beyond grain size reduction, the area of pinholes also shrinks with the increasing SrI₂ amount in the films. The size of pinholes becomes smaller with increasing SrI₂ concentrations, and this trend is similar to the change in the size of perovskite grains. The reason for the pinholes could be stress due to fast crystal growth in the film during the annealing process which changes with the addition of SrI₂⁸⁰. The distributions of grain size for the perovskite films are shown in Figure 2.1b. Grain sizes of the perovskite film without SrI₂ vary from nearly 1.6 μm to 0.2 μm. When adding 0.1% SrI₂ to the perovskite, the average grain size of the perovskite films decreased from ~707 nm to ~572 nm, and the distribution narrowed significantly. When the SrI₂ additive concentration in the film was 0.5% and above, it was observed that the grain sizes further decreased, with the 5.0% SrI₂ showing ~157 nm average grains.

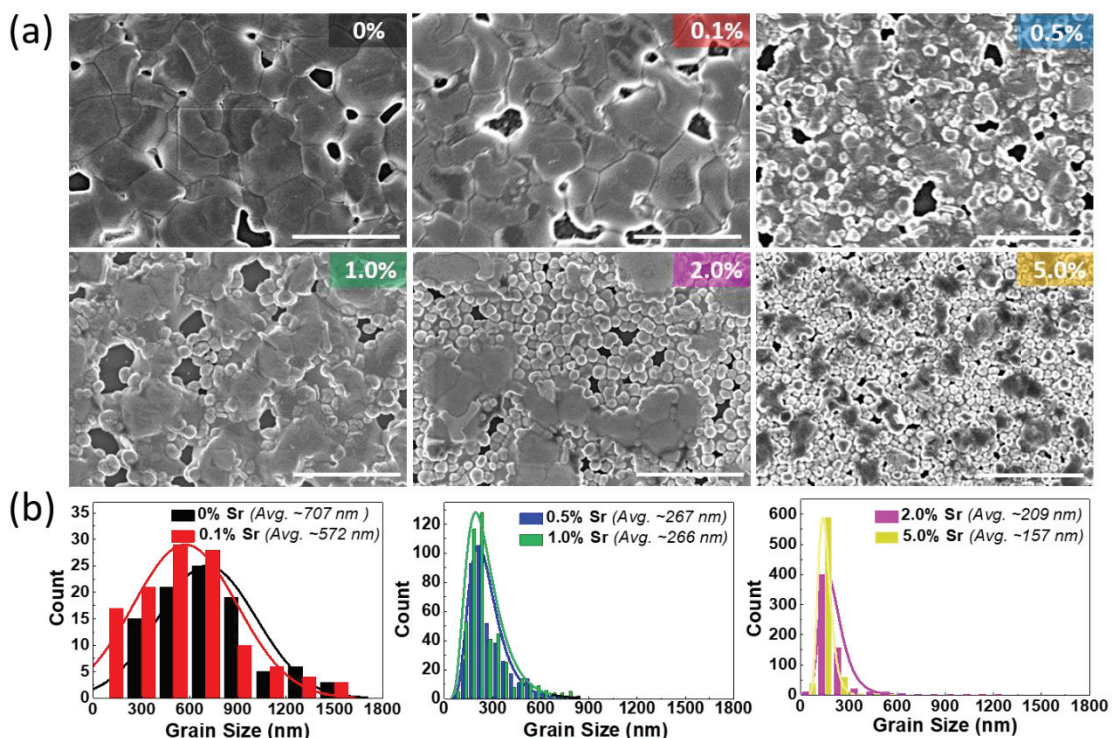


Figure 2.1. a) SEM images (Scale bar: 2 μm) and b) Grain size distributions of (FASnI₃)_{0.8}(MAPbBr₃)_{0.2} perovskite films with the addition of 0%, 0.1%, 0.5%, 1.0%, 2.0%, and 5.0% SrI₂.

In order to understand the impact of the SrI₂ additive on the crystal structure of the (FASnI₃)_{0.8}(MAPbBr₃)_{0.2} perovskite, XRD analyses were carried out and the results are shown in Figure 2.2a. The signals at 2θ of 14.1, 24.6, 28.4, 31.9, 40.7, and 43.3° correspond to the characteristic diffraction peaks of (FASnI₃)_{0.8}(MAPbBr₃)_{0.2} perovskite^{82,83}. In addition, the pristine and 0.1% SrI₂ perovskite films include excess SnI₂ signals at 2θ of 12.6, 25.5, 38.7, and 52.5°. When adding SrI₂ to the perovskite, no new signal was observed, which is indicative of no additional crystalline phase formation. The addition of 0.1% SrI₂ is shown to decrease the excess SnI₂ signal. At 0.5% SrI₂, the excess SnI₂ signature completely disappears and the perovskite film exhibits the highest XRD peak intensity for the perovskite phase. When the concentration of SrI₂ is increased from 0.5% to 5.0%, the intensities of the XRD peaks for the perovskite structure decrease. The XRD results show that the SrI₂ additive significantly improves the perovskite peak intensity until 0.5% concentration. The crystallite size calculated by the Williamson–Hall method of the perovskites is also increased by the addition of SrI₂ until 0.5% (Figure S2.2).

In an effort to further understand the SrI₂ additive-perovskite mechanism, microstrain within the perovskite lattice using the Williamson-Hall plot method, which utilizes full width at half-maximum (FWHM) of XRD signals was calculated. In addition, Urbach energies for the samples were calculated for comparison of structural disorder in the perovskite films as shown in Figure 2.2b. All microstrain (Figure S2.1 and Table S2.1) and Urbach energy (Figure S2.3 and Table S2.2) calculations with Urbach tail plots are shown in detail in Appendix A. When SrI₂ is introduced in the perovskite precursor solution at low concentrations (below 0.5%) an increase in microstrain was observed up to 0.5%, most possibly because of the distortion of the lattice due to Sr²⁺ incorporation. Above 0.5% SrI₂, the decrease in microstrain could be the result of the segregation of SrI₂ and lack of Sr²⁺ incorporation. Similar behavior of SrI₂ related to doping and segregation of Sr²⁺ was observed by Phung et al. with the introduction of Sr²⁺ at low concentrations to the MAPbI₃ perovskite solution⁸⁴. They observed Sr²⁺ segregation beyond 0.2% SrI₂ added MAPbI₃ while we observed the segregation beyond 0.5% SrI₂ added (FASnI₃)_{0.8}(MAPbBr₃)_{0.2} perovskite films. The reason for this difference probably originated from the rapid crystallization of Sn-based perovskites⁸⁵ and entrapment of Sr²⁺ ions within the lattice. However, a high concentration of SrI₂ additive may result in stress in the perovskite lattice. This can be a result of the segregation of dopants at the grain boundaries since the higher doping concentrations cause a disturbance in the long-range

crystallographic ordering⁸⁶. The Urbach energy decreases with Sr²⁺ doping and reaches the lowest value when $\leq 0.5\%$, which is ascribed to a decrease in electronic defect concentration induced by Sr²⁺ incorporation. At 1.0% and 2.0% SrI₂, the Urbach energy increases likely due to the segregation of SrI₂, as suggested by the microstrain analysis, however, it is still lower than that of the pristine perovskite. For 5.0%, a larger drop in Urbach energy is shown, suggesting that segregated SrI₂ could have a beneficial effect on the structural and electronic properties of the perovskite polycrystalline films. Other researchers have suggested that the accumulation of metal halides at the surface of the crystalline grain act as a passivation layer^{87–89}. It is possible that this is happening in these polycrystalline thin films only when the SrI₂ concentration is high enough to form precipitates that then passivate form at the surface of the perovskite. Both microstrain and Urbach energy show that large changes in the structure and electronic defects are happening at 5.0% SrI₂. The former can be attributed to the changes in the morphology with small grains and the latter with those smaller grains being passivated by the SrI₂ at a higher proportion than in lower SrI₂ concentrations. Urbach energies are different for each sample while bandgaps of the films remain unchanged, hinting at an overlap of trap states with energy bands.

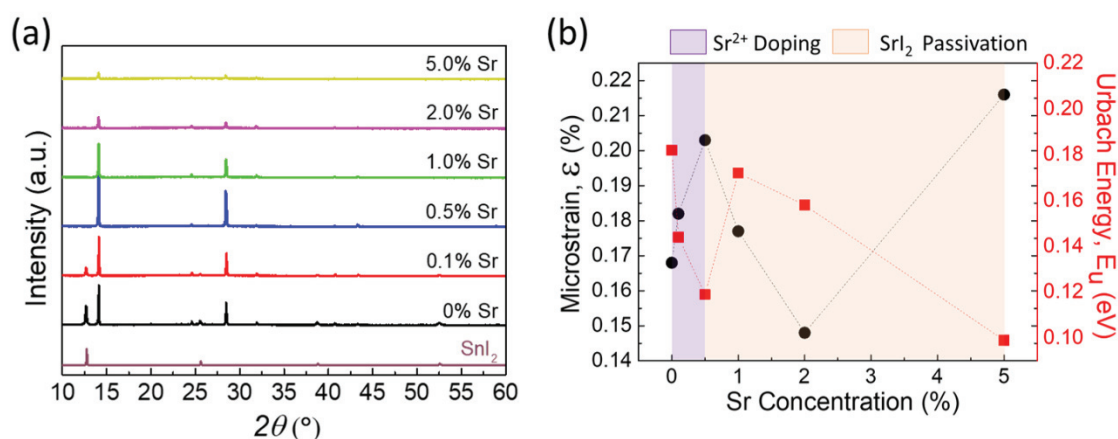


Figure 2.2. a) XRD pattern and b) microstrain and Urbach energies of the perovskite films with varying SrI₂ concentrations.

2.3.2. Optical Analysis

Optical absorbance analysis of pristine and SrI₂ added (FASnI₃)_{0.8}(MAPbBr₃)_{0.2} perovskite films were carried out for the energies between 1.0 and 4.0 eV as shown in

Figure 2.3a. From the absorbance spectra of the perovskite films, the optical bandgap (E_g) was calculated using Tauc's plot⁹⁰ shown in Figure 2.3b and details are given in Appendix A, supplementary Note 2. The data shows that the optical bandgap energies of all films are ~ 1.4 eV, which is in the range of the ideal bandgap of a single junction solar cell according to the SQ limit⁶⁴. To further understand the effect of SrI₂ on the optical properties of pristine perovskite film, photoluminescence (PL) measurements have been performed (Figure 2.3c). The PL peaks of all perovskite films are located at ~ 1.4 eV. The highest emission intensity among the perovskite films belongs to the perovskite film with 0.1% SrI₂, while the PL intensities of the 0.5% and 2.0% SrI₂ perovskite films are still higher than that of pristine perovskite film.

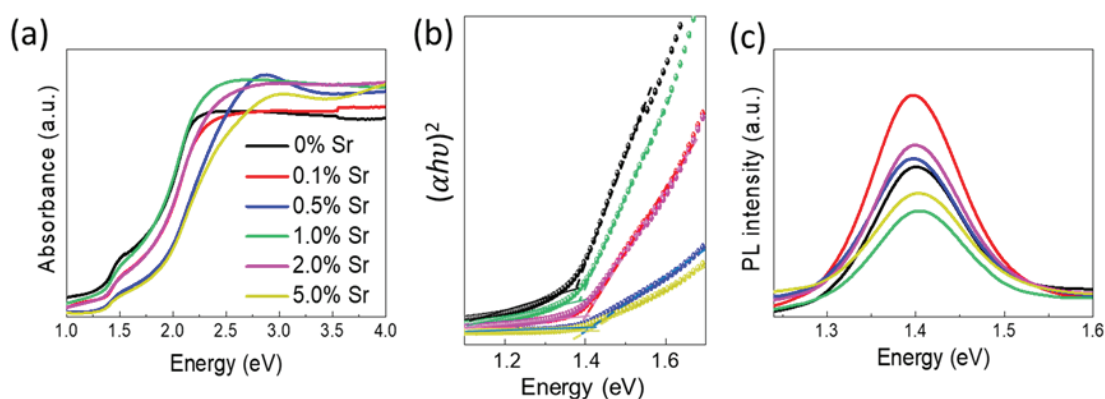


Figure 2.3. Optical properties of the films. a) UV-vis absorption, b) Tauc Plot, and (c) PL spectra.

2.3.3. Elemental Analysis

In order to investigate the effect of SrI₂ additive on the elemental composition of the (FASnI₃)_{0.8}(MAPbBr₃)_{0.2} perovskite, XPS analyses were carried out in the range of 0 to 800 eV as shown in Figure 2.4. According to the XPS survey results, the elements identified on the surface of perovskite films. F and Sr peaks originate from added SnF₂ and SrI₂ to the perovskite solution, respectively. The oxygen peak can be attributed to a combination of Sn oxidation and adsorbed oxygen. After adding SrI₂ to the perovskite structure, the F 1s peak at ~ 684.7 eV appears and the intensity of the peak increases for higher SrI₂ concentrations (Figure 2.4). Interestingly, these results suggest that the SrI₂ additive leads to the accumulation of F on the surface of the perovskite films. This

accumulation trend can be originated from the phase segregation of SnF₂, and the brightness of the SEM images in Figure 2.1a can be attributed to the segregation of F^{91,92}.

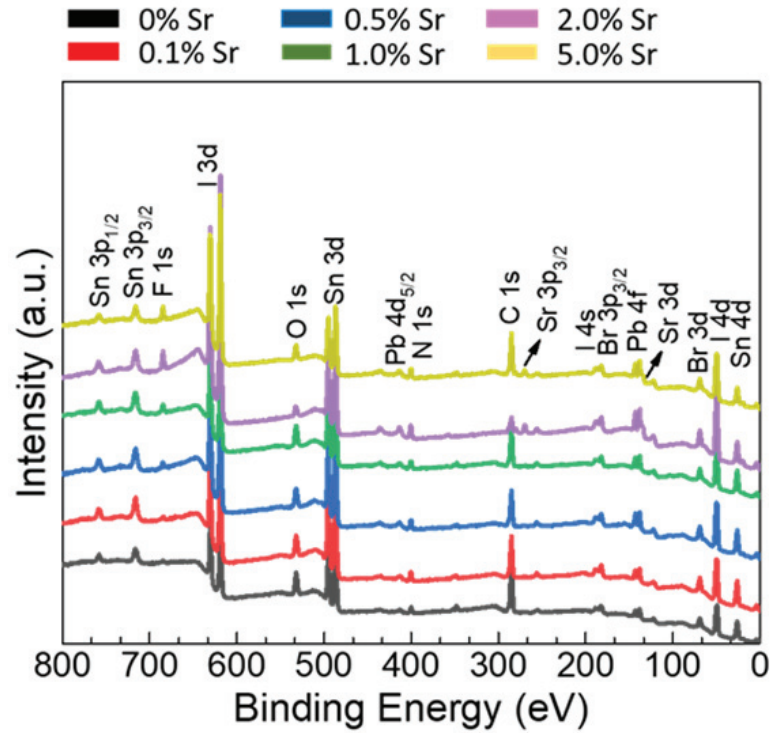


Figure 2.4. XPS survey spectra of the perovskite films.

In addition, there is less oxygen on the surface of the perovskite films with SrI₂ addition, as shown by the decrease in the intensity of the oxygen peak (Figure 2.4). To understand the effect of SrI₂ additive on Sn oxidation and oxygen adsorption in air-exposed perovskite films, high resolution XPS of the Sn 3d and O 1s peaks have been performed. Pb 4f, Sn 3d, I 3d, and Br 3d spectra are shown in Figure 2.5. Pb 4f spectrum for the perovskite films exhibit 4f_{5/2} and 4f_{7/2} peaks at 142.7 and 137.9 eV (Figure 2.5a)⁸⁴; Sn 3d spectra for pristine and SrI₂ added (FASnI₃)_{0.8}(MAPbBr₃)_{0.2} perovskite films show 3d_{3/2} and 3d_{5/2} peaks at 494.8 and 486.3 eV (Figure 2.5b)⁹³; I 3d spectrum for the films have 3d_{3/2} and 3d_{5/2} peaks at 630.2 and 618.7 eV (Figure 2.5c)⁹⁴, respectively. Br 3d peak is observed at 68.6 eV (Figure 2.5d)⁹⁵. The Sr 3d_{3/2} (135.6 eV) and Sr 3d_{5/2} (133.9 eV) are also evident in Pb 4f spectra in Figure 2.5a⁹⁴. After the addition of SrI₂ to the perovskite, Pb 4f, I 3d, Sr 3d, and Br peaks shift to higher binding energies. The reason for these shifts could be the presence of an oxide owing to surface band-bending⁹⁶. These shifts in XPS peaks suggest the chemical structure modification of the surface in the perovskite films⁹⁴.

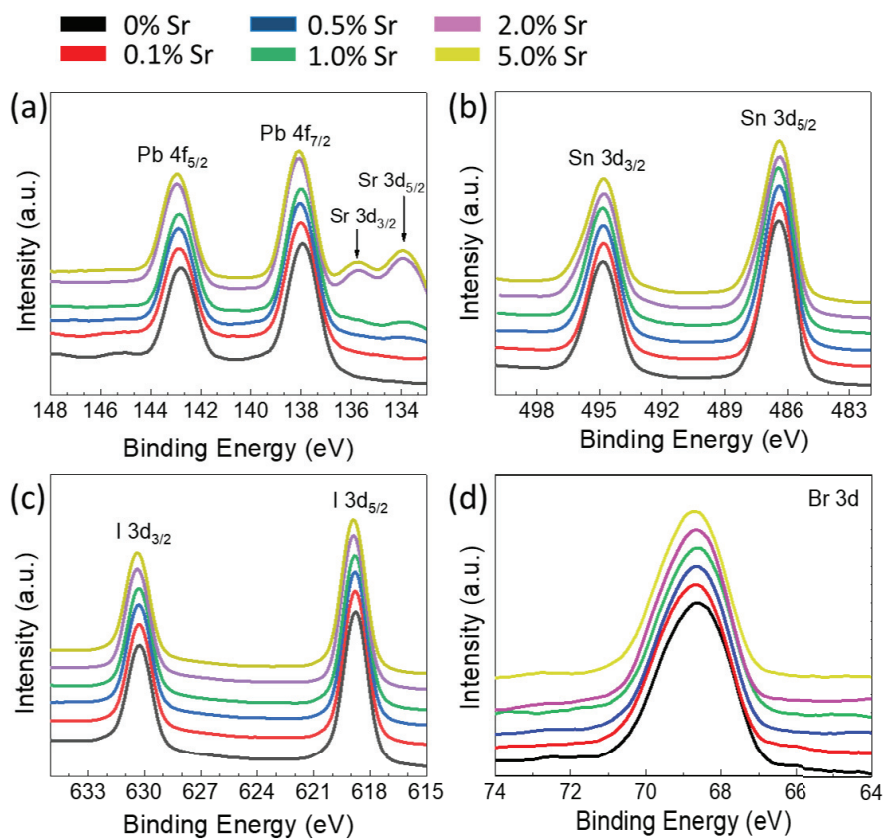


Figure 2.5. XPS spectra of a) Pb 4f b) Sn 3d c) I 3d, and d) Br 3d in perovskite films.

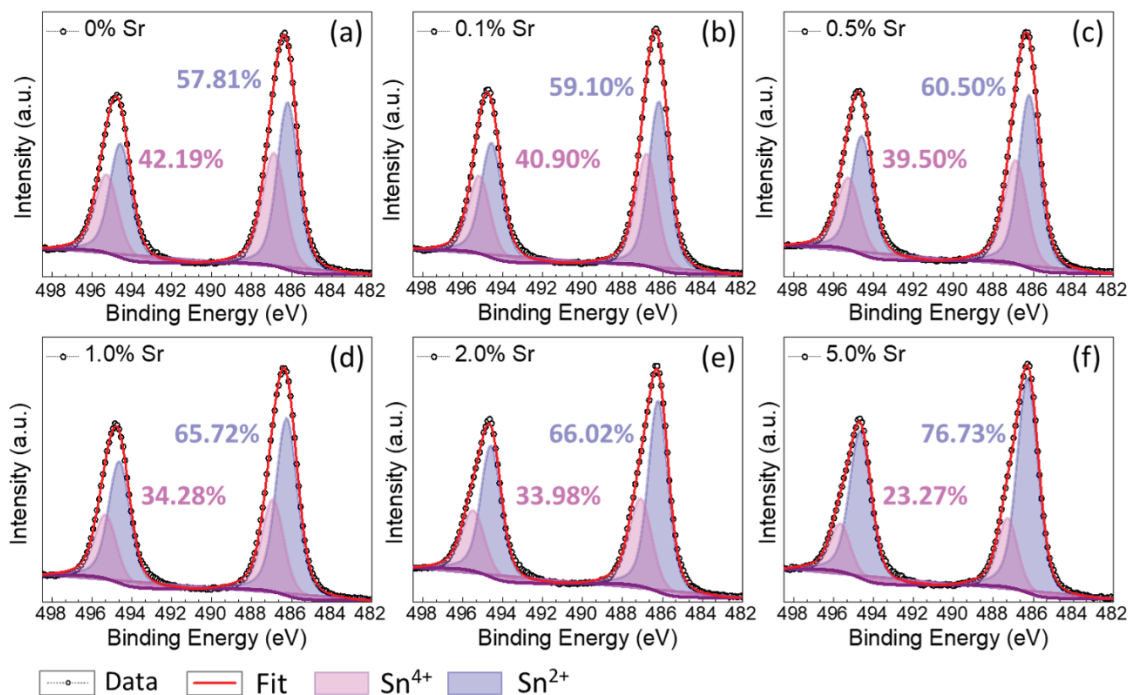


Figure 2.6. XPS spectra of Sn 3d peaks of a) pristine b) 0.1% Sr c) 0.5% Sr d) 1.0% Sr e) 2.0% Sr and f) 5.0% SrI₂ perovskite films.

Deconvolution of the Sn 3d peak represents the doublets of $3d_{3/2}$ at 495.27 eV and $3d_{5/2}$ at 486.87 eV are attributed to Sn^{4+} in SnO_2 and the doublets $3d_{3/2}$ at 494.56 eV and $3d_{5/2}$ at 486.17 eV assigned to Sn^{2+} (Figure 2.6)⁹⁷. There is a significant decrease in Sn^{4+} concentration (with respect to the Sn^{2+}) in the perovskite films with increasing SrI_2 concentration. The ratio of Sn^{4+} in the pristine perovskite film is 42.19% (Figure 2.6a). The addition of 5.0% SrI_2 to the perovskite film reduces the concentration of Sn^{4+} to 23.27% (Figure 2.6f). In order to quantify the amount of Sn species in the oxidized form, the ratio of $\text{Sn}^{4+}/\text{Sn}^{2+}$ (Figure 2.6) as a function of different SrI_2 concentrations were calculated as shown in Figure 2.7. A decrease in the ratio of $\text{Sn}^{4+}/\text{Sn}^{2+}$ was observed with the increase in SrI_2 addition. The information gained from deconvoluted Sn 3d XPS peaks suggests that the addition of Sr^{2+} to the perovskite causes a decrease in Sn^{2+} oxidation, which also decreases the Urbach energy and increases the microstrain of the perovskite films in Figure 2.2b.

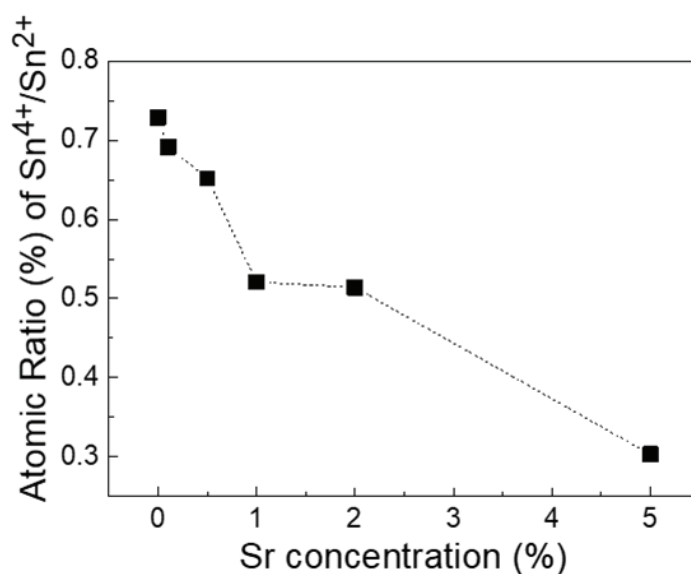


Figure 2.7. Atomic ratio of $\text{Sn}^{4+}/\text{Sn}^{2+}$ at different SrI_2 concentrations.

Figure 2.8 shows that the binding energies of the oxygen fitted peaks are observed at 530.26, 531.68, and 532.38 eV which are assigned to metal oxide coming from Sn-O, Pb-O and Sr-O, C-OH and C=O due to adsorbed atmospheric hydrocarbons from air, respectively⁹⁸⁻¹⁰⁰. Considering the deconvolution of O 1s spectra, the atomic ratio of metal oxide for pristine perovskite film is 17.71% while for 5.0% SrI_2 added perovskite film, an increase in the ratio is observed with the atomic percent of 8.83%. Also, the rate

graph of the atomic ratio of metal oxide to that of C-OH and C=O at different SrI₂ amounts is shown in Figure 2.9. When the atomic ratio of oxygen coming from Sn-O with adsorbed atmospheric hydrocarbons and oxygen due to exposing air is compared, it is found that there are no exact correlations between them. In Sn deconvolution peaks, it is observed that SrI₂ addition causes a decrease in Sn-oxidation with increasing SrI₂ concentration. However, it is observed in O 1s deconvolution peaks that the atomic ratio of metal oxide to C-OH and C=O increases at 0.1% SrI₂. This behavior could be the result of higher adsorbed atmospheric hydrocarbons on the surface of the film. Nevertheless, with an increasing amount of SrI₂ to 5.0%, metal oxidation seems to be reduced significantly as shown in Figure 2.9.

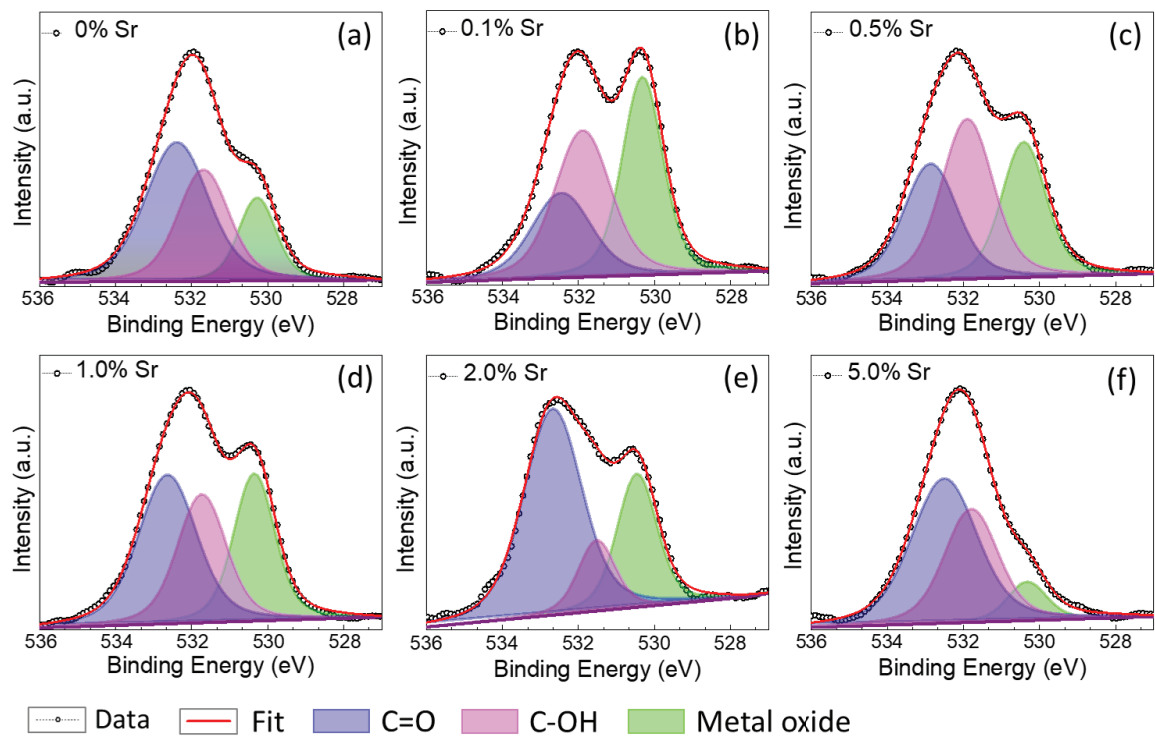


Figure 2.8. XPS spectra of O 1s peaks of a) pristine b) 0.1% c) 0.5% d) 1.0% e) 2.0%, and f) 5.0% SrI₂ added perovskite films.

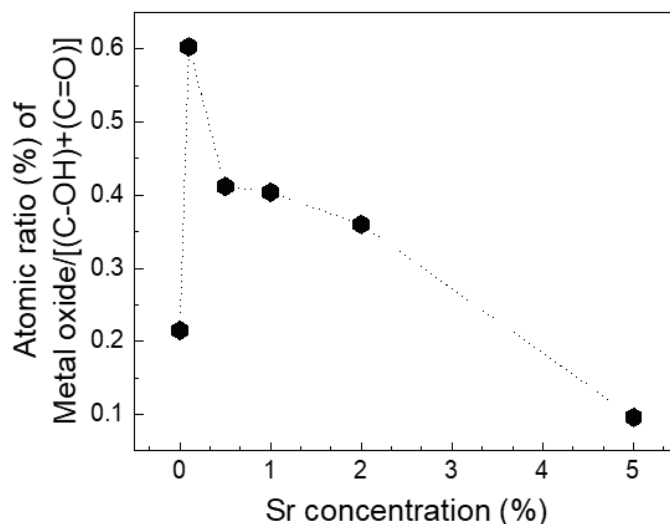


Figure 2.9. Atomic ratio (%) of metal oxide / [(C-OH) + (C=O)] for each sample as calculated from deconvoluted from XPS measurements.

2.4. Conclusion

A detailed investigation of the effects of SrI₂ addition to (FASnI₃)_{0.8}(MAPbBr₃)_{0.2} perovskite thin film with different concentrations has been presented. It was shown that SrI₂ additive leads to Sr²⁺ incorporation into the perovskite lattice for 0.1 and 0.5% SrI₂ concentrations. For higher concentrations, SrI₂ segregation takes place in the perovskite owing to the lattice relaxation with lower strain. Urbach energy calculations of the perovskite films show that SrI₂ addition leads to lower structural disorder in both Sr²⁺-incorporated and SrI₂ segregation cases. These results suggest segregated SrI₂ in the film could be acting as a passivating agent at high enough concentrations exceeding the doping limit of 0.5%. According to the XPS analysis results, deconvoluted spectra for Sn show that oxidation of Sn²⁺ decreases with the addition of SrI₂. Therefore, SrI₂ addition can be considered a possible way to decrease oxidation in Sn-based perovskites and therefore increase the long-term durability of the material while reducing the amount of lead (lower toxicity) in the perovskite layer.

CHAPTER 3

IMPROVING PERFORMANCE OF PEROVSKITE SOLAR CELLS WITH ALKALINE EARTH METAL ADDITIVES

3.1. Introduction

Halide perovskite solar cells are regarded as one of the most promising technologies for the next generation of photovoltaics due to their high power conversion efficiency (PCE) and manufacturing by using a simple solution technique. The absorber layer of PSCs is the most commonly studied on MA-based perovskites owing to achieved high efficiencies. However, it is reported that MAPbI₃ is unstable due to low tolerance to heat and moisture, which shows film degradation due to the volatility of MA⁺¹⁸. Moreover, FAPbI₃ exhibits good photo- and thermo-stabilities with a longer carrier lifetime compared to the MAPbI₃¹⁰¹. However, FAPbI₃ exhibits degradation under the effect of relative humidity, and the black α -phase perovskite of pure FAPbI₃ (only stable above 160 °C) degrades into photo-inactive yellow δ -phase below the phase transition temperature^{18,102}. Stabilizing the desired black phase of FAPbI₃ in the air for photovoltaic applications is still a problem. Recently, moisture stability of perovskites with higher performance is achieved by mixed cation perovskites (including Rb⁺, Cs⁺, MA⁺, and FA⁺)²⁰. According to the reported works, the stability of FAPbI₃ can be improved by partially incorporating MA⁺ or Cs⁺ into FAPbI₃. Considering the volatility of MA⁺, incorporated monovalent cation Cs⁺ is a good candidate to enhance the structural stability of FAPbI₃.

Determination of the exact size of the organic cation in organic-inorganic halide perovskites is not easy due to their non-spherical geometry and the constant rotation in the lattice¹⁰³. FAPbI₃ is stable in the δ -phase since it has a high tolerance factor (>1.0) because of the large ionic size of FA⁺. Therefore, by tuning its tolerance factor with the incorporation of Cs⁺ with a low tolerance factor, achieving stable α -phase Cs_xFA_{1-x}PbI₃ with improved optical and electrical properties is possible^{17,104}. Furthermore, some

reports have been conducted to increase the stability of the black-FAPbI₃ phase and the performance of FA-based organic-inorganic halide perovskite solar cells via doping and passivation mechanisms^{105,106}.

PSCs suffer from current-voltage (J - V) hysteresis came into view in different J - V scan directions. The hysteresis issue was first approached by Snaith *et al*¹⁰⁷. The factors which trigger the hysteresis behavior in the J - V curve could be ferroelectricity, modulation of charge transport, and ion migration¹⁰⁸. By hindering the ion migration and decreasing the defect density, the hysteresis can be suppressed¹⁰⁹. The hysteresis in the J - V curve can also be reduced by grain boundary engineering passivation mechanism^{110,111}.

In this work (Yuce H. *et al.*)¹¹², the effects of Sr²⁺ and Ca²⁺ additives with similar and lower ionic sizes compared to Pb²⁺ ($r_{Pb^{2+}} = 119 \text{ pm}$; $r_{Sr^{2+}} = 118 \text{ pm}$; $r_{Ca^{2+}} = 100 \text{ pm}$)¹¹³ on Cs_{0.1}FA_{0.9}PbI₃ perovskites and the performance of these CsFA-based PSCs have been investigated. It is shown that Sr²⁺ and Ca²⁺ additives make the morphology of the perovskite uniform as confirmed by scanning electron microscopy (SEM). Microstrain calculations for the perovskite films by using the Williamson-Hall method have been performed. Morphology and the microstrain calculations suggested a specific additive limit of 0.5% for improvement in the additive series beyond which the films were affected negatively. The highest average PCE of 13.29% based on 0.5% Sr²⁺:Cs_{0.1}FA_{0.9}PbI₃ and 12.82% based on 0.5% Ca²⁺:Cs_{0.1}FA_{0.9}PbI₃ was achieved while Cs_{0.1}FA_{0.9}PbI₃ has a PCE of 11.20%. The effects of Sr²⁺ and Ca²⁺ on the hysteresis of CsFA-based PSCs has been also investigated. By the addition of 0.5%Sr²⁺, the hysteresis of PSC is remarkably reduced by passivation. It is proved that low concentration additive engineering with divalent cation in the perovskite films is a viable option for improving the performance of PSCs.

3.2. Experimental Section

Materials and Sample Preparation: Soda-lime glass and fluorine-doped tin oxide (FTO) coated glass substrates (2.5x2.5 cm²) were cleaned by sonication in 2% Hellmanex water solution for 15 min. After rinsing with DI water, the substrates were cleaned with DI water, acetone, and isopropanol for 15 min, respectively. Then, the substrates were dried under nitrogen flow and exposed to UV-Ozone for 15 min.

Electron transport layer preparation: A compact TiO₂ (c-TiO₂) precursor solution was prepared with the mixture of 0.480 mL of Acetylacetone (Sigma-Aldrich) 0.720 mL of titanium diisopropoxide bis(acetylacetonate) (75 wt % in isopropanol, (Sigma-Aldrich)) diluted in 10.8 mL of anhydrous ethanol (Sigma-Aldrich). The precursor was deposited with oxygen as a carrier gas at 450 °C on FTO substrates by using a spray pyrolysis process. At 450 °C for 30 min, the TiO₂ coated substrates were then sintered and left to cool slowly down to room temperature. A mesoporous TiO₂ (m-TiO₂) solution was prepared with the dilution of 150 mg TiO₂ paste (Sigma Aldrich) in 1 mL anhydrous ethanol. The m-TiO₂ solution was spin coated on a c-TiO₂ layer at 4000 rpm for 30 sec, and the samples were immediately dried on a hot plate at 150 °C for 15 min and then sintered at 450 °C for 30 min.

Perovskite precursor solution and film preparation: A Precursor solution of Cs_{0.1}FA_{0.9}PbI₃ was prepared by mixing 1.5 M PbI₂ (TCI America) and 1.5 M cesium iodide (CsI, Sigma Aldrich) was dissolved in 8:1 V/V Dimethylformamide (DMF, Acros Organics)/dimethyl sulfoxide (DMSO, Acros Organics) and DMSO, respectively. After that, formamidinium iodide (FAI, Dyenamo) powders were dissolved in the PbI₂ solution (molar ratio of FAI/PbI₂: 1/1.09, lead excess precursor). The additives which are strontium iodide (SrI₂, Alfa Aesar) and calcium iodide (CaI₂, Sigma Aldrich) were dissolved in DMSO (1.5 M). Perovskite solution was coated on the substrates by 2- step spin coating (step 1: 1000 rpm for 2 sec; step 2: 4000 rpm for 23 sec). 10 sec before the end of spinning, 200 µL of chlorobenzene was dropped on the perovskite dropped substrate. The perovskite coated films were immediately annealed at 150 °C for 15 min in a nitrogen-filled glove box.

Hole transporting and contact layers preparation: Spiro OMeTAD (1-Material) solution (0.07M) was doped with 0.5 M bis(trifluoromethylsulfonyl)imide lithium salt (Li-TFSI, Sigma Aldrich), 0.03 M tris(2-(1Hpyrazol-1-yl)-4-tert-butylpyridine)-cobalt(III)tris(bis(trifluoromethylsulfonyl)imide) (FK209, Sigma Aldrich) and 3.3 M 4-tert-Butylpyridine (TBP, Sigma Aldrich). Then, the precursor was spin coated on a perovskite layer at 3000 rpm for 30 sec. Finally, the Au electrode layer with a thickness of 100 nm was evaporated on the spiro-OMeTAD layer.

The final structure of fabricated perovskite device solar cells with an active area of 0.128 cm² was FTO/c-TiO₂/m-TiO₂/Perovskite/spiro-OMeTAD/Au as shown in Figure 3.1a.

Characterizations of Perovskite Films and Devices: Morphology of perovskite film surface was obtained by using the Hitachi SU-8230 SEM. X-ray Diffraction (XRD)

measurements were carried out using a Malvern PANalytical Empyrean using Cu K α radiation ($\lambda= 1.54$ nm) with a scan step size of 0.0131 $^\circ$. The chemical states of elements were probed by an X-ray photoelectron spectrometer (XPS) (Thermo K-Alpha XPS) equipped using an Al K α (1486.6 eV) monochromatic source with a spot size of 400 μm . Absorption spectra were collected by using the Carry 500 UV-Visible-NIR spectrometer. Photoluminescence (PL) measurements were performed by using Horiba FL3-21 Fluorometer with an excitation wavelength of 560 nm. SEM, XRD, and XPS analyses were carried out on perovskite coated on FTO/glass substrates, and optical measurements were performed on perovskite coated on glass substrates. The J - V curves of the devices were measured in a forward and reverse bias under the solar simulator (Fluxim, Litos Lite) with an AM1.5 spectrum at a scan rate of 15 mV/s (Figure 3.1b). The numbers of the devices per each series are 15 for CsFA, 0.1% Sr $^{2+}$, 0.1% Ca $^{2+}$, 0.5 Ca $^{2+}$; 16 for 1.0% Sr $^{2+}$; 23 for 0.5 Sr $^{2+}$ PSCs.

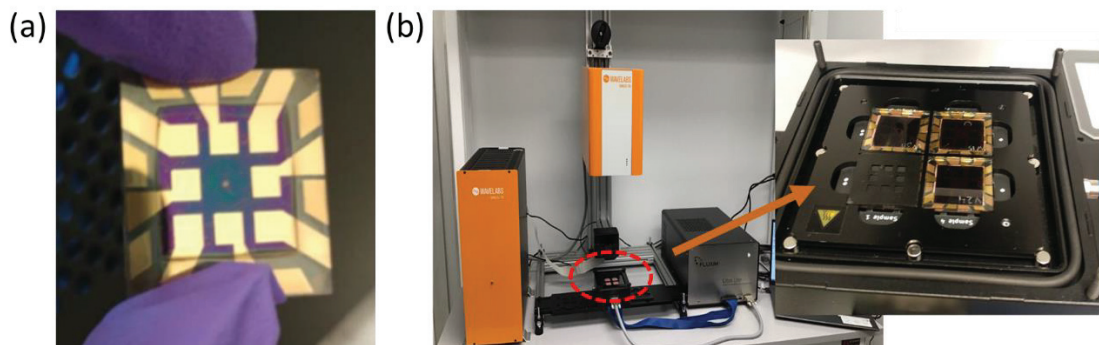


Figure 3.1. Images of a) perovskite solar cell pixels and b) measurement setup for the solar cell performance.

3.3. Results and Discussion

3.3.1. Morphological and Structural Analysis

In order to investigate the surface morphologies of the perovskite absorber layers, the samples were evaluated by SEM. The SEM images of Sr $^{2+}$ and Ca $^{2+}$ perovskite series with pristine perovskite are shown in Figure 3.2. The SEM images show that the addition of Ca $^{2+}$ and Sr $^{2+}$ causes homogenization of the perovskite grain sizes. The morphological properties of Sr $^{2+}$ and Ca $^{2+}$ added perovskite films with the concentration of 0.1% and

0.5% appear quite similar (Figure 3.2b,c). Moreover, by increasing the additive concentration from 0.5% to 1.0%, the cracks in the SEM image are observed for 1.0% Sr²⁺ added perovskite in Figure 3.2b. However, the cracks are not observed for 1.0% Ca²⁺ perovskite film in Figure 3.2c. The difference in the SEM images of 1.0% Sr²⁺ and 1.0% Ca²⁺ samples could have originated from the different ionic radii of the additives. Excess additives affect negatively and lead to deterioration of the perovskite films' morphological structure¹¹⁴. The ideal additive limit is observed as 0.5% for Sr²⁺ and Ca²⁺ perovskites due to the observed cracks for Sr²⁺ and smaller grains for Ca²⁺ perovskites at a higher concentration of 1.0%. The brightness of the grain boundaries could be attributed to the segregated metal halides¹¹¹. For all samples, over stoichiometric PbI₂:AI (1.09:1.0) where A is Cs_{0.1}FA_{0.9} was employed and the brightness in Figure 3.2a is probably the result of segregated PbI₂. After adding SrI₂ and CaI₂ to the perovskites, the segregated metal halides can be partially PbI₂/SrI₂ and PbI₂/CaI₂ as shown in Figure 3.2d.

XRD patterns of the perovskite films coated on FTO substrates are shown in Figure 3.3a,b. According to the XRD analysis results, all perovskite films exhibit similar crystal structures with diffraction peaks centered at $2\theta=13.93^\circ$, 19.75° , 24.26° , 28.10° , and 40.19° corresponding to the perovskite phase and at $2\theta=26.45^\circ$, 31.47° , 37.70° , and 42.74° corresponding to the mixed δ - and perovskite phases. In the case of Sr²⁺ and Ca²⁺ additions to the perovskite structure, any new peak is not observed, suggesting that no new crystalline phases form. Segregated metal halides are undetectable by XRD due to their low concentrations. Homogeneous structural strain behavior is usually detected by a systematic shift in the signals in XRD patterns. Considering the absence of a systematic shift in XRD peaks of our samples, there is no homogeneously strained lattice due to macrostrain in the perovskite crystal structure¹¹⁵. A microstrain in a crystalline material originates from small fluctuations in the lattice spacing, and these small fluctuations are detected owing to crystal imperfections or structural defects; such as dislocations, vacancies, interstitials, twinings, and grain boundaries¹¹⁴. The microstrain is detected by analyzing the broadening of XRD signals. Therefore, in order to monitor the inhomogeneous strain behavior, the microstrain calculations by using Williamson-Hall plot were performed for the Sr²⁺ and Ca²⁺ perovskite series in Figure 3.3c, and the details of microstrain calculations are given in supporting information (Figure S3.1 and Table S3.1). It was observed that microstrains in both Sr²⁺ and Ca²⁺ perovskite series follow the same trend where the microstrain decreases until 0.5% additive concentration, then it

increases at an additive concentration of 1.0%. The microstrain values for the Sr^{2+} perovskite series are lower than those for the Ca^{2+} perovskite series in all concentrations.

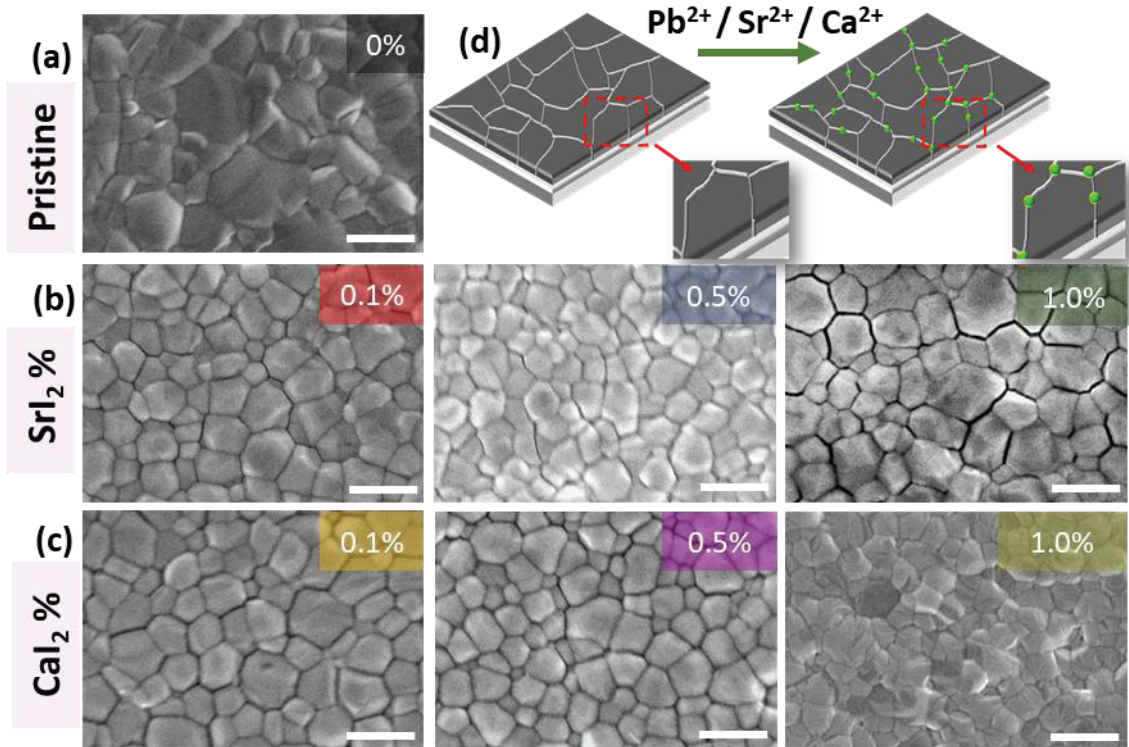


Figure 3.2. SEM images of a) pristine, b) Sr^{2+} and c) Ca^{2+} added perovskite with the concentration of 0.1%, 0.5%, and 1.0%. d) Illustration of the proposed microstructure of perovskite films. The left and right sides indicate pristine and $\text{Sr}^{2+}/\text{Ca}^{2+}$ added perovskite films, respectively. Excess metal halides at the grain boundaries are indicated by green spheres. Bar size is 500 nm for all micrographs.

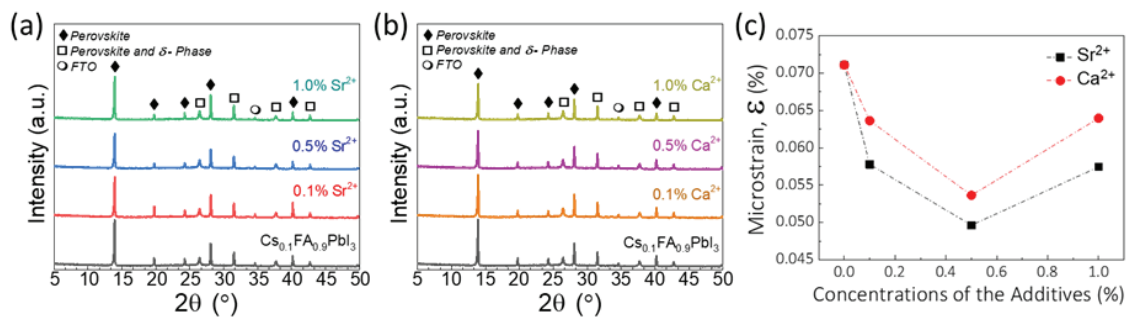


Figure 3.3. XRD signals of a) Sr^{2+} and b) Ca^{2+} additive perovskite series. (c) Calculated microstrains of the perovskite films.

Considering a higher microstrain due to high defect density, the calculations suggest that the defect density in the perovskites is reduced by the additives. The mechanism behind the reduction of microstrain by the additives is most probably passivation by metal halides at grain boundaries as suggested by the reported work in which excess PbI_2 passivates the perovskite¹¹⁶. Similarly, SrI_2 and CaI_2 additives with/without PbI_2 can segregate at the grain boundaries as illustrated in Figure 3.2d. In case of considering that the pristine perovskite film has already been passivated by excess PbI_2 , It can be concluded that the passivation effects of SrI_2 and CaI_2 are proven to be better than that of PbI_2 , or a mixture of the additives with PbI_2 , which is determined by microstrain calculations of the films. The additive limit is determined to be the concentration of 0.5% by microstrain calculations in Figure 3.3c which is also compatible with SEM images with uniform grains due to the added Sr^{2+} and Ca^{2+} at 0.5% concentration in Figure 3.2b,c.

3.3.2. Optical Analysis

Figure 3.4 shows the Tauc plot and the photoluminescence (PL) spectrum of the perovskite films. The absorption spectra of the films were given in Figure S3.2. The bandgap energy was calculated by linear fitting of the absorption band edge as 1.53 eV for Sr^{2+} and Ca^{2+} additive perovskite series in Figure 3.4a,b, and the details of Tauc plot calculations are given in Supporting Information. Considering the SQ limit, the calculated bandgap of 1.53 eV is near the ideal bandgap of an absorber layer for single-junction solar cells⁶⁴. Note that all perovskite films including Sr^{2+} and Ca^{2+} additive perovskite series have the same bandgap energy, which shows that the additives at low concentrations do not affect the bandgap energy of the perovskite films. Gaussian fitted peaks of PL emissions (raw data in Figure S3.3) for all perovskite films are centered at ~ 813 nm (~ 1.525 eV) in Figure 3.4c,d, which is very close to the bandgap of the films. The positions of the PL emissions remain unchanged with the addition of Sr^{2+} and Ca^{2+} . According to the PL measurements, the optical properties of the perovskites are improved in presence of the additives within the film. The highest PL intensities are observed at 0.1% concentration for Sr^{2+} (Figure 3.4c) and Ca^{2+} (Figure 3.4d) additive perovskite series. PL intensity of 0.5% Sr^{2+} added perovskite film is higher than that of pristine perovskite. The lowest PL intensities among Sr^{2+} and Ca^{2+} additive series belong to 1.0%

concentrations of additives. Furthermore, the PL intensity of pristine perovskite is the same as those of 1.0% Sr²⁺ and 0.5% Ca²⁺ perovskites.

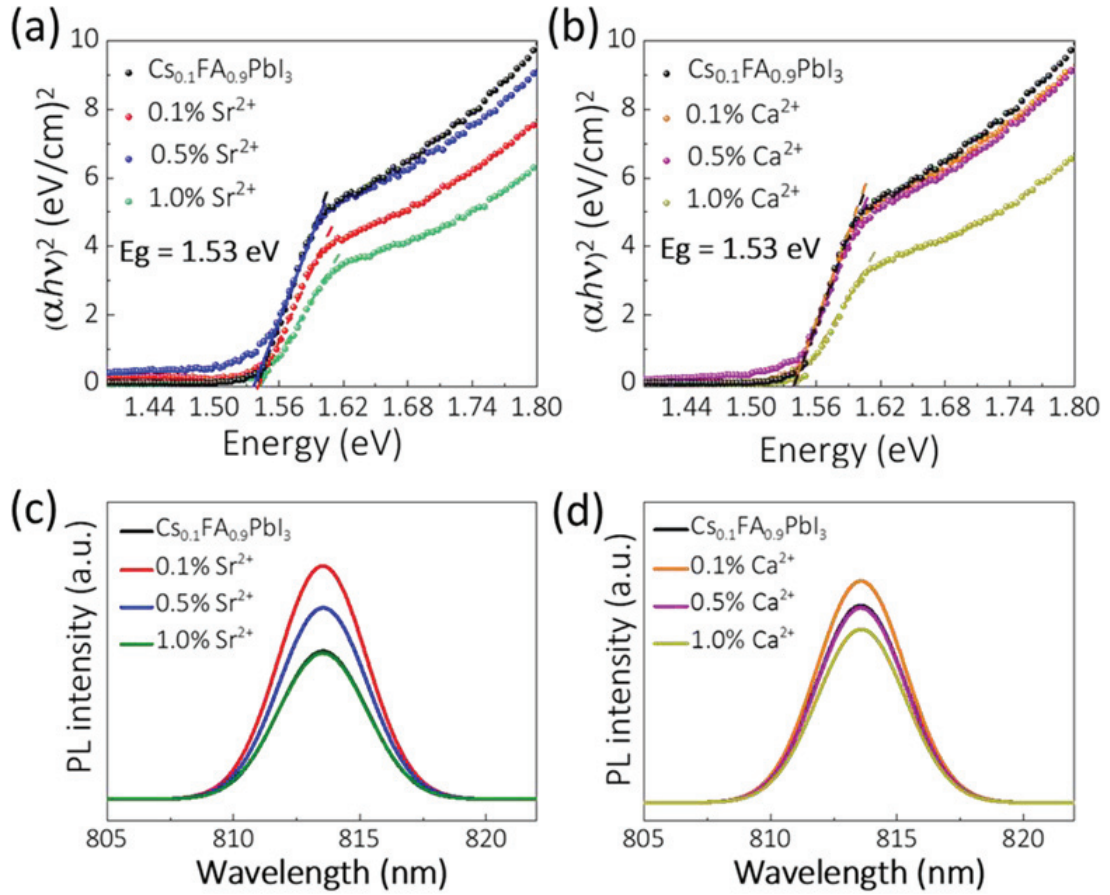


Figure 3.4. Tauc plots of a) Sr²⁺ and b) Ca²⁺ additive perovskite series by using absorption spectra. PL spectra of c) Sr²⁺ and d) Ca²⁺ additive perovskite series.

3.3.3. Elemental Analysis

To further clarify the change of the Cs_{0.1}FA_{0.9}PbI₃ perovskite films after the addition of Sr²⁺ and Ca²⁺, XPS measurements were performed. XPS survey spectra of Sr²⁺ and Ca²⁺ series in the binding energy range of 0 to 900 eV are shown in Figure 3.5a,b. After the addition of the additives, Sr- and Ca- related lines in the XPS survey spectra are not distinguishable due to low concentrations of the additives. Figure 3.5c shows detailed spectra in the energy region of Pb 4f_{7/2}/Sr 3d core levels. The Sr 3d_{5/2} line is detected at 133.9 eV for Sr²⁺ added perovskite films¹¹⁵ while only the edge of Pb 4f_{7/2} signal for pristine perovskite (0%) is observed. XPS spectra of Ca 2p doublets which are obtained

at 351.78 eV for Ca 2p_{1/2} and 348.23 eV for Ca 2p_{3/2}¹¹⁷ with the spin-orbit splitting energy of 3.55 eV¹¹⁸ as shown in Figure 3.5d. Here, Figures 3.5c,d demonstrate the presence of Sr²⁺ in Sr²⁺ additive series and Ca²⁺ in Ca²⁺ additive series, respectively. Atomic percentage ratios of Sr 3d/Pb 4f and Ca 2p/Pb 4f were calculated for Sr²⁺ and Ca²⁺ additive perovskite series, given in Table 3.1.

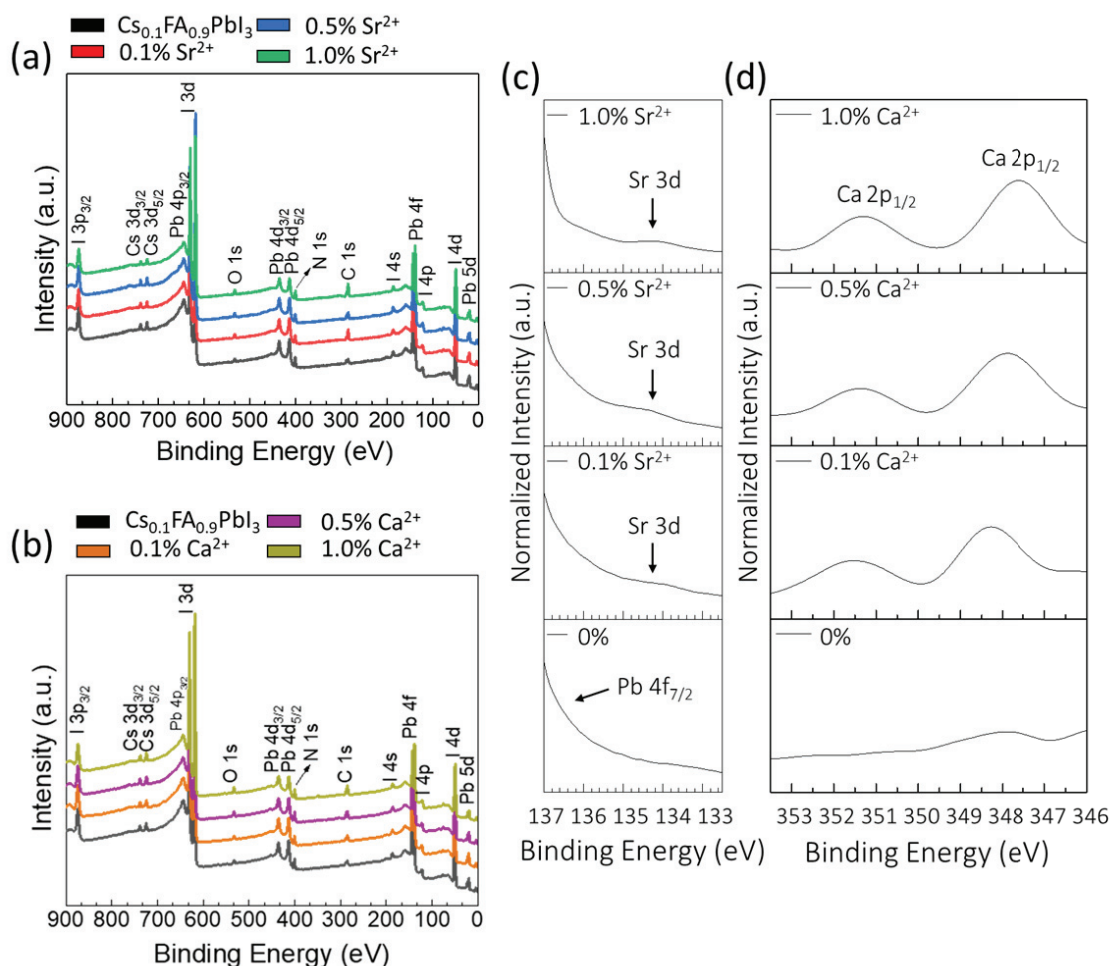


Figure 3.5. XPS survey spectra of a) Sr²⁺ and b) Ca²⁺ additive perovskite series. XPS spectra of c) Pb 4f/Sr 3d and d) Ca 2p core levels of the perovskite films.

Table 3.1 Atomic percentage in sample for element to Pb ratio (Z:Pb)

Z:Pb 4f (%)	0.1% Sr ²⁺	0.5% Sr ²⁺	1.0% Sr ²⁺	0.1% Ca ²⁺	0.5% Ca ²⁺	1.0% Ca ²⁺
Sr 3d	1.2	2.9	3.8	-	-	-
Ca 2p	-	-	-	0.9	2.0	2.7

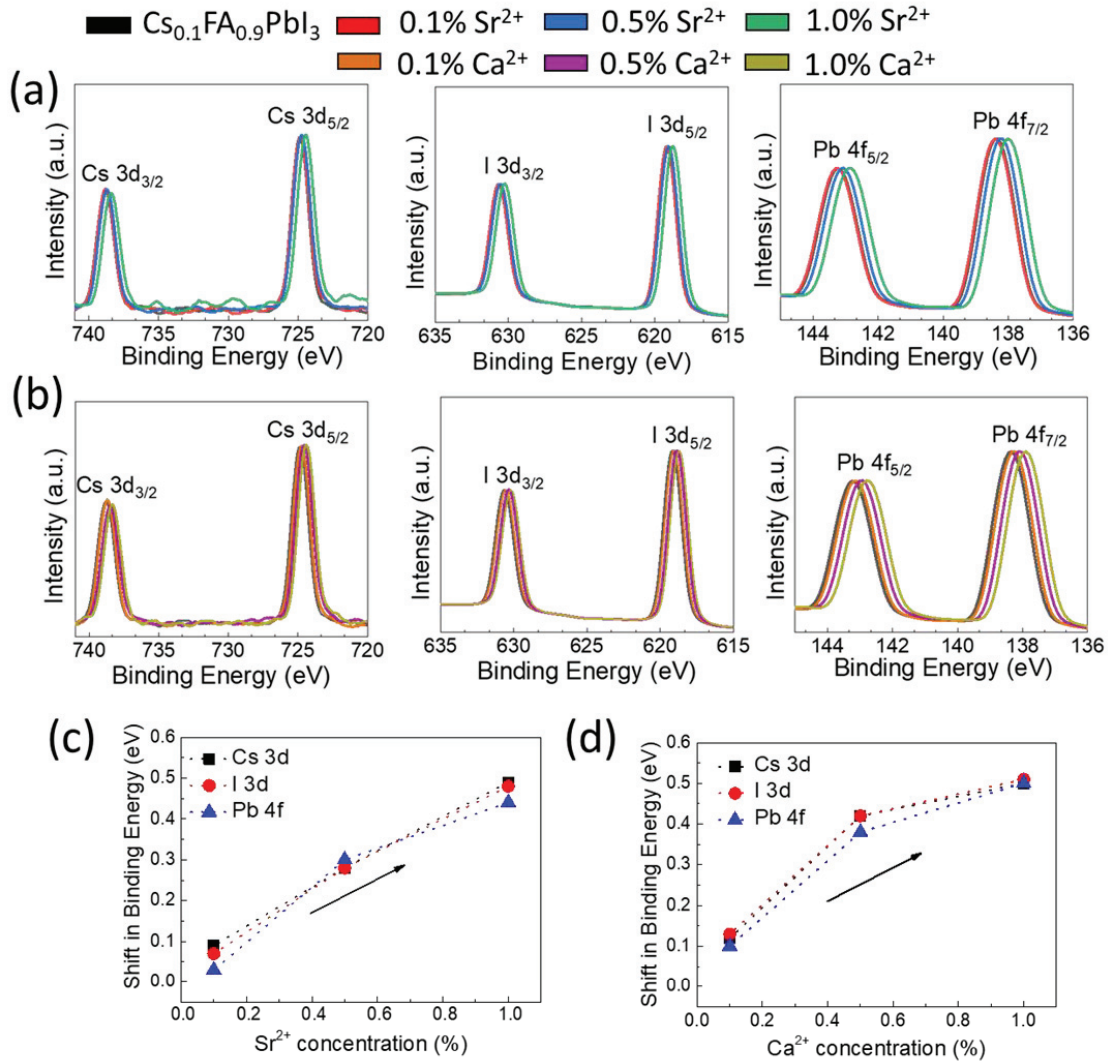


Figure 3.6. XPS spectra of Cs 3d, I 3d and Pb 4f for a) Sr²⁺ and b) Ca²⁺ additive perovskite series. The energy shifts in the different elemental core level peaks of c) Sr²⁺ and d) Ca²⁺ perovskite films.

Table 3.2. The shifts in binding energies of the perovskite films for Cs 3d, I 3d, and Pb 4f XPS spectra.

Additives	Cs 3d (eV)	I 3d (eV)	Pb 4f (eV)
0.1% Sr ²⁺	0.09	0.07	0.03
0.5% Sr ²⁺	0.28	0.28	0.30
1.0% Sr ²⁺	0.49	0.48	0.44
0.1% Ca ²⁺	0.12	0.13	0.10
0.5% Ca ²⁺	0.42	0.43	0.38
1.0% Ca ²⁺	0.50	0.51	0.50

Figures 3.6a,b show the XPS spectra of Cs 3d, I 3d, and Pb 4f for Sr²⁺ and Ca²⁺ series, respectively. For pristine perovskite film, Cs 3d doublets are located 738.8 eV (Cs 3d_{5/2}) and 724.9 eV (Cs 3d_{3/2})¹¹⁹. Moreover, the signals of Pb 4f_{5/2} and Pb 4f_{7/2} are observed at 143.3 eV and 138.4 eV¹²⁰. For I 3d spectra, I 3d_{5/2} and I 3d_{3/2} peaks are located at 630.7 eV and 619.2 eV¹²⁰. The spin-orbit splitting energies of Cs 3d, Pb 4f, and I 3d doublets are calculated as 13.9, 4.9, and 11.4 V, respectively. In addition, It can be seen that there are shifts in the binding energies of Cs 3d, Pb 4f, and I 3d after the addition of Ca²⁺ and Sr²⁺ to the perovskite film. In the case of increasing the concentration of Sr²⁺ and Ca²⁺ in the perovskite samples, the binding energies of the core levels shift to lower binding energies, which is the result of the electronegativity difference of the additives¹²¹. Considering the electronegativities¹²² of Pb (1.85), Sr (0.96), and Ca (1.03), the differences in the electronegativity of the divalent cations could also explain the reason for the different shifts in the binding energies for Sr²⁺ and Ca²⁺ series. These shift variations for Sr²⁺ (Figure 3.6c) and Ca²⁺ additives (Figure 3.6d) show small differences, and these shift parameters are given in Table 3.2. The same trend in binding energy shifts is also observed for C1s, N1s, and O1s XPS core level spectra, which are given in Figure 3.7.

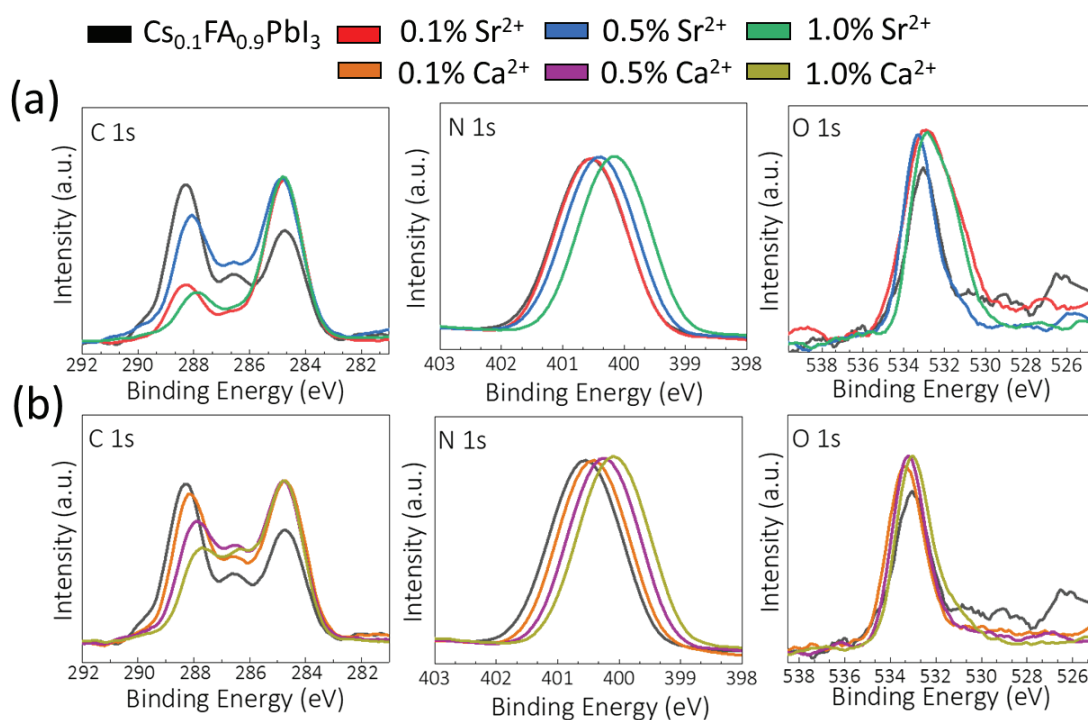


Figure 3.7. XPS spectra of C 1s, N 1s, and O 1s for a) Sr²⁺ and b) Ca²⁺ additive perovskite series.

Figure 3.7 shows C 1s, N 1s, and O 1s core level XPS spectra for Sr²⁺ and Ca²⁺ additive perovskite series. In the C 1s spectra of Cs_{0.1}FA_{0.9}PbI₃ perovskite, the peaks at 284.8, 286.6, and 288.4 eV were assigned to C-H, C-N, and O-C=O bonds, respectively¹²³. The N 1s region of pristine perovskite includes one peak at 400.2 eV assigned to C-N bonds¹²³. O 1s peak of pristine perovskite is at 532.7 belonging to the C=O bond¹²³. In the case of adding Sr²⁺ and Ca²⁺ to the perovskite, XPS binding energies shift to lower binding energies. For the O 1s region, the reason for the broadened peak for the Sr²⁺ perovskite series can be the formation of surface hydroxides at around 530.9 eV¹²⁴.

3.3.4. Solar Cell Characterization

The effects of Sr²⁺ (similar ionic radii with Pb²⁺) and Ca²⁺ (smaller ionic radii than Pb²⁺) additives on the performance of PSCs are shown in Figure 3.8. The n-i-p architecture of PSC with FTO/compact TiO₂/ mesoporous TiO₂/ perovskite/Spiro OMeTAD/Gold was constructed as shown in Figure 3.8c. The solar cell parameters, which are open-circuit voltage (V_{oc}), fill factor (FF), short circuit current density (J_{sc}), and PCE were extracted from reverse *J-V* curves of Sr²⁺ and Ca²⁺ additive series and plotted in Figures 3.8a,b. The device parameters obtained from forward/reverse *J-V* curves are plotted as box plots. The *J-V* curves belonging to high performance PSCs for each series are given in Figure 3.8d.

The solar cell parameters suggest Sr²⁺ and Ca²⁺ addition to the perovskite significantly improve the device performance. The pristine perovskite device yields an average PCE of 11.20 % with V_{oc}, FF, and J_{sc} values of 0.92 V, 64.92%, and 18.66 mA/cm². Considering similar ionic radius with Pb²⁺; the addition of Sr²⁺ until 0.5% concentration improves the performance of PSCs. By the addition of Sr²⁺ at 0.1% concentration, the device parameters are improved with a resulting average PCE value of 12.25%. The maximum device parameters are obtained for 0.5% Sr²⁺ PSC series with an average PCE of 13.29%, V_{oc} of 0.96 V, FF of 67.37%, and J_{sc} of 20.34 mA/cm². Considering lower J_{sc} at 1.0% Sr²⁺ PSCs compared to the others, it can be said that a high concentration of Sr²⁺ can prevent charge extraction from the perovskite absorber layer, resulting in a lower average PCE of 10.03%.

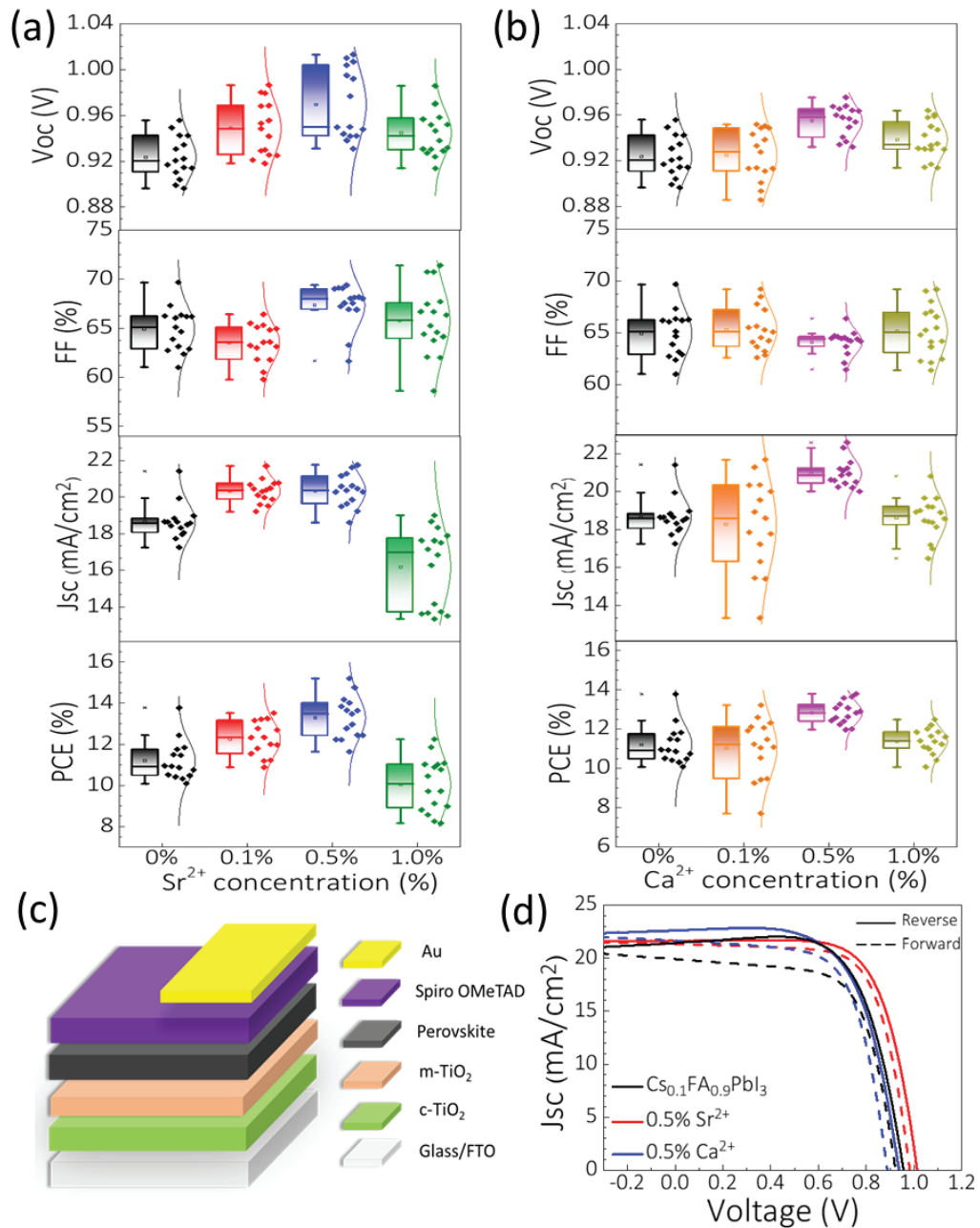


Figure 3.8. Solar cell parameters of Voc, FF, Jsc, and PCE for a) Sr²⁺ and b) Ca²⁺ additive series. c) n-i-p architecture of fabricated solar cells. d) *J-V* curves of PSCs for additive series with the pristine.

When considering the addition of Ca²⁺ which has a lower ionic radius compared to Pb²⁺, the perovskite device performance shows a somewhat similar performance trend to Sr²⁺ added PSCs. However, for 0.1% Ca²⁺ PSCs, the average PCE drops to 11.03% from 11.20% which could be a result of sample-to-sample fluctuation. The maximum average PCE achieved for 0.5% Ca²⁺ PSCs is 12.82% with Voc, FF, and Jsc values of

0.95 V, 64.09%, and 20.95 mA/cm². Lastly, 11.37% of average PCE is obtained in 1.0% Ca²⁺ concentration PSCs.

The device parameters of PSCs change in both cases, showing a similar trend where 0.5% additive concentration yields the maximum values as a result of reduced defect density upon doping as the microstrain calculations suggested. The microstrain decreases monotonically with increasing additive concentration up to 0.5%, which implies lower defect density while the microstrain in the perovskites enhances at 1.0% (Figure 3.3c). Defects in the perovskites significantly affect the photovoltaic devices and lead to lower device performances^{114,125}. Until 0.5% concentrations of the additives, PCEs of the PSCs enhance with increasing Voc and Jsc due to the decreasing defects in the perovskites. For 1.0% Sr²⁺ and Ca²⁺ PSCs, there is a decrease in device performance; however, there are fluctuations in the FF of PSCs. At this point, considering microstrain calculation, an increase in defect concentration is observed at 1.0% Sr²⁺ and Ca²⁺ PSCs.

Table 3.3. Average device parameters of pristine, Sr²⁺, and Ca²⁺ additive PSCs for reverse and forward scan.

PSCs	Scan direction	PCE [%]	Jsc [mA cm ⁻²]	Voc [V]	FF [%]	Hysteresis [%]
Cs _{0.1} FA _{0.9} Pb ₃	Reverse	11.20	18.66	0.92	64.92	14.40
Cs _{0.1} FA _{0.9} Pb ₃	Forward	9.60	16.85	0.88	64.21	
0.1% Sr ²⁺	Reverse	12.25	20.32	0.94	63.50	5.28
0.1% Sr ²⁺	Forward	11.61	19.50	0.90	65.87	
0.5% Sr ²⁺	Reverse	13.29	20.34	0.96	67.37	7.60
0.5% Sr ²⁺	Forward	12.30	19.37	0.93	67.72	
1.0% Sr ²⁺	Reverse	10.03	16.18	0.94	65.79	17.23
1.0% Sr ²⁺	Forward	8.28	14.53	0.91	62.64	
0.1% Ca ²⁺	Reverse	11.03	18.27	0.92	65.28	12.70
0.1% Ca ²⁺	Forward	9.71	16.72	0.87	65.45	
0.5% Ca ²⁺	Reverse	12.82	20.95	0.95	64.09	5.51
0.5% Ca ²⁺	Forward	12.21	20.09	0.91	66.66	
1.0% Ca ²⁺	Reverse	11.37	18.61	0.93	65.15	12.58
1.0% Ca ²⁺	Forward	9.96	16.99	0.89	65.27	

Microstrain calculation results for determining the change in defect concentrations are compatible with device performance of the PSCs and hysteresis of J-V curves. Hysteresis index box plots in J-V curves of the PSCs are shown in Figure 3.10. Average

hysteresis indices and device parameters obtained from reverse and forward scans are plotted as box plot in Figure 3.9 and given in Table 3.3. Hysteresis indexes in $J-V$ curves for the perovskite by Sr^{2+} and Ca^{2+} have been reduced and the lowest average hysteresis index is obtained at 0.5% concentration for both additive series as shown in Figure 3.8d. The hysteresis resulting from mostly ion migration which is faster at the grain boundaries due to higher ionic diffusivity¹²⁶ is reduced for Sr^{2+} and Ca^{2+} PSC series by passivation effects of SrI_2 and CaI_2 .

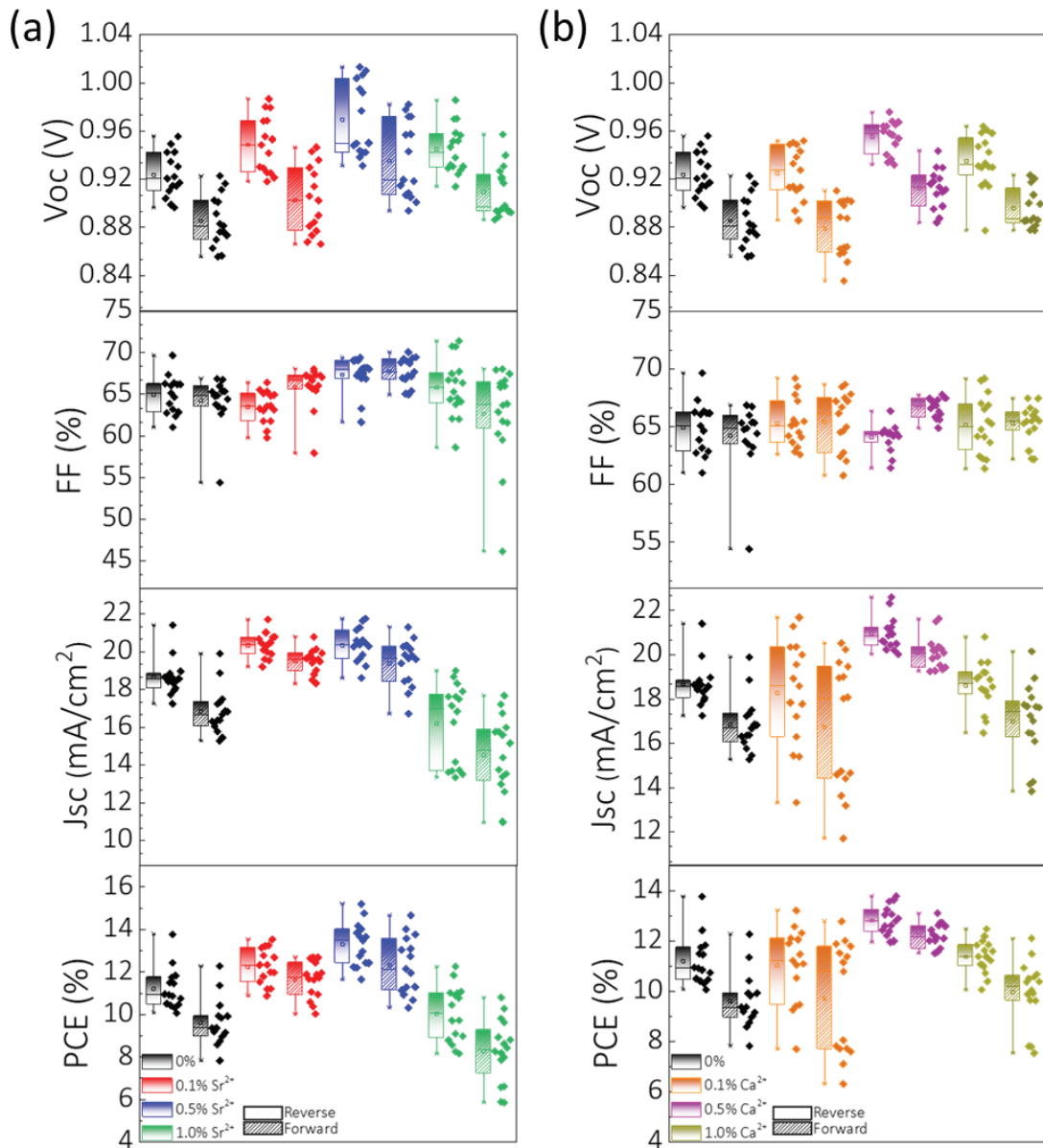


Figure 3.9. Calculated solar cell parameters of V_{oc} , FF, J_{sc} , and PCE from reverse and forward $J-V$ curves for a) Sr^{2+} and b) Ca^{2+} PSCs.

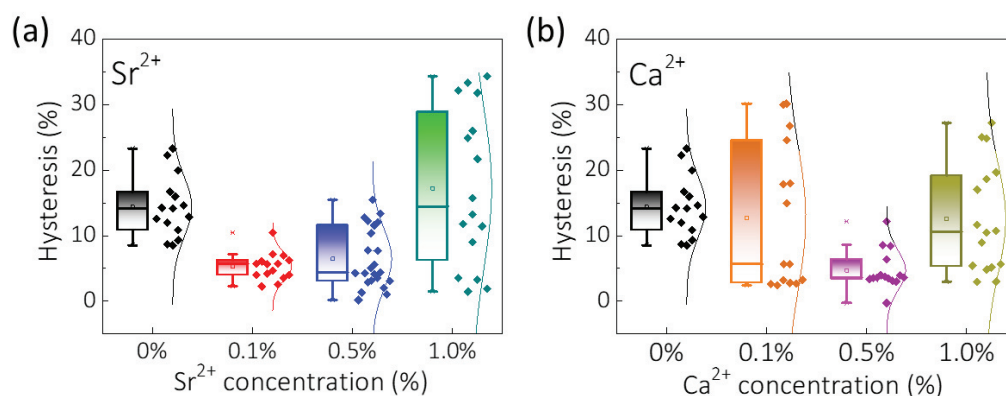


Figure 3.10. Hysteresis indices in the J-V curves of a) Sr²⁺ and b) Ca²⁺ additive series.

3.4. Conclusion

Additive engineering on CsFA-PSCs utilizing Sr²⁺ and Ca²⁺ metal halide additives at low concentrations has been performed. The additives cause uniformity in the grain structure at 0.5% which is assigned as the optimum additive concentration. Microstrain calculations show the defect densities in the perovskite films reduce until 0.5% concentration. Furthermore, the additives cause improvements in optical parameters of the perovskites as well. Finally, the performance of the PSCs is increased by the additives due to lowered defect density with uniform morphologies and enhanced optical properties. At the 0.5% additive concentration, PCEs of the PSCs are significantly improved by Sr²⁺ and Ca²⁺; however, the effect of Sr²⁺ for the improvement of PSCs is superior compared to that of Ca²⁺ with a champion PCE of 15.20%. Furthermore, the hysteresis in PSCs is reduced by utilizing metal halide passivation at grain boundaries. The results show that metal halide additive engineering is a promising strategy to counter the problems of MA-free CsFA PSCs.

CHAPTER 4

IMPROVING PHOTOPHYSICAL PROPERTIES OF PEROVSKITE NANOCRYSTALS FOR WHITE LIGHT EMITTING DIODES

4.1. Introduction

All-inorganic lead halide perovskite nanocrystals (NCs), e.g., CsPbX₃ (X = Cl⁻, Br⁻, I⁻) have found a number of potential roles in a variety of applications including LEDs^{62,127,128}, solar cells^{129,130}, lasers^{131,132}, and photodetectors^{133,134}. In addition to the key properties pursued by these applications such as high photoluminescence quantum yield (PLQY), defect tolerance, adjustable bandgaps, narrow photoluminescence (PL), and the low cost of these materials makes them significantly attractive^{38,135,136}. Despite these promising properties, there are still some issues of halide perovskite NCs face for real-world applications. In addition to the stability, another main problem is the halide defects decreasing the PLQY of perovskite NCs by promoting non-radiative recombination^{137,138}. In order to overcome these problems, a proper surface passivation method by using polymers or inorganic ligands^{139,140} was applied; however, these surface passivation materials limit their application in optoelectronic devices due to their poor conductivities. Compositional engineering is also another effective method to increase the stability and defect elimination resulting in improved optoelectronic properties of perovskite NCs^{34,138,141}. This method can be performed with homovalent dopants, such as Zn²⁺^{142,143}, Cd²⁺^{142,144}, Mn²⁺^{145,146}, and Sn²⁺^{142,147} and heterovalent dopants, such as Ce³⁺¹⁴⁸, Bi³⁺¹⁴⁹, Sb³⁺¹⁵⁰, and Al³⁺¹⁵¹. In addition, Sr²⁺ homovalent dopants for CsPbI₃ perovskite NCs improve the stability and optical properties by increasing defect formation energy^{52,53}. Mn²⁺ incorporation into perovskite lattice leads to optically interesting behavior, which results in a mid-gap state in band structure that belongs to the Mn²⁺, which affects the recombination dynamics¹⁵². Mn-doped perovskites exhibit two PL emissions: one just below the bandgap (~2.4 eV for CsPbBr₃ or ~3.0 eV for CsPbCl₃), assigned to exciton recombination in the perovskite, and another one in orange/red region

at around 2.06 eV¹⁵³, assigned to the Mn *d-d* transition between the ⁴T1 and ⁶A1 configurations^{30,152}.

For perovskite NC-based white light-emitting diodes (WLEDs), CsPbX₃ NCs can be employed to obtain white light with the combination of the emissions in red-green-blue regions^{28,62}. In order to obtain PL emission in the red region, Mn-doped perovskite NCs are a promising alternative to CsPbI₃ NCs which suffer from thermodynamic instability at room temperature³⁸. CsPbBr₃ exhibits better phase stability compared to CsPbI₃ NCs²⁸. A low PLQY of Mn state emission is still a problem for commercialized usage; however, Bi³⁺¹⁵⁴, Co²⁺¹⁵⁵, Ni²⁺¹⁵⁶, Yb³⁺¹⁵⁷, and Cu²⁺¹⁵⁸ co-dopants are used for improving the PLQY of Mn state emission in Mn²⁺-doped perovskite NCs.

In this work (Yuce H. et al)¹⁵⁹, the improved photophysical properties of CsPbBr₃ and Mn²⁺:CsPb(Br,Cl)₃ perovskite NCs by Sr²⁺ incorporation are reported. Firstly, Sr²⁺ dopant at 1%, 2%, 5%, and 10% concentrations in CsPbBr₃ NCs was optimized. In order to find the optimum Sr²⁺ dopant concentration, a series of doped samples ranging from 1% to 10% Sr²⁺ concentration was explored, and the highest PLQY was observed at a 2% dopant concentration. With the goal of harnessing emission in the red region, the 2% Sr²⁺ sample was further doped with MnCl₂ yielding Mn²⁺:CsPb(Br,Cl)₃ NCs. The effects of Sr²⁺ doping on the morphology and crystal structure of CsPbBr₃ and Mn²⁺:CsPb(Br,Cl)₃ perovskite NCs were investigated. A remarkable increase in PLQY and PL lifetime for Sr²⁺:CsPbBr₃ and Mn²⁺:CsPb(Br,Cl)₃ NCs have been observed. Lastly, the Sr²⁺-doped perovskite NCs having enhanced optoelectronic performance have been applied in a white LED fabrication, which shows higher performance with improved white light.

4.2. Experimental Procedure

Materials: Lead(II) bromide (PbBr₂, ≥98%), strontium bromide (SrBr₂, 99.99% trace metal basis), Manganese(II) chloride tetrahydrate (MnCl₂·4H₂O, ≥98%) cesium carbonate (Cs₂CO₃, 99.9%, Sigma-Aldrich), 1-octadecene (ODE, 90%), oleylamine (OLAM, 70%), and oleic acid (OA, 90%) were purchased from SigmaAldrich. Toluene (≥99%, Merck) was purchased and used without any further purification.

Synthesis of Cs – Oleate: for 203.5 mg (266.67 mg) Cs₂CO₃, 625 μL (1,167 μL) oleic acid, and 10 mL 1-octadecene were put into a round bottom flask and dried at 120 °C while stirring for 1 h. After drying the temperature was increased to 150 °C under a

nitrogen atmosphere. The solution was kept at 150 °C overnight to make sure all Cs_2CO_3 reacted with oleic acid. The values given in parentheses are for Cs-Oleate synthesis of pristine and $\text{Sr}^{2+}:\text{Mn}^{2+}:\text{CsPb}(\text{Br},\text{Cl})_3$ NCs.

Synthesis of pristine and $\text{Sr}^{2+}:\text{CsPbBr}_3$ NCs: For the synthesis of pristine CsPbBr_3 NCs, first, 17.2 mg PbBr_2 was put into a glass tube alongside 1.25 mL ODE, 125 μL OA, and 125 μL OLAM and dissolved/degassed at 120 °C for 30 minutes. After degassing, the temperature was increased to 180 °C where 100 μL Cs-oleate was injected. After injection, the solution was immediately cooled down using an ice bath and then centrifuged for 15 min at 6000 rpm (Figure 4.1a). For the synthesis of $\text{Sr}^{2+}:\text{CsPbBr}_3$ NCs, the same procedure was followed except 1%, 2%, 5%, and 10% SrBr_2 was added to the solution while the same molar amount of PbBr_2 was excluded (Figure 4.1b).

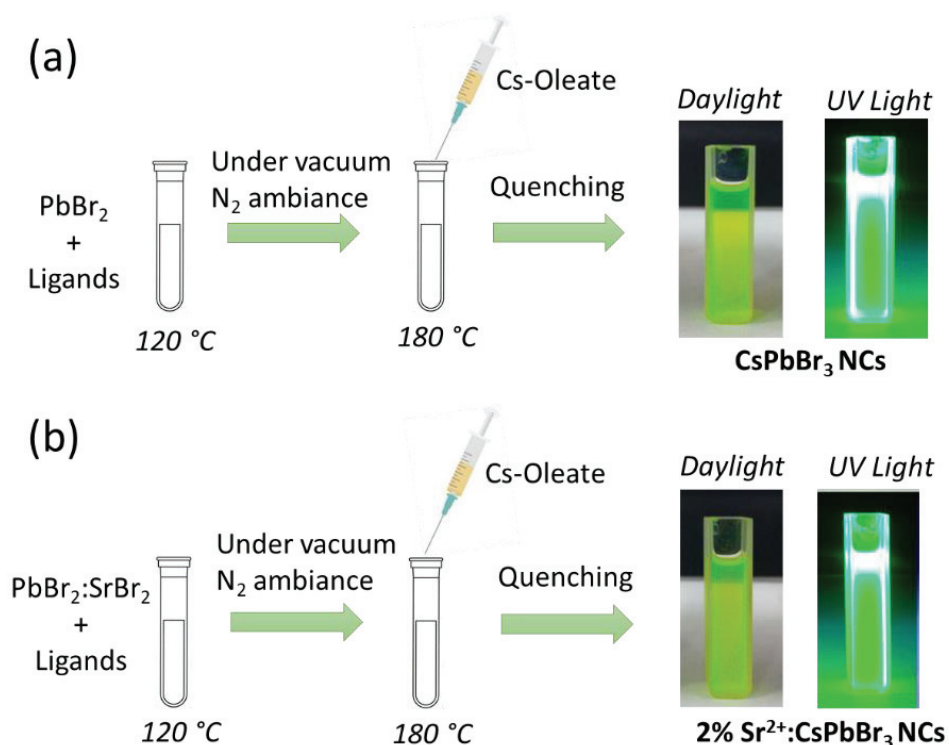


Figure 4.1. Illustration of a) CsPbBr_3 and b) $\text{Sr}^{2+}:\text{CsPbBr}_3$ perovskite NCs synthesis with their images under daylight and UV light.

Synthesis of $\text{Mn}^{2+}:\text{CsPb}(\text{Br},\text{Cl})_3$ and $\text{Sr}^{2+}:\text{Mn}^{2+}:\text{CsPb}(\text{Br},\text{Cl})_3$ NCs: For the synthesis of $\text{Mn}^{2+}:\text{CsPb}(\text{Br},\text{Cl})_3$ NCs, firstly 9.175 mg PbBr_2 and 4.95 mg $\text{MnCl}_2 \cdot 4\text{H}_2\text{O}$ were put into a glass tube alongside with 1.25 mL ODE, 125 μL OA, and 125 μL OLAM and dissolved/degassed at 120 °C for 30 minutes. After degassing, the temperature was

increased to 180 °C where 100 μ L Cs-oleate was injected. After injection, the solution was immediately cooled down using an ice bath and then centrifuged for 15 min at 6000 rpm (Figure 4.2a). For the synthesis of $\text{Sr}^{2+}:\text{Mn}^{2+}:\text{CsPb}(\text{Br},\text{Cl})_3$ NCs, the same procedure was followed except 2% SrBr_2 was added to the solution while the same molar amount of PbBr_2 was excluded (Figure 4.2b).

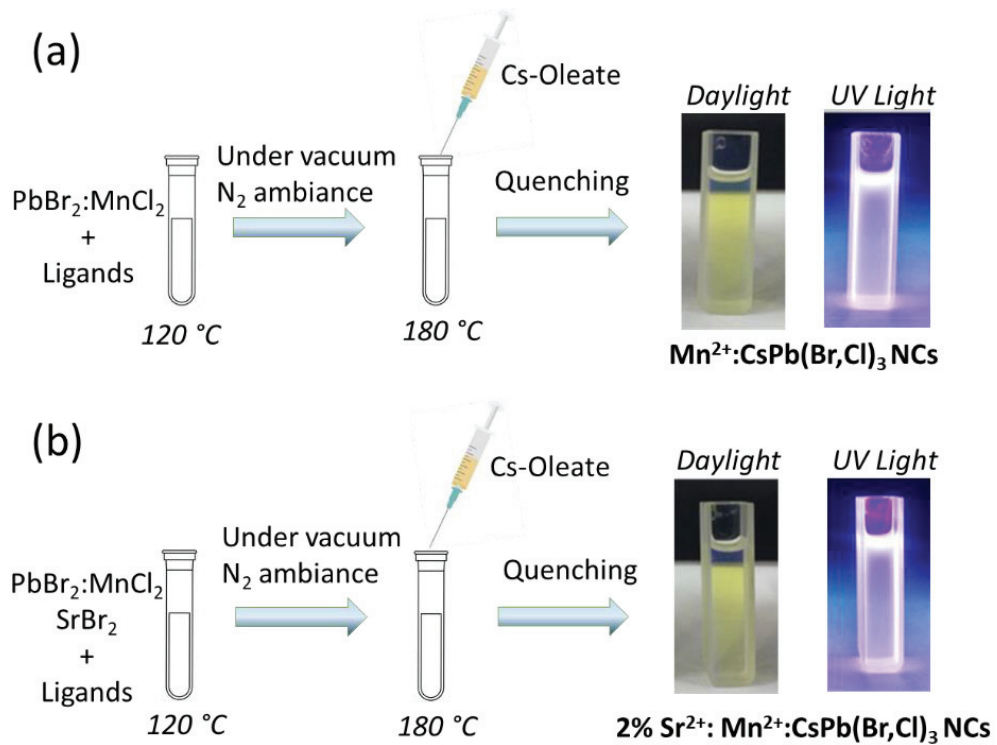


Figure 4.2. Illustration of a) $\text{Mn}^{2+}:\text{CsPb}(\text{Br},\text{Cl})_3$ and b) $2\% \text{Sr}^{2+}:\text{Mn}^{2+}:\text{CsPb}(\text{Br},\text{Cl})_3$ perovskite NCs synthesis with their images under daylight and UV light.

Fabrication of perovskite NCs- based WLED: 0.5 g poly(methyl methacrylate) (PMMA) was dissolved in 10 mL Toluene. For each film of CsPbBr_3 drop cast films were prepared with the mixture of 40 μ L PMMA and 120 μ L perovskite while $\text{Mn}^{2+}:\text{CsPb}(\text{Br},\text{Cl})_3$ drop cast films were prepared with the mixture of 40 μ L PMMA and 240 μ L perovskite solution on $1.5 \times 1.5 \text{ cm}^2$ glass substrates (Figure 4.3). Then, these CsPbBr_3 and $\text{Mn}^{2+}:\text{CsPb}(\text{Br},\text{Cl})_3$ (for 0% and 2% Sr^{2+} series separately) were placed on the LED laterally. The emission spectra were taken from the perovskite layers excited with UV light (366 nm of wavelength, 12 V, and 8W power) and a CIE chromaticity diagram was extracted from the OSRAM ColorCalculator program.

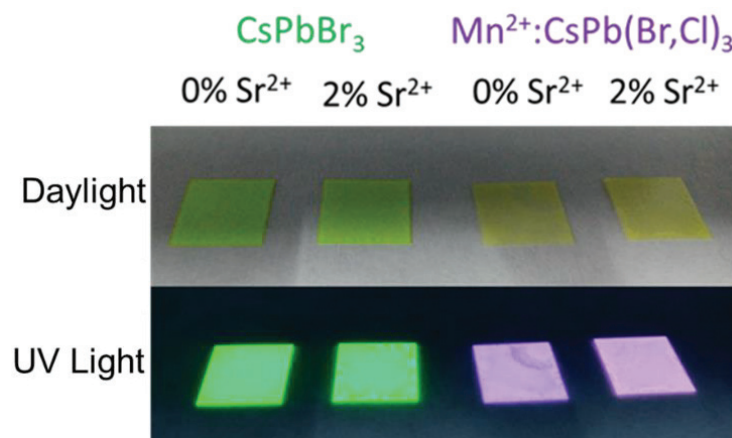


Figure 4.3. Pictures of perovskite NCs/PMMA composite films under daylight and UV light.

Characterization of NCs: STEM images for all perovskite NCs were taken by using a scanning electron microscopy (SEM); Quanta 250, FEI, Hillsboro, OR. Perovskite solutions were dropped onto 300 mesh holey carbon-Cu (50 microns) for STEM images. X-ray diffraction (XRD) analyses were done by using X'Pert Pro, Philips, Eindhoven, the Netherlands. Optical measurements including absorption, PL, PL lifetime, and PLQY were carried out on an FS5 spectrofluorometer (Edinburgh Instruments, U.K.). For PL and PLQY measurements, excitation wavelengths of CsPbBr₃ and Mn²⁺:CsPb(Br,Cl)₃ samples were 400 nm and 390 nm, respectively. For lifetime measurements, CsPbBr₃ and Mn²⁺:CsPb(Br,Cl)₃ samples were excited with 442 nm and 307 nm lasers, respectively. Trace metal analysis was carried out using an inductively Coupled Plasma-Mass Spectrometer (ICP-MS) on Agilent 7500ce Octopole Reaction System.

4.3. Results and Discussion

4.3.1 Elemental Analysis

Inductively Coupled Plasma-Mass Spectrometer (ICP-MS) measurements as shown in Figure 4.4 (Table 4.1) were firstly carried out in order to determine actual doping ratio of Sr/Pb for CsPbBr₃ NCs and the ratios were estimated as 0.0472%, 0.0998%, 0.2388%, 1.0513% for the 1%, 2%, 5%, and 10% Sr²⁺ concentration, respectively. For Mn²⁺:CsPb(Br,Cl)₃ perovskite NCs, actual doping ratio of 2% Sr²⁺ was

estimated as 0.0205% as given in Table 4.2. ICP-MS analysis results show that Sr²⁺ was successfully doped into perovskite NCs and doping concentrations of Sr²⁺ against their addition amounts are in agreement with Sr²⁺:CsPbI₃ NCs⁵³. Br⁻/Cl⁻ ratios were determined as 72.34% and 75.26% for Mn²⁺:CsPb(Br,Cl)₃ and 2% Sr²⁺: Mn²⁺:CsPb(Br,Cl)₃ by ion chromatography (IC) analysis. The large difference in bond dissociation energies between ions prevents the incorporation of dopants into perovskite NCs¹⁴⁵. Considering the bond dissociation energies of Sr-Br (365 kJ/mol) and Sr-Cl (409 kJ/mol)^{160,161}, incorporated Sr²⁺ within lattice could be favoring doping of Br⁻ compared to the Cl⁻.

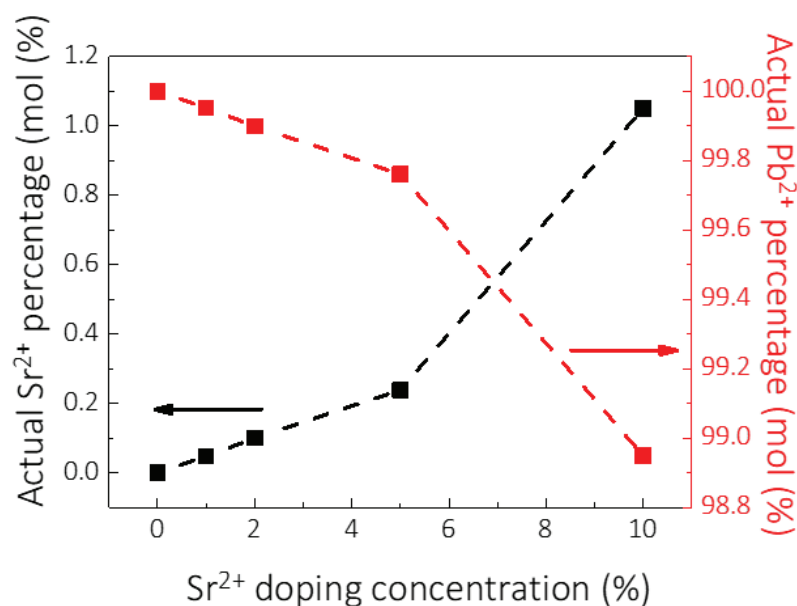


Figure 4.4. Actual Sr²⁺ and Pb²⁺ percentages depending on the added Sr²⁺ concentrations for CsPbBr₃ NCs as obtained by ICP-MS.

Table 4.1. Actual Sr²⁺/ Pb²⁺+Sr²⁺ for Sr²⁺:CsPbBr₃ NCs (determined by ICP-MS).

Sample	Sr ²⁺ /(Pb ²⁺ +Sr ²⁺) (%)
1% Sr ²⁺ :CsPbBr ₃	0.0472
2% Sr ²⁺ :CsPbBr ₃	0.0998
5% Sr ²⁺ :CsPbBr ₃	0.2388
10% Sr ²⁺ :CsPbBr ₃	1.0513

Table 4.2. Actual mole ratio (%) of Sr^{2+} and $\text{Mn}^{2+}/\text{Pb}^{2+}+\text{Mn}^{2+}+\text{Sr}^{2+}$ (determined by ICP-MS) and Br^-/Cl^- (determined by IC) for $\text{Mn}^{2+}:\text{CsPb}(\text{Br},\text{Cl})_3$ NC samples.

Sample	$\text{Sr}^{2+}/(\text{Pb}^{2+}+\text{Mn}^{2+}+\text{Sr}^{2+})$ (%)	$\text{Mn}^{2+}/(\text{Pb}^{2+}+\text{Mn}^{2+}+\text{Sr}^{2+})$ (%)	Br^-/Cl^- (%)
0% $\text{Sr}^{2+}:\text{Mn}^{2+}:\text{CsPb}(\text{Br},\text{Cl})_3$	-	0.2525	72.34
2% $\text{Sr}^{2+}:\text{Mn}^{2+}:\text{CsPb}(\text{Br},\text{Cl})_3$	0.0205	0.2406	75.26

4.3.2. Morphology of CsPbBr_3 NCs

The morphology and size distribution of CsPbBr_3 NCs upon Sr^{2+} doping was monitored via STEM mode in SEM. The incorporation of Sr^{2+} ions into the perovskite lattice does not clearly affect the structure and morphology of the perovskite NCs (Figure 4.5). From the STEM images in Figure 4.5, the average NC sizes of pristine, 1%, 2%, 5%, and 10% Sr^{2+} -doped CsPbBr_3 NCs were found to be ~ 20.3 , ~ 16.8 , ~ 17.3 , ~ 16.0 , and ~ 17.0 nm, respectively. While a systematic reduction of perovskite NC size corresponding to an increasing Sr^{2+} ion concentration was not observed, in general, however, the CsPbBr_3 NCs experienced a reduction in nanoparticle size due to Sr^{2+} doping. Passivation by excess halide ions has been reported to cause a lower size distribution in perovskite NCs^{162,163}, however, the reason for the decrease in NC size upon Sr^{2+} doping can be an effect of impurity (i.e., the dopant) on crystallization dynamics, since the synthesized perovskite NCs are stoichiometric in this work. It is argued that the Sr^{2+} impurities lead to a reduction of the energy threshold for nucleation and cause more nuclei to form, resulting in a smaller NC size. The uniformity of NC size distribution is improved upon Sr^{2+} doping until 2% Sr^{2+} concentration, however, even higher Sr^{2+} concentrations adversely affect NC homogeneity (Figure 4.5b-e insets).

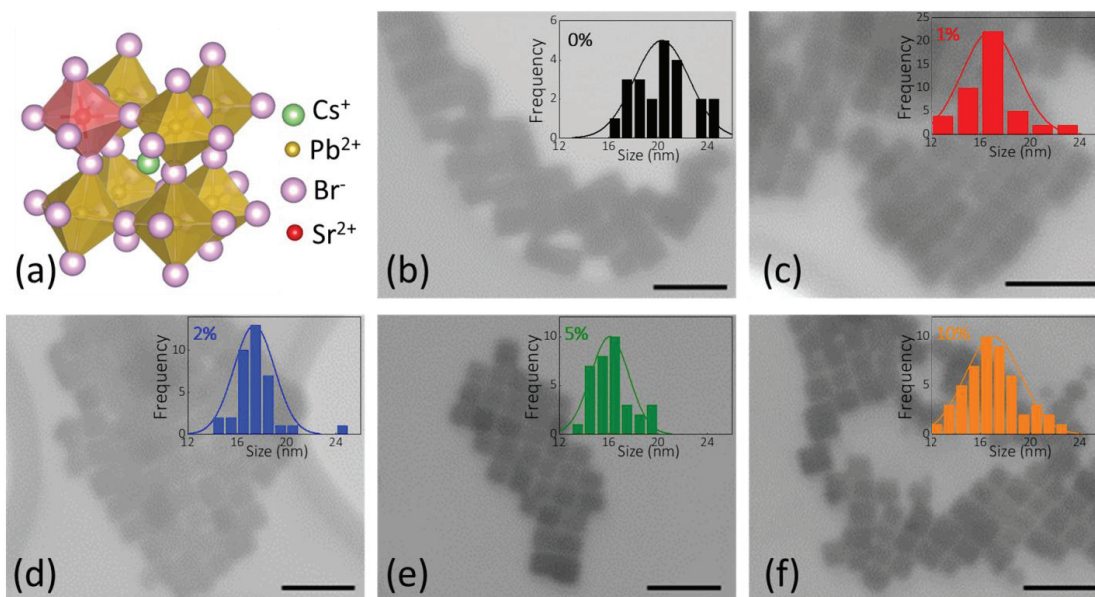


Figure 4.5. a) Illustration of Sr²⁺-doping into CsPbBr₃ crystal lattice and STEM images of b) 0%, c) 1%, d) 2%, e) 5%, and f) 10% Sr²⁺ doped CsPbBr₃ NCs. All inset in each figure shows NC size distribution in the relevant sample. Bar size is 50 nm.

4.3.3. Structural and Optical Properties of CsPbBr₃ NCs

Figure 4.6a shows the XRD patterns of pristine and Sr²⁺:CsPbBr₃ NC samples. XRD reflections for all samples confirm the orthorhombic Pnma crystal structure of CsPbBr₃¹⁶⁴. Incorporation of Sr²⁺ to perovskite lattice does not cause any additional XRD reflection, confirming no phase transition upon doping. Furthermore, no systematic shift in XRD reflections was observed upon Sr²⁺ doping due to the similar ionic radii of Pb²⁺ (119 pm) and Sr²⁺ (118 pm) ions¹¹³. In order to understand the effect of Sr²⁺ doping on the perovskite lattice, the lattice parameters were calculated by using XRD patterns of each sample as given in Table S4.1. The lattice parameters (a, b, c unit cell) show a trend where “a= 8.27680 Å” and “c= 8.19181 Å” values increase and reach a maximum at 2% Sr²⁺ doping concentration and then decrease as the doping concentration exceeds 2% (Figure 4.6b) whereas “b” lattice parameter follows an opposite trend. The absence of a systematic shift in XRD patterns (i.e. homogeneous strain) has led to an investigation of microstrain depending on the doping concentration. Microstrain describes a local distortion of the crystal lattice, which was calculated by the slope of the Williamson-Hall (W-H) plot obtained by the XRD reflection broadness of the samples in Figure S4.1

(Table S4.2)^{79,115}. According to the calculations in Figure 4.6c, microstrain has declined upon Sr²⁺ doping until 2% concentration. For further concentrations, there is a systematic increase in microstrain. This behavior suggests that reduced defect-related distortion in the perovskite NCs at 2% Sr²⁺ could be the result of changed lattice parameters upon doping.

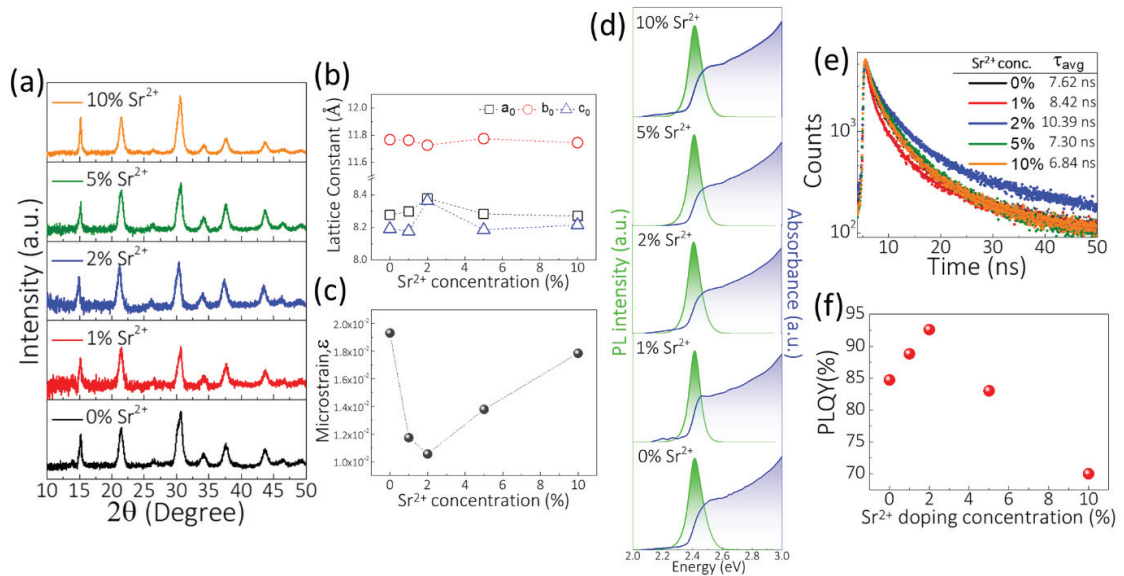


Figure 4.6. a) XRD patterns, b) lattice parameters, c) microstrain values obtained by W-H plot, d) PL/Absorption spectra, e) TRPL plot, and f) PLQY distribution of pristine and Sr²⁺:CsPbBr₃ NCs.

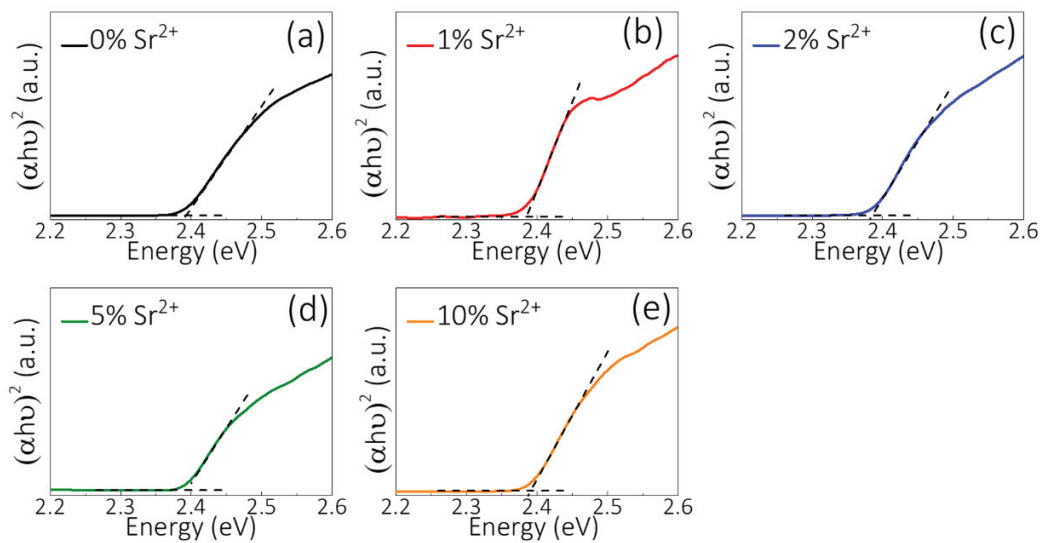


Figure 4.7. Tauc plots of a) pristine, b) 1%, c) 2%, d) 5%, and e) 10% Sr²⁺:CsPbBr₃ NCs with bandgap of 2.39 eV.

In order to understand the doping effect further, optical measurements have been carried out as shown in Figure 4.6d-f. Considering absorption and PL spectra of pristine and Sr²⁺:CsPbBr₃ NCs (Figure 4.5d), there is no shift in PL emission energy and absorption edge of the samples. This implies that the incorporation of Sr²⁺ into the lattice does not affect the bandgap energy of CsPbBr₃. According to Tauc's plot (Figure 4.7), the bandgap energies of the samples are calculated as ~ 2.39 eV. PL signals were centered at 2.41 eV. Furthermore, the full-width half maxima (FWHM) of PL peaks (Figure 4.8) were reduced by the doping of Sr²⁺ which is in agreement with size distribution in STEM images.

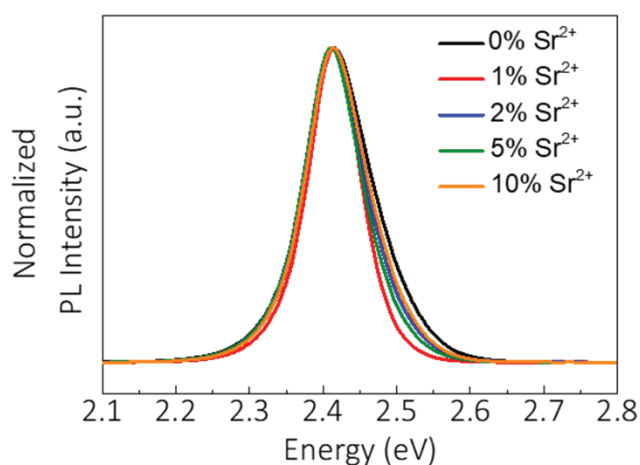


Figure 4.8. PL emissions of pristine, 1%, 2%, 5%, and 10% Sr²⁺:CsPbBr₃ NCs.

The absence of PL shift despite the minor NC size changes can be attributed to the sizes of CsPbBr₃ NCs within intermediate-weak confinement regimes¹⁶⁵. Figure 4.6e shows the TRPL results of CsPbBr₃ NCs with different Sr²⁺ doping amounts. The average PL lifetimes per sample were calculated in Table S4.3 and details are given in Appendix A, Supplementary Note 4. PL lifetime of CsPbBr₃ NCs was measured as 7.62 ns. In the case of the incorporation of Sr²⁺ ions until ≤ 2% to the perovskite NCs, longer average lifetimes were observed. Depending on the doping concentration, there is a systematic increase in the average lifetime which are 8.42 and 10.39 ns for 1% and 2% Sr²⁺-doped CsPbBr₃ NCs, respectively. However, for higher concentrations of Sr²⁺ (>2%), a reduction of lifetimes which are 7.30 ns for 5% and 6.84 ns for 10% Sr²⁺ perovskite NCs was found. Considering the inversely proportional defect-lifetime relationship^{166,167}, the trend in PL lifetimes is in an agreement with calculated microstrain results in Figure 4.6c. According to the microstrain calculations, defect-related distortions were diminished by

incorporation of Sr^{2+} into the lattice until 2% concentration and minimum microstrain originating from fewer defects was determined for 2% Sr^{2+} -doped CsPbBr_3 NCs. Then, with a higher doping amount of Sr^{2+} , a reduction of PL lifetime was observed with increasing microstrain due to higher defect concentration resulting in more non-radiative recombination. The reduced defect density leads to decreased non-radiative recombination, resulting in higher PLQY and PL lifetime¹⁶⁸. The same trend as in PL lifetime and microstrain was observed for PLQY results in Figure 4.6f. The PLQY of CsPbBr_3 NCs was obtained as 84.7%. By doping of Sr^{2+} , PLQY of the perovskite NCs was enhanced to 88.8% and 92.6% at 1% and 2% Sr^{2+} concentrations, respectively. For further doping concentrations, PLQY of the perovskite dropped to 83% at 5% Sr^{2+} and then 70% at 10% Sr^{2+} concentrations since more dopants in the perovskite lattice could trigger the formation of new defects⁵².

4.3.4. Morphology of $\text{Mn}^{2+}:\text{CsPb}(\text{Br},\text{Cl})_3$ NCs

Figure 4.9 shows the STEM images of $\text{Mn}^{2+}:\text{CsPb}(\text{Br},\text{Cl})_3$ and 2% $\text{Sr}^{2+}:\text{Mn}^{2+}:\text{CsPb}(\text{Br},\text{Cl})_3$ NCs. 2% Sr^{2+} incorporation into $\text{Mn}^{2+}:\text{CsPb}(\text{Br},\text{Cl})_3$ lattice is benign to the NC morphology shape-wise. However, a slight decrease in nanocube size and improved monodispersity in size were observed similar to the $\text{Sr}^{2+}:\text{CsPbBr}_3$ case (Figure 4.5). The average NC sizes are 20.6 nm and 19.3 nm for pristine and 2% $\text{Sr}^{2+}:\text{Mn}^{2+}:\text{CsPb}(\text{Br},\text{Cl})_3$, respectively.

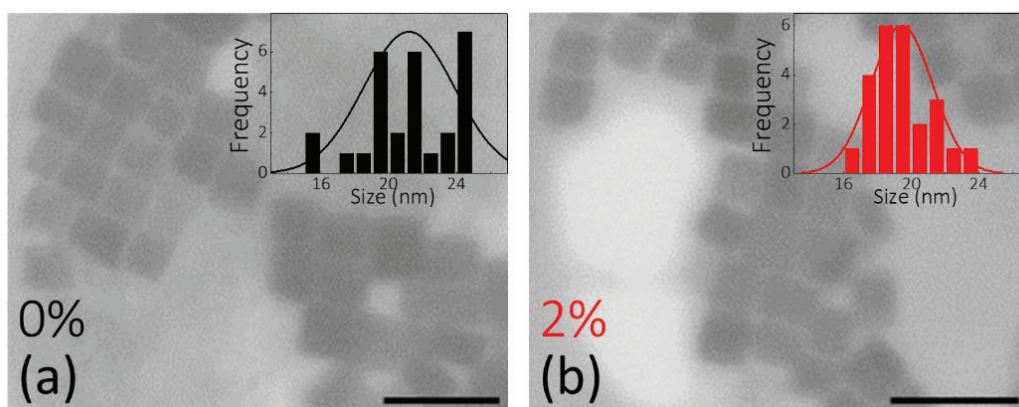


Figure 4.9. STEM images of a) $\text{Mn}^{2+}:\text{CsPb}(\text{Br},\text{Cl})_3$ and b) 2% $\text{Sr}^{2+}:\text{Mn}^{2+}:\text{CsPb}(\text{Br},\text{Cl})_3$ NCs. Bar size is 50 nm.

4.3.5. Structural and Optical Properties of $\text{Mn}^{2+}:\text{CsPb}(\text{Br},\text{Cl})_3$ NCs

XRD analyses for $\text{Mn}^{2+}:\text{CsPb}(\text{Br},\text{Cl})_3$ NCs in order to observe the impact of 2% Sr^{2+} doping on the NCs were carried out as shown in Figure 4.10a. The XRD pattern of $\text{Mn}^{2+}:\text{CsPb}(\text{Br},\text{Cl})_3$ NCs show reflections at 15.4° , 22.0° , 31.1° , 35.0° , 38.4° , and 44.6° which correspond to the orthorhombic perovskite phase¹⁶⁹. Due to the ionic radius difference between Mn^{2+} (67 pm) and Pb^{2+} (119 pm) ions¹¹³, the XRD signal shifted to higher angles for Mn^{2+} -doped perovskite NCs, which indicates Mn^{2+} ions were incorporated into the perovskite lattice¹⁷⁰. Nonetheless, the shift in $\text{Mn}^{2+}:\text{CsPb}(\text{Br},\text{Cl})_3$ is not exclusively due to Pb^{2+} ion substitutions with Mn^{2+} ions, the overall lattice shrinking effect should also be attributable to Cl^-/Br^- substitutions Figure 4.10b²⁸. Sr^{2+} addition into $\text{Mn}^{2+}:\text{CsPb}(\text{Br},\text{Cl})_3$ NCs does not exhibit any peak shift, indicating the Sr^{2+} ions substituted with Pb^{2+} ions in the perovskite NCs.

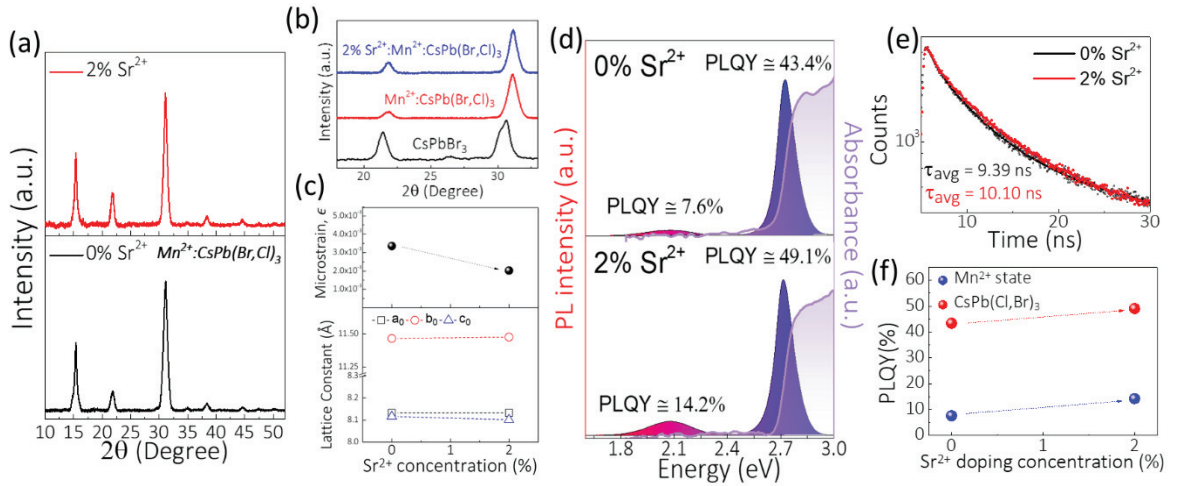


Figure 4.10. a) XRD patterns, b) the comparisons of XRD signal positions for CsPbBr_3 , $\text{Mn}^{2+}:\text{CsPb}(\text{Br},\text{Cl})_3$ and $\text{Sr}^{2+}:\text{Mn}^{2+}:\text{CsPb}(\text{Br},\text{Cl})_3$ perovskite NCs c) microstrain and lattice constant parameters. d) PL/Absorption spectra, e) TRPL plot, and f) PLQY comparisons of $\text{Mn}^{2+}:\text{CsPb}(\text{Br},\text{Cl})_3$ and $2\%\text{Sr}^{2+}:\text{Mn}^{2+}:\text{CsPb}(\text{Br},\text{Cl})_3$ NCs.

Therefore, microstrain calculations of $\text{Mn}^{2+}:\text{CsPb}(\text{Br},\text{Cl})_3$ samples have been performed owing to the narrowing of XRD signals after Sr^{2+} incorporation. Through the doping, the microstrain of $\text{Mn}^{2+}:\text{CsPb}(\text{Br},\text{Cl})_3$ NCs diminishes from 0.33% to 0.20% as shown in Figure 4.10c. In the lattice parameters, b and c exhibit an inversely proportional

trend while “ $a=8.1324 \text{ \AA}$ ” and stays constant by Sr^{2+} doping (Figure 4.10c and Table S4.1). The UV-Vis results in Figure 4.10d show very similar absorption behaviour for $\text{Mn}^{2+}:\text{CsPb}(\text{Br},\text{Cl})_3$ and $2\%\text{Sr}^{2+}:\text{Mn}^{2+}:\text{CsPb}(\text{Br},\text{Cl})_3$ NCs.

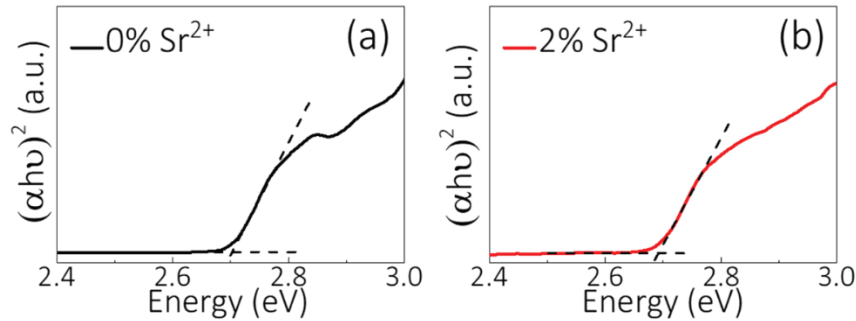


Figure 4.11. Tauc plots of a) $\text{Mn}^{2+}:\text{CsPb}(\text{Br},\text{Cl})_3$ ($E_g = 2.70 \text{ eV}$) and b) $2\%\text{Sr}^{2+}:\text{Mn}^{2+}:\text{CsPb}(\text{Br},\text{Cl})_3$ NCs ($E_g = 2.69 \text{ eV}$).

The Tauc plots of $\text{Mn}^{2+}:\text{CsPb}(\text{Br},\text{Cl})_3$ and $2\%\text{Sr}^{2+}:\text{Mn}^{2+}:\text{CsPb}(\text{Br},\text{Cl})_3$ samples are shown in Figure 4.11, which shows 2.70 and 2.69 eV bandgaps for these samples, respectively. This small variation between the samples was also observed in PL peak positions obtained from excitons where $\text{Mn}^{2+}:\text{CsPb}(\text{Br},\text{Cl})_3$ and $2\%\text{Sr}^{2+}:\text{Mn}^{2+}:\text{CsPb}(\text{Br},\text{Cl})_3$ NCs exhibited exciton PL signals at 2.72 and 2.71 eV, respectively (Figure 4.10d). Since Sr^{2+} doping at low concentrations ($\leq 1\%$) does not cause a change in the bandgap energy (Figure 4.7), this slight change in bandgap and PL emission energies can be attributed to an extremely small variety of Br^-/Cl^- ratio in the perovskite structures. PL emission coming from Mn-state in $\text{Mn}^{2+}:\text{CsPb}(\text{Br},\text{Cl})_3$ perovskite NCs increases by Sr^{2+} doping. TRPL measurement results of these samples are given in Figure 4.10e for exciton emissions of the perovskites. The average PL lifetime of $\text{Mn}^{2+}:\text{CsPb}(\text{Br},\text{Cl})_3$ NCs was increased from 9.39 ns to 10.10 ns by Sr^{2+} doping, indicating lower defect density. As the last optical measurement, PLQY measurements on $\text{Mn}^{2+}:\text{CsPb}(\text{Br},\text{Cl})_3$ and $2\%\text{Sr}^{2+}:\text{Mn}^{2+}:\text{CsPb}(\text{Br},\text{Cl})_3$ NCs have been performed. For these measurements, only the range between 2.38-1.59 eV (520-780 nm) and 3.02-2.38 eV (410-520 nm) were included to see the change in the optical performance of Mn^{2+} -state and perovskite exciton emissions, respectively. As a result, $\text{Mn}^{2+}:\text{CsPb}(\text{Br},\text{Cl})_3$ NCs have a PLQY of 7.6% and they show a remarkable increase in the PLQY reaching up to 14.2% after Sr^{2+} incorporation for $\text{Sr}^{2+}:\text{Mn}^{2+}:\text{CsPb}(\text{Br},\text{Cl})_3$ NCs as given in Figure 4.10f, proving the beneficial effect of Sr^{2+} co-doping alongside with Mn^{2+} . In addition, the exciton

PLQY belonging to the perovskite structure is increased from 43.4% to 49.1% by Sr²⁺ incorporation (Figure 4.10f). These optical improvements with better exciton-to-Mn²⁺ energy transfer due to Sr²⁺ incorporation originated from lowered defect density.

4.3.6. White Light Generation by Using Perovskite NCs

Two sets of WLEDs were fabricated based on CsPbBr₃/PMMA (green-emitting composite) and Mn²⁺:CsPb(Br,Cl)₃/PMMA (red-blue emitting composite) by excitation of a UV LED. In order to observe 2% Sr²⁺ addition effect on the quality of WLED, perovskite NCs/PMMA composite films with and without 2% Sr²⁺ were obtained by drop-casting. Their corresponding PL spectra for 0% Sr²⁺ and 2% Sr²⁺ systems are shown in Figure 4.12a with their CIE coordinates in Figure 4.12b. Since the amount of Mn²⁺:CsPb(Br,Cl)₃ perovskite NCs in the film is higher compared to the amount of CsPbBr₃ NCs, PL emissions of Mn²⁺:CsPb(Br,Cl)₃ are improved more by Sr²⁺ doping compared to the improvement of CsPbBr₃ NCs. The luminescence efficiency of CsPbBr₃/Mn²⁺:CsPb(Br,Cl)₃ based WLED is 277 lm/W under the 8W power of UV light, which is increased to 290 lm/W by Sr²⁺ doping. While the CRI for the undoped perovskite system is 80, 2% Sr²⁺:CsPbBr₃/2% Sr²⁺:Mn²⁺:CsPb(Br,Cl)₃ based WLED exhibit a CRI of 83 due to the increase in PL emission of Mn²⁺ state by decreasing the deficiency of red emission in the system.

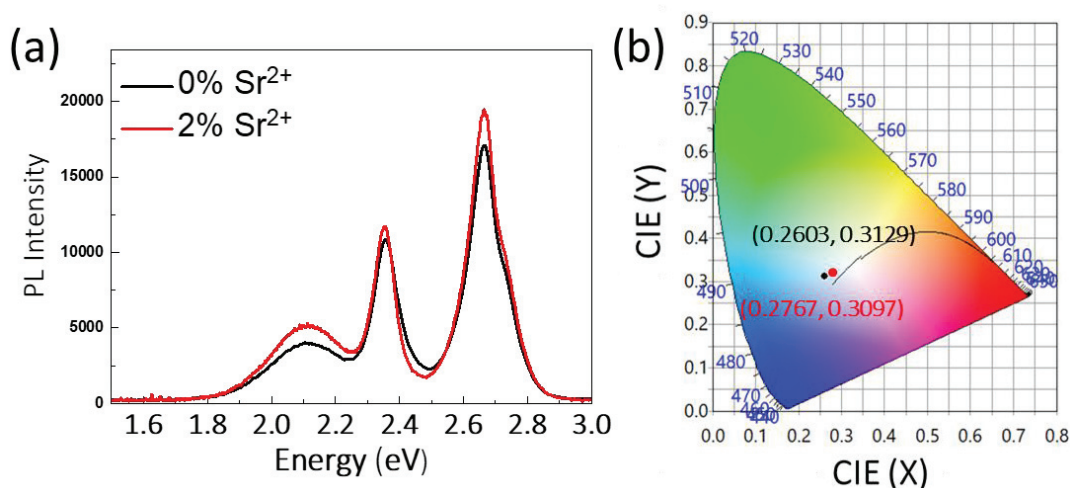


Figure 4.12. PL spectra of WLEDs based on a) 0% and 2% Sr²⁺ doped CsPbBr₃ and Mn²⁺:CsPb(Br,Cl)₃ drop casted films; b) corresponding CIE coordinates.

4.4. Conclusion

A detailed experimental study on Sr^{2+} doping into CsPbBr_3 and $\text{Mn}^{2+}:\text{CsPb}(\text{Br},\text{Cl})_3$ perovskite NCs has been presented. Upon Sr^{2+} doping, a decrease in the NC size of the perovskite was observed by STEM images. The changes in lattice parameters and microstrains were calculated from XRD signals, where microstrain reaches a minimum at 2% Sr^{2+} concentration for CsPbBr_3 NCs possibly due to the elimination of defects. In addition, the improved optical properties with a PLQY of 92.6% increased from 84.7% by reducing non-radiative recombination with fewer defects. Based on the significant results obtained by $\text{Sr}^{2+}:\text{CsPbBr}_3$ NCs, the same strategy to improve the optical properties of $\text{Mn}^{2+}:\text{CsPb}(\text{Br},\text{Cl})_3$ NCs has been employed, which was characterized by the same techniques. The PLQY of Mn^{2+} -state emission is increased to 14.2% from 7.6%. Finally, improved 2% Sr^{2+} -doped CsPbBr_3 and $\text{Mn}^{2+}:\text{CsPb}(\text{Br},\text{Cl})_3$ NCs were used to build a WLED system resulting in improved white light compared to the WLED build with pristine perovskite NC counterparts. It is shown that Sr^{2+} doping is a very effective method to make CsPbBr_3 and $\text{Mn}^{2+}:\text{CsPb}(\text{Br},\text{Cl})_3$ perovskite NCs more optically active.

CHAPTER 5

INCREASED STABILITY OF PEROVSKITE NANOCRYSTALS BY LIGAND ENGINEERING

5.1. Introduction

In terms of their optoelectronic properties, useful black phases of CsPbI₃ with α (cubic), β (tetragonal) or γ (orthorhombic) require high temperatures to maintain their stability^{171,172}. Thermodynamic instability of black CsPbI₃ phases at low temperatures in ambient conditions limits their usage in optoelectronic devices^{173,174}. Since the first synthesis of inorganic lead halide perovskite NCs, oleic acid (OA) and oleylamine (OLAM) have been the most popular ligand pair for these materials²⁸. One common issue regarding lead halide perovskite NCs is the phase instability of CsPbI₃ NCs, especially under ambient conditions¹⁷¹. Phase instability of the perovskite NCs is caused by the small size of the Cs⁺ cation and is facilitated by humidity. The dynamic nature of the ligand binding to lead halide perovskite NC surfaces increases the risk of ligand detachment and faster phase transition of CsPbI₃ NCs¹⁷⁵. This detachment can occur during the purification steps or upon exposure to polar solvents or the atmosphere. The sizes of long-chain OA and OLAM ligands limit the potential optoelectronic applications of LHP NCs due to blocked charge carrier transport¹⁷⁶.

To overcome the phase instability of CsPbI₃ NCs, methods such as forming octahedral tilting by doping the perovskite lattice with impurities^{177,178} or ligand engineering to increase the passivation to protect the structure from ambient air are implemented^{31,179}. Also, hydrophobic ligands in perovskites are used to hinder the effect of humidity on CsPbI₃ NCs¹⁸⁰. Therefore, it is crucial to dig deeper into these mechanisms to achieve stable CsPbI₃ NCs with good optoelectronic properties.

In this study, 4-hydroxybenzoic acid (4-HBA) was used as an additive to the standard OA and OLAM ligand pair in order to improve the optical properties and α -phase stability of CsPbI₃ NCs. The hydrophobic feature of 4-HBA¹⁸¹ causes the protection of CsPbI₃ NCs in the ambient atmosphere or polar solvent conditions, resulting in improved stability. It was also revealed that octahedral tilting due to increased

compressive strain within the CsPbI₃ crystal lattice is another possible reason for this improvement by using x-ray diffraction (XRD) and tracking the strain within the CsPbI₃ crystal lattice. Time-resolved photoluminescence (TRPL) studies showed that the 4-HBA addition decreases the non-radiative carrier lifetimes. The stability of CsPbI₃ NCs under ambient conditions by periodic PL and absorption optical measurements was tested. This study shows the effect of 4-HBA ligand addition at different concentrations on CsPbI₃ perovskite NCs and significantly improved perovskite phase stability of CsPbI₃ NCs in addition to improved optical properties.

5.2. Experimental Procedure

Materials: Lead (II) iodide (PbI₂, 99%), cesium carbonate (Cs₂CO₃, 99.9%), 1-octadecene (ODE, 90%), oleylamine (OLAM, 70%), oleic acid (OA, 90%), and 4-Hydroxybenzoic acid (HBA, ≥99%) were purchased from SigmaAldrich. Toluene (≥99%, Merck) was purchased and used without any further purification.

Synthesis of Cs-Oleate was carried out the same way as described in Chapter 4.2.

Synthesis of CsPbI₃ NCs: For the synthesis of pure CsPbI₃ NCs, first, 21.7 mg PbI₂ (0.047 mmol) was put into a glass tube alongside 1.25 mL ODE, 125 μL OA, and 125 μL OLAM and dissolved/degassed under vacuum at 120 °C for 10 minutes. After degassing, the temperature of the solution was increased to 160 °C under a nitrogen atmosphere and 100 μL Cs-oleate was injected. After 10 seconds of Cs-oleate injection, the solution was cooled down with an ice bath. In order to remove the residuals, the perovskite solution was centrifuged at 9000 rpm for 10 min after cooling to room temperature. Finally, perovskite NCs were dispersed in toluene (Figure 5.1a). For the synthesis of CsPbI₃ NCs with 4-HBA, the same procedure was followed with the addition of 2.5%, 5%, 10%, and 20% mmol of 4-HBA to the OA (Figure 5.1b).

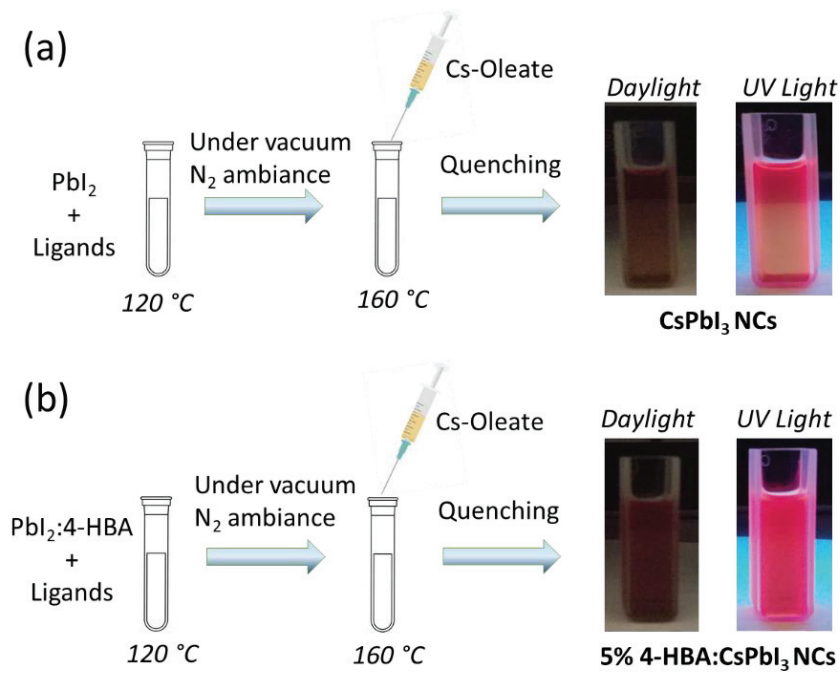


Figure 5.1. Illustration of a) CsPbI₃ and b) 5% 4-HBA:CsPbI₃ perovskite NCs synthesis with their images under daylight and UV light.

Methods: STEM images for all perovskite samples were taken by using the STEM mode of scanning electron microscopy (SEM); Quanta 250, FEI, Hillsboro, OR. Perovskite solutions were dropped onto 300 mesh holey carbon-Cu (50 μ L) for STEM images. X-ray diffraction (XRD) analyses were done by using PANalytical Empyrean using Cu K α radiation ($\lambda = 1.54$ nm) with a scan step size of 0.013 $^\circ$. Optical measurements including absorption, PL, and TRPL were carried out on a spectrophotometer (UV-2550 Shimadzu, Kyoto, Japan), a fluorescence spectrophotometer (Varian Carry-Eclipse), and an FS5 spectrofluorometer (Edinburgh Instruments, U.K.). For PL measurements, the excitation wavelength was 480 nm. For lifetime measurements, CsPbI₃ NCs were excited with a 561 nm laser.

5.3. Results and Discussion

5.3.1. Morphological and Structural Analysis

STEM images of CsPbI₃ NCs with 0%, 2.5%, 5%, 10%, and 20% 4-HBA additives are shown in Figure 5.2. Pristine CsPbI₃ NCs show the standard nanocube

morphology with an average size distribution of ~ 26.5 nm (Figure S5.1). As the 4-HBA concentration rises, a slight change in the morphology of perovskite NCs was observed. The reason for the change in the morphology could be the formation of the γ -CsPbI₃ phase or polyhedral perovskite NCs. This kind of effect was observed on CsPbI₃ particles passivated with imidazolium resulting in γ -CsPbI₃¹⁸². In addition, NCs aggregation was observed by the increasing concentration of 4-HBA.

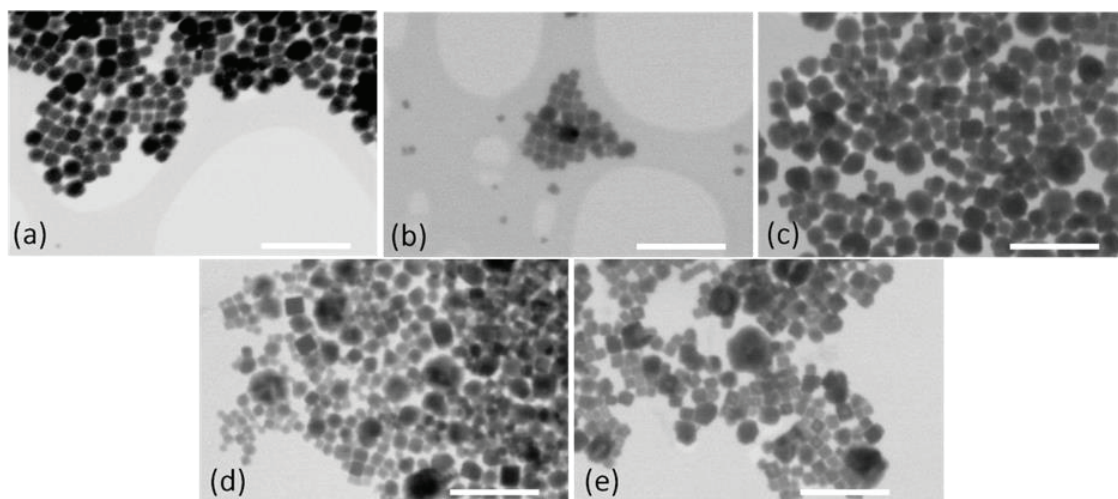


Figure 5.2. STEM images of perovskite samples, for a) 0%, b) 2.5%, c) 5.0%, d) 10%, and e) 20% 4-HBA perovskites. Bar size is 200 nm.

XRD measurements were carried out in order to understand the effect of 4-HBA on the crystal structure of CsPbI₃ NCs. Figure 5.3 shows the XRD analysis results of CsPbI₃ NCs with 0%, 2.5%, 5%, 10%, and 20% 4-HBA additives. The XRD pattern of the pristine CsPbI₃ NCs exhibits peaks at 14.12°, 20.10°, and 28.62° which correspond to the cubic α -phase of CsPbI₃ with $Pm\bar{3}m$ symmetry¹⁷². As the 4-HBA percentage increases, the reflection at 28.5° shifts to higher scattering angles which indicate compressive strain on the lattice.

The XRD reflections of the CsPbI₃ NCs evolve into a new pattern upon the emergence of new peaks for 4-HBA added samples that belong to the γ -CsPbI₃ phase. Also, the weak α -CsPbI₃ phase signals at around 20°, 32°, 35°, and 40° were gradually intensified with increasing 4-HBA addition. This changing trend indicates that the CsPbI₃ NCs undergo octahedral tilting due to increased strain with increasing 4-HBA amount. This tilting leads to the formation of the orthorhombic γ -CsPbI₃ phase with $Pnam$ symmetry and the peaks of the γ -CsPbI₃ phase become more intense with increasing 4-

HBA amount. Therefore, it can be said that 4-HBA addition yields CsPbI₃ NCs with a mixture of α - and γ -phases. The octahedral tilting was reported to be the reason for better stability and optical properties for CsPbI₃¹⁸³ and 4-HBA addition to the CsPbI₃ synthesis could be improving the NC quality.

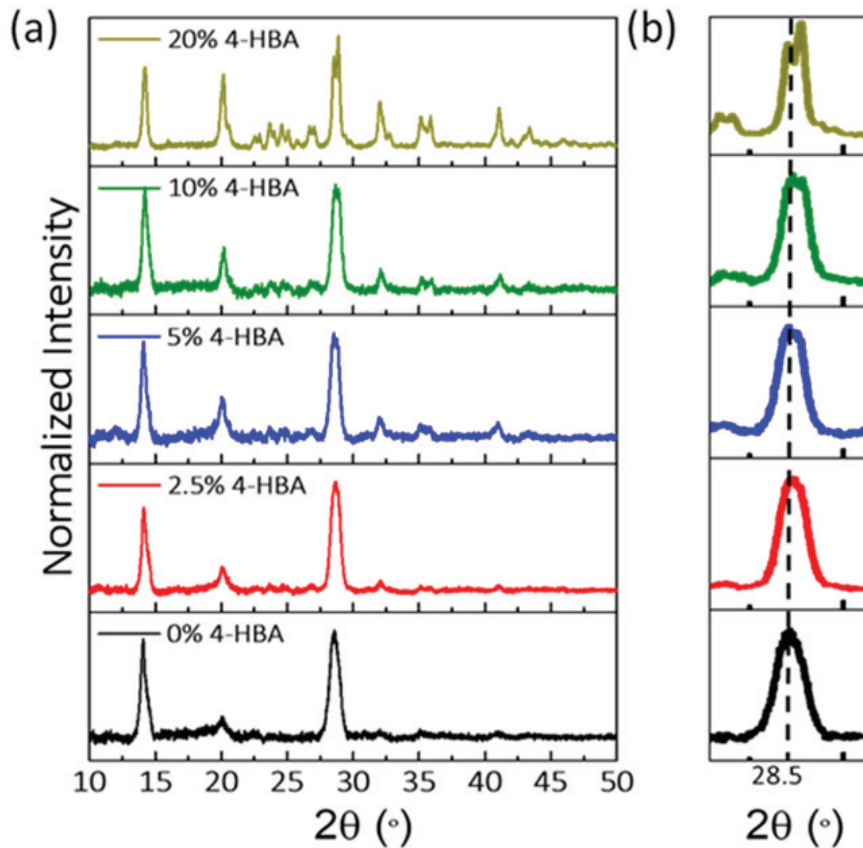


Figure 5.3. a) XRD patterns and b) relative shift in the peak at 28.5° of perovskite NC samples.

5.3.2. Optical Analysis

Photoluminescence (PL) and absorption measurements for 4-HBA added perovskite NCs at different concentrations have been performed. Bandgap energies and PL peak positions of CsPbI₃ NCs with varying 4-HBA percentages are given in Figure 5.4a and Figure 5.4b, respectively. A systematic red-shift in PL spectra of CsPbI₃ NC samples depending on the 4-HBA concentration is observed. Tauc plots were used obtained from the absorption data to determine the bandgaps of the CsPbI₃ NCs (Figure 5.4a). Pristine CsPbI₃ NCs exhibit ~1.75 eV whereas 20% 4-HBA added CsPbI₃ NCs

show ~ 1.73 eV bandgap. Since all CsPbI₃ NCs lie within a similar quantum confinement regime, increased strain in the crystal lattice can be the reason for the change in the bandgap energy as it was observed for perovskite thin films¹⁸⁴. Urbach energies by using the absorption spectra of CsPbI₃ NC samples with varying 4-HBA percentages were calculated (Figure 5.4c). The Urbach energy value decreases dramatically when 4-HBA is introduced to the CsPbI₃ NC synthesis and remains rather similar amongst 4-HBA added samples (Figure S5.2 and Table S5.1). It decreases to 43.65 meV from 47.32 meV when 5% 4-HBA added to CsPbI₃ NCs. Further 4-HBA additions increase the Urbach Energy slightly. However, the Urbach Energy values of 4-HBA added CsPbI₃ NCs are still lower than that of pristine CsPbI₃ NCs. Therefore, Urbach energy calculation shows the disordering is reduced upon 4-HBA addition.

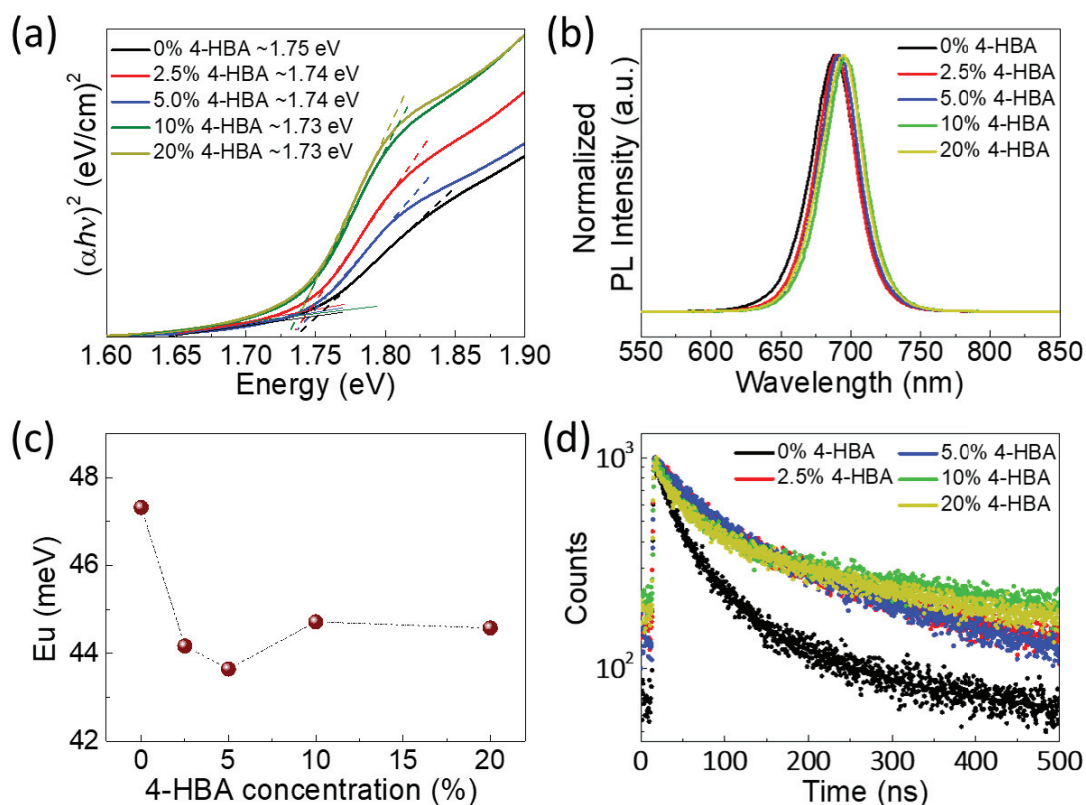


Figure 5.4. a) Tauc plots, b) PL spectra, c) Urbach energy comparison, and d) TRPL data of CsPbI₃ NCs with various 4-HBA amounts.

Time-resolved photoluminescence (TRPL) measurements on the samples have been also conducted to see the 4-HBA addition effect on the charge carrier dynamics of CsPbI₃ NCs (Figure 5.4d). Double exponential fit was used to get τ_1 and τ_2 values which

are given in Table S5.2. TRPL results reveal that the PL lifetime of CsPbI₃ NCs increases from 97.08 ns to 203.71 ns with a 5% 4-HBA addition. After the 5%, the PL lifetime values decrease with further 4-HBA addition and reach 177.45 ns for 20% 4-HBA. Even though the PL lifetime value of 20% HBA is lower than that of 5% 4-HBA value, it is still higher than the PL lifetime of the pristine sample. This means 4-HBA addition and octahedral tilting are causing the suppression of non-radiative recombination caused by defects.

It is widely known that ambient conditions such as humidity facilitate the phase transition of the black CsPbI₃ phase to the yellow CsPbI₃ phase. Polar solvents such as ethanol are also known to cause lattice distortion and lead to the phase transition of CsPbI₃¹⁷⁴. Causing reduced cubic symmetry or octahedral tilting in CsPbI₃ lattice is a well-established method to counter the phase stability issue of the black CsPbI₃ phase^{173,185}. The increased strain and octahedral tilting caused by 4-HBA addition are therefore expected to increase the stability of CsPbI₃ NCs against ambient and polar solvent conditions. In addition, the hydrophobic group in 4-HBA is expected to protect the CsPbI₃ NCs from the ambient humidity and hinder its effect on the phase transformation from black CsPbI₃ to yellow CsPbI₃¹⁸². Therefore, the effect of 4-HBA addition to the stability of CsPbI₃ NCs using ethanol as a polar solvent was tested. The photographic images are shown in Figure 5.5 and Figure S5.3. To this end, 100 μ L ethanol to the expectedly 0.0248 mmol CsPbI₃ NC dispersion in toluene was added and the optical measurements of the samples were carried out.

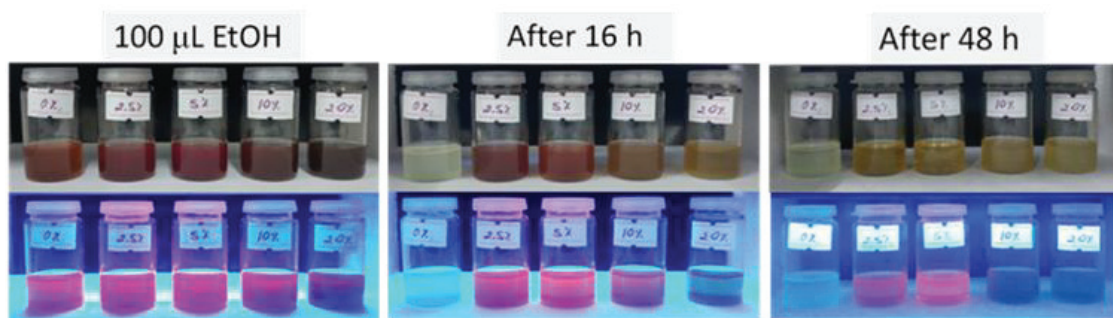


Figure 5.5. Images of CsPbI₃ NCs with varying 4-HBA concentrations after ethanol exposure under daylight and UV light. The vials are ordered with the concentration of 4-HBA at 0%, 2.5%, 5%, 10%, and 20%, respectively from left to right.

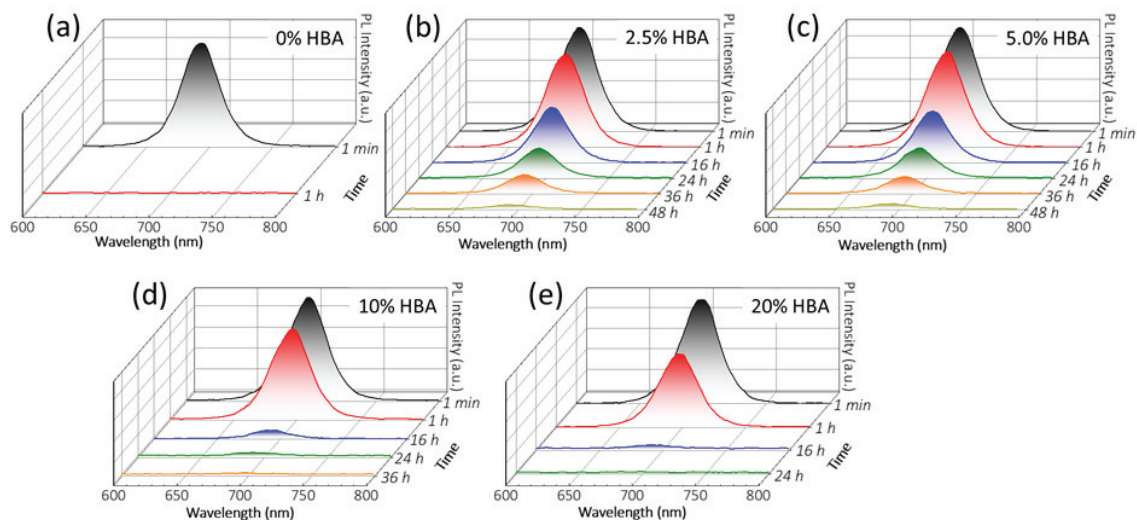


Figure 5.6. PL spectra of CsPbI₃ NCs with various 4-HBA amounts after ethanol exposure depending on time.

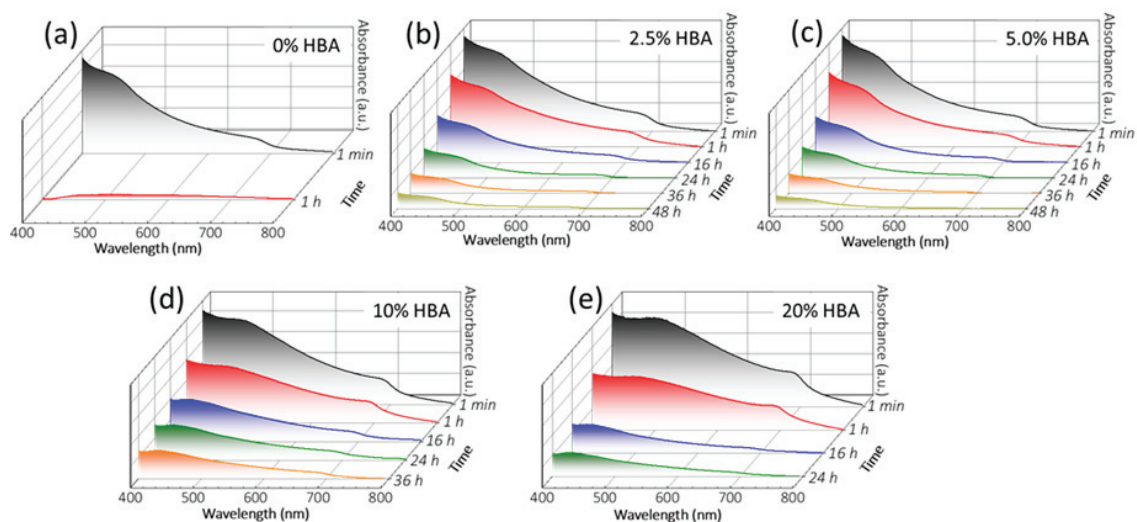


Figure 5.7. Absorption spectra of CsPbI₃ NCs with various 4-HBA amounts depending on ambient air exposure time.

Figure 5.6 shows the periodic PL measurements of CsPbI₃ NCs with different 4-HBA amounts after injection of 100 μ L. The PL degradation over time indicates the phase transition from black perovskite to yellow perovskite phase. The pristine CsPbI₃ NCs transform into the yellow phase in 1 h. When 16 h passed after the ethanol addition, CsPbI₃ NCs with 2.5% and 5% 4-HBA maintained about 50% of their original PL intensities although CsPbI₃ NCs with 10% and 20% 4-HBA lost most of their PL. After

24h in ethanol addition, CsPbI₃ NCs with 2.5% and 5% 4-HBA possessed about 25% of their original PL intensities, and 10% 4-HBA added sample had almost 3% of its initial PL intensity (Figure S5.3 and Figure 5.6). The most stable samples were observed to be 2.5% and 5.0% 4-HBA added CsPbI₃ NCs with minor differences and they still have emission 48 h after EtOH exposure. The absorption behavior of the CsPbI₃ NCs in the same condition showed a similar trend where 4-HBA addition increased the stability (Figure 5.7).

5.4. Conclusion

It has been discovered that 4-HBA ligand additive to CsPbI₃ NCs leads to superior optoelectronic properties and phase stability under ambient conditions. XRD measurements revealed that the compressive strain applied to the CsPbI₃ lattice was proportional to the 4-HBA amount. The changes in the XRD patterns are caused by the partial phase transition of CsPbI₃ NCs to the mixed α - and γ -phases of the perovskite. This increased strain also caused a lower bandgap and higher free charge carrier lifetime. Also, our periodic PL/absorption measurements on the CsPbI₃ samples which were mixed with ethanol show that the strain and hydrophobic effects caused by 4-HBA addition increase the black phase stability of CsPbI₃ NCs to 48 hours where pristine CsPbI₃ NCs lost their black phase in 1 hour. In addition, the optimum octahedral tilting caused by 4-HBA addition of 5.0% was found. This method is a good strategy to improve the stability of perovskites for optoelectronic applications.

CHAPTER 6

CONCLUSION

The main objective of this dissertation was to improve the structural and photophysical properties of perovskite films and perovskite nanocrystals for optoelectronic applications.

In Chapter 2, improvements on the photophysical properties of Pb/Sn-based perovskite films induced by SrI₂ additives were presented. The effects of SrI₂ addition on the defects of the perovskite films were investigated by using microstrain calculations. The doping and segregation regimes were discriminated based on XRD analysis. From Urbach energy calculations, segregated SrI₂ was shown to passivate the perovskite films. XPS analysis showed a reduced ratio of Sn⁴⁺/Sn²⁺ by the addition of SrI₂. Therefore, SrI₂ addition also reduced the oxidation of Sn²⁺ to Sn⁴⁺, improving the stability of the perovskite film. Thus, SrI₂ additive can be an effective method to hinder the Sn²⁺ oxidation in the Sn-based perovskite films.

In chapter 3, improved methylammonium-free perovskite films and solar cells by SrI₂ and CaI₂ additives were demonstrated. Microstrain calculations pointed out to a reduced defect density within the perovskite lattice upon SrI₂ and CaI₂ addition. The solar cells built from pristine, Sr²⁺ added, and Ca²⁺ added perovskite films showed that SrI₂ and CaI₂ additives improve the PCE while SrI₂ added films yielded the best performing device. The average PCE of CsFAPbI₃ PSCs was increased from 11.20% to 13.29% with the addition of Sr²⁺ and 12.82% with the addition of Ca²⁺. Furthermore, average hysteresis index of CsFAPbI₃ PSCs decreased from 14.4% to around 5% by Sr²⁺ and Ca²⁺ additives. Sr²⁺ and Ca²⁺ additives proved to be efficient passivators at low concentration.

In chapter 4, the effects of Sr²⁺ incorporation into the CsPbBr₃ nanocrystals regarding their photophysical properties such as PLQY and PL lifetime were presented. By using XRD patterns and microstrain calculations, the changes in perovskite lattice parameters and the correlation of the defect density trend with the additive concentration were respectively tracked. These results showed that Sr²⁺ doping reduced the defect density and improved optical properties of CsPbBr₃ nanocrystals with a longer lifetime and a higher PLQY. Based on these results, Sr²⁺ doping was performed to improve the

optical properties of $\text{Mn}^{2+}:\text{CsPb}(\text{Br},\text{Cl})_3$ perovskite nanocrystals. The PLQY of CsPbBr_3 NCs was increased from 84.7% to 92.6% by Sr^{2+} doping. Similarly, Sr^{2+} incorporation changed the lattice parameters and decreased the defect density of the perovskite NCs. These changes led to higher PLQY for both perovskite exciton and Mn-state emission doubling the orange/red emission from the Mn-state. The PLQY of Mn-state was improved from 7.6% to 14.2% with Sr^{2+} doping. By using improved perovskite nanocrystals, WLEDs were built to improve the white light luminous efficiency.

In chapter 5, a novel ligand engineering method was employed in order to increase the stability of CsPbI_3 nanocrystals with 4-hydroxybenzoic acid addition to the precursor solution. 4-hydroxybenzoic acid led to an increase in PL lifetime until a specific ratio. XRD patterns showed that 4-hydroxybenzoic acid addition causes a compressive strain in the perovskite lattice which eventually causes octahedral tilting and formation of γ - CsPbI_3 orthorhombic perovskite phase in addition to the α - CsPbI_3 phase. Lastly, the absorption and PL spectra measurements on perovskite nanocrystals in an ethanol medium revealed that 4-hydroxybenzoic acid addition significantly improves the black phase stability of CsPbI_3 perovskite nanocrystals.

REFERENCES

- (1) Chakhmouradian, A. R.; Woodward, P. M. Celebrating 175 Years of Perovskite Research: A Tribute to Roger H. Mitchell. *Phys Chem Miner.* **2014**, *41*, 387–391.
- (2) Ahn, C. H.; Rabe, K. M.; Triscone, J. M. Ferroelectricity at the Nanoscale: Local Polarization in Oxide Thin Films and Heterostructures. *Science.* **2004**, *303*, 488–491.
- (3) Li, W.; Wang, Z.; Deschler, F.; Gao, S.; Friend, R. H.; Cheetham, A. K. Chemically Diverse and Multifunctional Hybrid Organic-Inorganic Perovskites. *Nat. Rev. Mater.* **2017**, *2*, 16099.
- (4) Frost, J. M.; Walsh, A. Molecular Motion and Dynamic Crystal Structures of Hybrid Halide Perovskites. *Org. Halide Perovskite Photovoltaics From Fundam. to Device Archit.* **2016**, 1–17.
- (5) Kaur, P.; Singh, K. Review of Perovskite-Structure Related Cathode Materials for Solid Oxide Fuel Cells. *Ceram. Int.* **2020**, *46*, 5521–5535.
- (6) Fu, Y.; Zhu, H.; Chen, J.; Hautzinger, M. P.; Zhu, X. Y.; Jin, S. Metal Halide Perovskite Nanostructures for Optoelectronic Applications and the Study of Physical Properties. *Nat. Rev. Mater.* **2019**, *4*, 169–188.
- (7) He, X.; Qiu, Y.; Yang, S. Fully-Inorganic Trihalide Perovskite Nanocrystals: A New Research Frontier of Optoelectronic Materials. *Advanced Materials. Adv. Mater.* **2017**, *29*, 1700775.
- (8) Zhao, Y.; Zhu, K. Organic-Inorganic Hybrid Lead Halide Perovskites for Optoelectronic and Electronic Applications. *Chem. Soc. Rev.* **2016**, *45*, 655–689.
- (9) Shamsi, J.; Urban, A. S.; Imran, M.; De Trizio, L.; Manna, L. Metal Halide Perovskite Nanocrystals: Synthesis, Post-Synthesis Modifications, and Their Optical Properties. *Chem. Rev.* **2019**, *119*, 3296–3348.
- (10) Zhou, Y.; Zhao, Y. Chemical Stability and Instability of Inorganic Halide Perovskites. *Energy Environ. Sci.* **2019**, *12*, 1495–1511.
- (11) Manser, J. S.; Christians, J. A.; Kamat, P. V. Intriguing Optoelectronic Properties

- of Metal Halide Perovskites. *Chem. Rev.* **2016**, *116*, 12956–13008.
- (12) Zhou, Y.; Zhao, Y. Chemical Stability and Instability of Inorganic Halide Perovskites. *Energy Environ. Sci.* **2019**, *12*, 1495–1511.
- (13) Jin, S. Can We Find the Perfect A-Cations for Halide Perovskites? *ACS Energy Lett.* **2021**, *6*, 3386–3389.
- (14) Fu, Y.; Rea, M. T.; Chen, J.; Morrow, D. J.; Hautzinger, M. P.; Zhao, Y.; Pan, D.; Manger, L. H.; Wright, J. C.; Goldsmith, R. H. Selective Stabilization and Photophysical Properties of Metastable Perovskite Polymorphs of CsPbI₃ in Thin Films. *Chem. Mater.* **2017**, *29*, 8385-8394.
- (15) Masi, S.; Gualdrón-Reyes, A. F.; Mora-Seró, I. Stabilization of Black Perovskite Phase in FAPbI₃ and CsPbI₃. *ACS Energy Lett.* **2020**, *5*, 1974–1985.
- (16) Li, Z.; Yang, M.; Park, J. S.; Wei, S. H.; Berry, J. J.; Zhu, K. Stabilizing Perovskite Structures by Tuning Tolerance Factor: Formation of Formamidinium and Cesium Lead Iodide Solid-State Alloys. *Chem. Mater.* **2016**, *28*, 284–292.
- (17) Li, Z.; Yang, M.; Park, J. S.; Wei, S. H.; Berry, J. J.; Zhu, K. Stabilizing Perovskite Structures by Tuning Tolerance Factor: Formation of Formamidinium and Cesium Lead Iodide Solid-State Alloys. *Chem. Mater.* **2016**, *28*, 284–292.
- (18) Turren-Cruz, S. H.; Hagfeldt, A.; Saliba, M. Methylammonium-Free, High-Performance, and Stable Perovskite Solar Cells on a Planar Architecture. *Science.* **2018**, *362*, 449–453.
- (19) Saliba, M.; Matsui, T.; Seo, J.-Y.; Domanski, K.; Correa-Baena, J.-P.; Khaja, M.; Zakeeruddin, S. M.; Tress, W.; Abate, A.; Hagfeldt, A.; Grätzel, M. Cesium-Containing Triple Cation Perovskite Solar Cells: Improved Stability, Reproducibility and High Efficiency. *Energy Environ. Sci.* **2016**, *9*, 1989-1997.
- (20) Correa-Baena, J.-P.; Saliba, M.; Buonassisi, T.; Grätzel, M.; Abate, A.; Tress, W.; Hagfeldt, A. Promises and Challenges of Perovskite Solar Cells. *Science.* **2017**, *358*, 739–744.
- (21) Brenner, T. M.; Egger, D. A.; Kronik, L.; Hodes, G.; Cahen, D. Hybrid Organic - Inorganic Perovskites: Low-Cost Semiconductors with Intriguing Charge-Transport Properties. *Nat. Rev. Mater.* **2016**, *1*, 1–16.

- (22) Wehrenfennig, C.; Eperon, G. E.; Johnston, M. B.; Snaith, H. J.; Herz, L. M. High Charge Carrier Mobilities and Lifetimes in Organolead Trihalide Perovskites. *Adv. Mater.* **2014**, *26*, 1584–1589.
- (23) Miyata, A.; Mitioglu, A.; Plochocka, P.; Portugall, O.; Wang, J. T. W.; Stranks, S. D.; Snaith, H. J.; Nicholas, R. J. Direct Measurement of the Exciton Binding Energy and Effective Masses for Charge Carriers in Organic-Inorganic Tri-Halide Perovskites. *Nat. Phys.* **2015**, *11*, 582–587.
- (24) Yang, Z.; Rajagopal, A.; Jen, A. K. Y. Ideal Bandgap Organic–Inorganic Hybrid Perovskite Solar Cells. *Adv. Mater.* **2017**, *29*, 1704418.
- (25) Sahli, F.; Werner, J.; Kamino, B. A.; Bräuninger, M.; Monnard, R.; Paviet-Salomon, B.; Barraud, L.; Ding, L.; Diaz Leon, J. J.; Sacchetto, D.; Cattaneo, G.; Despeisse, M.; Boccard, M.; Nicolay, S.; Jeangros, Q.; Niesen, B.; Ballif, C. Fully Textured Monolithic Perovskite/Silicon Tandem Solar Cells with 25.2% Power Conversion Efficiency. *Nat. Mater.* **2018**, *17*, 820–826.
- (26) Hou, Y.; Aydin, E.; De Bastiani, M.; Xiao, C.; Isikgor, F. H.; Xue, D. J.; Chen, B.; Chen, H.; Bahrami, B.; Chowdhury, A. H.; Johnston, A.; Baek, S. W.; Huang, Z.; Wei, M.; Dong, Y.; Troughton, J.; Jalmood, R.; Mirabelli, A. J.; Allen, T. G.; Van Kerschaver, E.; Saidaminov, M. I.; Baran, D.; Qiao, Q.; Zhu, K.; De Wolf, S.; Sargent, E. H. Efficient Tandem Solar Cells with Solution-Processed Perovskite on Textured Crystalline Silicon. *Science*. **2020**, *367*, 1135–1140.
- (27) Tong, J.; Song, Z.; Kim, D. H.; Chen, X.; Chen, C.; Palmstrom, A. F.; Ndione, P. F.; Reese, M. O.; Dunfield, S. P.; Reid, O. G.; Liu, J.; Zhang, F.; Harvey, S. P.; Li, Z.; Christensen, S. T.; Teeter, G.; Zhao, D.; Al-Jassim, M. M.; Van Hest, M. F. A. M.; Beard, M. C.; Shaheen, S. E.; Berry, J. J.; Yan, Y.; Zhu, K. Carrier Lifetimes of >1 Ms in Sn-Pb Perovskites Enable Efficient All-Perovskite Tandem Solar Cells. *Science*. **2019**, *364*, 475–479.
- (28) Protesescu, L.; Yakunin, S.; Bodnarchuk, M. I.; Krieg, F.; Caputo, R.; Hendon, C. H.; Yang, R. X.; Walsh, A.; Kovalenko, M. V. Nanocrystals of Cesium Lead Halide Perovskites (CsPbX₃, X = Cl, Br, and I): Novel Optoelectronic Materials Showing Bright Emission with Wide Color Gamut. *Nano Lett.* **2015**, *15*, 18.
- (29) Huang, H.; Bodnarchuk, M. I.; Kershaw, S. V.; Kovalenko, M. V.; Rogach, A. L.

- Lead Halide Perovskite Nanocrystals in the Research Spotlight: Stability and Defect Tolerance. *ACS Energy Lett.* **2017**, *2*, 2071–2083.
- (30) Meinardi, F.; Akkerman, Q. A.; Bruni, F.; Park, S.; Mauri, M.; Dang, Z.; Manna, L.; Brovelli, S. Doped Halide Perovskite Nanocrystals for Reabsorption-Free Luminescent Solar Concentrators. *ACS Energy Lett.* **2017**, *2*, 2368–2377.
- (31) Pan, J.; Shang, Y.; Yin, J.; De Bastiani, M.; Peng, W.; Dursun, I.; Sinatra, L.; El-Zohry, A. M.; Hedhili, M. N.; Emwas, A. H.; Mohammed, O. F.; Ning, Z.; Bakr, O. M. Bidentate Ligand-Passivated CsPbI₃ Perovskite Nanocrystals for Stable Near-Unity Photoluminescence Quantum Yield and Efficient Red Light-Emitting Diodes. *J. Am. Chem. Soc.* **2018**, *140*, 562–565.
- (32) Sanehira, E. M.; Marshall, A. R.; Christians, J. A.; Harvey, S. P.; Ciesielski, P. N.; Wheeler, L. M.; Schulz, P.; Lin, L. Y.; Beard, M. C.; Luther, J. M. Enhanced Mobility CsPbI₃ Quantum Dot Arrays for Record-Efficiency, High-Voltage Photovoltaic Cells. *Sci. Adv.* **2017**, *3*, 1-8.
- (33) Dutta, A.; Pradhan, N. Phase-Stable Red-Emitting CsPbI₃ Nanocrystals: Successes and Challenges. *ACS Energy Lett.* **2019**, *4*, 709-719.
- (34) Akkerman, Q. A.; Rainò, G.; Kovalenko, M. V.; Manna, L. Genesis, Challenges and Opportunities for Colloidal Lead Halide Perovskite Nanocrystals. *Nat. Mater.* **2018**, *17*, 394–405.
- (35) Brandt, R. E.; Poindexter, J. R.; Gorai, P.; Kurchin, R. C.; Hoye, R. L. Z.; Nienhaus, L.; Wilson, M. W. B.; Polizzotti, J. A.; Sereika, R.; Žaltauskas, R.; Lee, L. C.; Macmanus-Driscoll, J. L.; Bawendi, M.; Stevanović, V.; Buonassisi, T. Searching for “Defect-Tolerant” Photovoltaic Materials: Combined Theoretical and Experimental Screening. *Chem. Mater.* **2017**, *29*, 4667–4674.
- (36) Lignos, I.; Protesescu, L.; Emiroglu, D. B.; MacEiczyk, R.; Schneider, S.; Kovalenko, M. V.; DeMello, A. J. Unveiling the Shape Evolution and Halide-Ion-Segregation in Blue-Emitting Formamidinium Lead Halide Perovskite Nanocrystals Using an Automated Microfluidic Platform. *Nano Lett.* **2018**, *18*, 1246–1252.
- (37) Jagielski, J.; Kumar, S.; Wang, M.; Scullion, D.; Lawrence, R.; Li, Y. T.; Yakunin, S.; Tian, T.; Kovalenko, M. V.; Chiu, Y. C.; Santos, E. J. G.; Lin, S.; Shih, C. J.

Aggregation-Induced Emission in Lamellar Solids of Colloidal Perovskite Quantum Wells. *Sci. Adv.* **2017**, *3*, 1-10.

- (38) Protesescu, L.; Yakunin, S.; Bodnarchuk, M. I.; Krieg, F.; Caputo, R.; Hendon, C. H.; Yang, R. X.; Walsh, A.; Kovalenko, M. V. Nanocrystals of Cesium Lead Halide Perovskites (CsPbX₃, X = Cl, Br, and I): Novel Optoelectronic Materials Showing Bright Emission with Wide Color Gamut. *Nano Lett.* **2015**, *15*, 3692–3696.
- (39) Akkerman, Q. A.; Motti, S. G.; Srimath Kandada, A. R.; Mosconi, E.; D’Innocenzo, V.; Bertoni, G.; Marras, S.; Kamino, B. A.; Miranda, L.; De Angelis, F.; Petrozza, A.; Prato, M.; Manna, L. Solution Synthesis Approach to Colloidal Cesium Lead Halide Perovskite Nanoplatelets with Monolayer-Level Thickness Control. *J. Am. Chem. Soc.* **2016**, *138*, 1010–1016.
- (40) Weidman, M. C.; Seitz, M.; Stranks, S. D.; Tisdale, W. A. Highly Tunable Colloidal Perovskite Nanoplatelets through Variable Cation, Metal, and Halide Composition. *ACS Nano.* **2016**, *10*, 7830–7839.
- (41) Weidman, M. C.; Goodman, A. J.; Tisdale, W. A. Colloidal Halide Perovskite Nanoplatelets: An Exciting New Class of Semiconductor Nanomaterials. *Chem.Mater.* **2017**, *29*, 5019–5030.
- (42) Marinova, N.; Valero, S.; Delgado, J. L. Organic and Perovskite Solar Cells: Working Principles, Materials and Interfaces. *J. Colloid Interface Sci.* **2017**, *488*, 373–389.
- (43) Guillemoles, J. F.; Kirchartz, T.; Cahen, D.; Rau, U. Guide for the Perplexed to the Shockley–Queisser Model for Solar Cells. *Nat. Photonics* **2019**, *13*, 501–505.
- (44) Rühle, S. Tabulated Values of the Shockley–Queisser Limit for Single Junction Solar Cells. *Sol. Energy* **2016**, *130*, 139–147.
- (45) Bayod-Rújula, A. A. Solar Photovoltaics (PV). *Sol. Hydrog. Prod. Process. Syst. Technol.* **2019**, 237–295.
- (46) Hou, Y. Rational Interfaces Design of Efficient Organic–Inorganic Hybrid Perovskite Solar Cells. **2017**.
- (47) Palazon, F.; Di Stasio, F.; Akkerman, Q. A.; Krahne, R.; Prato, M.; Manna, L.

Polymer-Free Films of Inorganic Halide Perovskite Nanocrystals as UV-to-White Color-Conversion Layers in LEDs. *Chem. Mater.* **2016**, *28*, 2902–2906.

- (48) Li, X.; Wu, Y.; Zhang, S.; Cai, B.; Gu, Y.; Song, J.; Zeng, H. CsPbX₃ Quantum Dots for Lighting and Displays: Room-temperature Synthesis, Photoluminescence Superiorities, Underlying Origins and White Light-Emitting Diodes. *Adv. Funct. Mater.* **2016**, *26*, 2435–2445.
- (49) Chen, J.; Xiang, H.; Wang, J.; Wang, R.; Li, Y.; Shan, Q.; Xu, X.; Dong, Y.; Wei, C.; Zeng, H. Perovskite White Light Emitting Diodes: Progress, Challenges, and Opportunities. *ACS Nano* **2021**, *15*, 17150–17174.
- (50) Zhang, Y. W.; Wu, G.; Dang, H.; Ma, K.; Chen, S. Multicolored Mixed-Organic-Cation Perovskite Quantum Dots (FA_xMA_{1-x}PbX₃, X = Br and I) for White Light-Emitting Diodes. *Ind. Eng. Chem. Res.* **2017**, *56*, 10053–10059.
- (51) Wu, H.; Wang, S.; Cao, F.; Zhou, J.; Wu, Q.; Wang, H.; Li, X.; Yin, L.; Yang, X. Ultrastable Inorganic Perovskite Nanocrystals Coated with a Thick Long-Chain Polymer for Efficient White Light-Emitting Diodes. *Chem. Mater.* **2019**, *31*, 1936–1940.
- (52) Lu, M.; Zhang, X.; Zhang, Y.; Guo, J.; Shen, X.; Yu, W. W.; Rogach, A. L. Simultaneous Strontium Doping and Chlorine Surface Passivation Improve Luminescence Intensity and Stability of CsPbI₃ Nanocrystals Enabling Efficient Light-Emitting Devices. *Adv. Mater.* **2018**, *30*, 1–6.
- (53) Chen, C.; Xuan, T.; Bai, W.; Zhou, T.; Huang, F.; Xie, A.; Wang, L.; Xie, R. J. Highly Stable CsPbI₃:Sr²⁺ Nanocrystals with near-Unity Quantum Yield Enabling Perovskite Light-Emitting Diodes with an External Quantum Efficiency of 17.1%. *Nano Energy* **2021**, *85*, 106033.
- (54) Chang, C. Y.; Solodukhin, A. N.; Liao, S. Y.; Mahesh, K. P. O.; Hsu, C. L.; Ponomarenko, S. A.; Luponosov, Y. N.; Chao, Y. C. Perovskite White Light-Emitting Diodes Based on a Molecular Blend Perovskite Emissive Layer. *J. Mater. Chem. C* **2019**, *7*, 8634–8642.
- (55) Chen, J.; Xiang, H.; Wang, J.; Wang, R.; Li, Y.; Shan, Q.; Xu, X.; Dong, Y.; Wei, C.; Zeng, H. Perovskite White Light Emitting Diodes: Progress, Challenges, and Opportunities. *ACS Nano* **2021**, *15*, 17150–17174.

- (56) Best Research-Cell Efficiency Chart | Photovoltaic Research | NREL
<https://www.nrel.gov/pv/cell-efficiency.html> (accessed June 10, 2022).
- (57) Koh, T. M.; Krishnamoorthy, T.; Yantara, N.; Shi, C.; Leong, W. L.; Boix, P. P.; Grimsdale, A. C.; Mhaisalkar, S. G.; Mathews, N. Formamidinium Tin-Based Perovskite with Low E_g for Photovoltaic Applications. *J. Mater. Chem. A* **2015**, *3*, 14996–15000.
- (58) Krishnamoorthy, T.; Ding, H.; Yan, C.; Leong, W. L.; Baikie, T.; Zhang, Z.; Sherburne, M.; Li, S.; Asta, M.; Mathews, N.; Mhaisalkar, S. G. Lead-Free Germanium Iodide Perovskite Materials for Photovoltaic Applications. *J. Mater. Chem. A* **2015**, *3*, 23829–23832.
- (59) Chen, M.; Ju, M. G.; Garces, H. F.; Carl, A. D.; Ono, L. K.; Hawash, Z.; Zhang, Y.; Shen, T.; Qi, Y.; Grimm, R. L.; Pacifici, D.; Zeng, X. C.; Zhou, Y.; Padture, N. P. Highly Stable and Efficient All-Inorganic Lead-Free Perovskite Solar Cells with Native-Oxide Passivation. *Nat. Commun.* **2019**, *10*, 16.
- (60) Zong, Y.; Zhou, Z.; Chen, M.; Padture, N. P.; Zhou, Y. Lewis-Adduct Mediated Grain-Boundary Functionalization for Efficient Ideal-Bandgap Perovskite Solar Cells with Superior Stability. *Adv. Energy Mater.* **2018**, *8*, 1800997.
- (61) Li, M.; Wang, Z. K.; Zhuo, M. P.; Hu, Y.; Hu, K. H.; Ye, Q. Q.; Jain, S. M.; Yang, Y. G.; Gao, X. Y.; Liao, L. S. Pb–Sn–Cu Ternary Organometallic Halide Perovskite Solar Cells. *Adv. Mater.* **2018**, *30*, 1800258.
- (62) Guner, T.; Demir, M. M. A Review on Halide Perovskites as Color Conversion Layers in White Light Emitting Diode Applications. *Phys. Status Solidi Appl. Mater. Sci.* **2018**, *215*, 1–11.
- (63) McMeekin, D. P.; Sadoughi, G.; Rehman, W.; Eperon, G. E.; Saliba, M.; Hörantner, M. T.; Haghighirad, A.; Sakai, N.; Korte, L.; Rech, B.; Johnston, M. B.; Herz, L. M.; Snaith, H. J. A Mixed-Cation Lead Mixed-Halide Perovskite Absorber for Tandem Solar Cells. *Science* **2016**, *351*, 151–155.
- (64) Shockley, W.; Queisser, H. J. Detailed Balance Limit of Efficiency of P-n Junction Solar Cells. *J. Appl. Phys.* **1961**, *32*, 510–519.
- (65) Ogomi, Y.; Morita, A.; Tsukamoto, S.; Saitho, T.; Fujikawa, N.; Shen, Q.; Toyoda,

- T.; Yoshino, K.; Pandey, S. S.; Ma, T.; Hayase, S. $\text{CH}_3\text{NH}_3\text{Sn}_x\text{Pb}_{(1-x)}\text{I}_3$ Perovskite Solar Cells Covering up to 1060 Nm. *J. Phys. Chem. Lett.* **2014**, *5*, 1004–1011.
- (66) Noel, N. K.; Stranks, S. D.; Abate, A.; Wehrenfennig, C.; Guarnera, S.; Haghighirad, A. A.; Sadhanala, A.; Eperon, G. E.; Pathak, S. K.; Johnston, M. B.; Petrozza, A.; Herz, L. M.; Snaith, H. J. Lead-Free Organic-Inorganic Tin Halide Perovskites for Photovoltaic Applications. *Energy Environ. Sci.* **2014**, *7*, 3061–3068.
- (67) Gupta, S.; Cahen, D.; Hodes, G. How SnF_2 Impacts the Material Properties of Lead-Free Tin Perovskites. *J. Phys. Chem. C* **2018**, *122*, 13926–13936.
- (68) Leijtens, T.; Prasanna, R.; Gold-Parker, A.; Toney, M. F.; McGehee, M. D. Mechanism of Tin Oxidation and Stabilization by Lead Substitution in Tin Halide Perovskites. *ACS Energy Lett.* **2017**, *2*, 2159–2165.
- (69) Chatterjee, S.; Pal, A. J. Influence of Metal Substitution on Hybrid Halide Perovskites: Towards Lead-Free Perovskite Solar Cells. *J. Mater. Chem. A* **2018**, *6*, 3793–3823.
- (70) Adjokatse, S.; Kahmann, S.; Duim, H.; Loi, M. A. Effects of Strontium Doping on the Morphological, Structural, and Photophysical Properties of FASnI_3 Perovskite Thin Films. *APL Mater.* **2019**, *7*, 031116.
- (71) Ran, C.; Xi, J.; Gao, W.; Yuan, F.; Lei, T.; Jiao, B.; Hou, X.; Wu, Z. Bilateral Interface Engineering toward Efficient 2D-3D Bulk Heterojunction Tin Halide Lead-Free Perovskite Solar Cells. *ACS Energy Lett.* **2018**, *3*, 713–721.
- (72) Leijtens, T.; Eperon, G. E.; Noel, N. K.; Habisreutinger, S. N.; Petrozza, A.; Snaith, H. J. Stability of Metal Halide Perovskite Solar Cells. *Adv. Energy Mater.* **2015**, *5*, 1500963.
- (73) Gu, F.; Ye, S.; Zhao, Z.; Rao, H.; Liu, Z.; Bian, Z.; Huang, C. Improving Performance of Lead-Free Formamidinium Tin Triiodide Perovskite Solar Cells by Tin Source Purification. *Sol. RRL* **2018**, *2*, 1800136.
- (74) Gupta, S.; Cahen, D.; Hodes, G. How SnF_2 Impacts the Material Properties of Lead-Free Tin Perovskites. *J. Phys. Chem. C* **2018**, *122*, 13926–13936.
- (75) Ripolles, T. S.; Yamasuso, D.; Zhang, Y.; Kamarudin, M. A.; Ding, C.; Hirotoni,

- D.; Shen, Q.; Hayase, S. New Tin(II) Fluoride Derivative as a Precursor for Enhancing the Efficiency of Inverted Planar Tin/Lead Perovskite Solar Cells. **2018**, *122*, 27284–27291.
- (76) Liao, W.; Zhao, D.; Yu, Y.; Grice, C. R.; Wang, C.; Cimaroli, A. J.; Schulz, P.; Meng, W.; Zhu, K.; Xiong, R. G.; Yan, Y. Lead-Free Inverted Planar Formamidinium Tin Triiodide Perovskite Solar Cells Achieving Power Conversion Efficiencies up to 6.22%. *Adv. Mater.* **2016**, *28*, 9333–9340.
- (77) Lee, S. J.; Shin, S. S.; Kim, Y. C.; Kim, D.; Ahn, T. K.; Noh, J. H.; Seo, J.; Seok, S. Il. Fabrication of Efficient Formamidinium Tin Iodide Perovskite Solar Cells through SnF₂–Pyrazine Complex. *J. Am. Chem. Soc.* **2016**, *138*, 3974–3977.
- (78) Kumar, M. H.; Dharani, S.; Leong, W. L.; Boix, P. P.; Prabhakar, R. R.; Baikie, T.; Shi, C.; Ding, H.; Ramesh, R.; Asta, M.; Graetzel, M.; Mhaisalkar, S. G.; Mathews, N. Lead-Free Halide Perovskite Solar Cells with High Photocurrents Realized through Vacancy Modulation. *Adv. Mater.* **2014**, *26*, 7122–7127.
- (79) Yuce, H.; Perini, C. A. R.; Hidalgo, J.; Castro-Méndez, A. F.; Evans, C.; Betancur, P. F.; Vagott, J. N.; An, Y.; Bairley, K.; Demir, M. M.; Correa-Baena, J. P. Understanding the Impact of SrI₂ Additive on the Properties of Sn-Based Halide Perovskites. *Opt. Mater.* **2021**, *123*, 1–7.
- (80) Qiu, W.; Merckx, T.; Jaysankar, M.; Masse De La Huerta, C.; Rakocevic, L.; Zhang, W.; Paetzold, U. W.; Gehlhaar, R.; Froyen, L.; Poortmans, J.; Cheyns, D.; Snaith, H. J.; Heremans, P. Pinhole-Free Perovskite Films for Efficient Solar Modules. *Energy Environ. Sci.* **2016**, *9*, 484–489.
- (81) Chan, S. H.; Wu, M. C.; Lee, K. M.; Chen, W. C.; Lin, T. H.; Su, W. F. Enhancing Perovskite Solar Cell Performance and Stability by Doping Barium in Methylammonium Lead Halide. *J. Mater. Chem. A* **2017**, *5*, 18044–18052.
- (82) Hu, Y.; Aygüler, M. F.; Petrus, M. L.; Bein, T.; Docampo, P. Impact of Rubidium and Cesium Cations on the Moisture Stability of Multiple-Cation Mixed-Halide Perovskites. *ACS Energy Lett.* **2017**, *2*, 2212–2218.
- (83) Yao, E. P.; Sun, P.; Huang, W.; Yao, E. P.; Yang, Y.; Wang, M. Efficient Planar Perovskite Solar Cells Using Halide Sr-Substituted Pb Perovskite. *Nano Energy* **2017**, *36*, 213–222.

- (84) Phung, N.; Félix, R.; Meggiolaro, D.; Al-Ashouri, A.; Sousa e Silva, G.; Hartmann, C.; Hidalgo, J.; Köbler, H.; Mosconi, E.; Lai, B. The Doping Mechanism of Halide Perovskite Unveiled by Alkaline Earth Metals. *J. Am. Chem. Soc.* **2020**, *142*, 2364–2374.
- (85) Hasan, S. A. U.; Lee, D. S.; Im, S. H.; Hong, K. H. Present Status and Research Prospects of Tin-Based Perovskite Solar Cells. *Sol. RRL* **2020**, *4*, 1–30.
- (86) Anitha, V. S.; Sujatha Lekshmy, S.; Joy, K. Effect of Mn Doping on the Structural, Magnetic, Optical and Electrical Properties of ZrO₂-SnO₂ Thin Films Prepared by Sol-Gel Method. *J. Alloys Compd.* **2016**, *675*, 331–340.
- (87) Hsiao, K. C.; Jao, M. H.; Li, B. T.; Lin, T. H.; Liao, S. H. C.; Wu, M. C.; Su, W. F. Enhancing Efficiency and Stability of Hot Casting P-i-n Perovskite Solar Cell via Dipolar Ion Passivation. *ACS Appl. Energy Mater.* **2019**, *2*, 4821-4832.
- (88) Rajagopal, A.; Liang, P.-W. W.; Chueh, C.-C. C.; Yang, Z.; Jen, A. K. Y. K.-Y. Defect Passivation via a Graded Fullerene Heterojunction in Low-Bandgap Pb–Sn Binary Perovskite Photovoltaics. *ACS Energy Lett.* **2017**, *2*, 2531–2539.
- (89) Xin, D.; Tie, S.; Yuan, R.; Zheng, X.; Zhu, J.; Zhang, W.-H. H. Defect Passivation in Hybrid Perovskite Solar Cells by Tailoring the Electron Density Distribution in Passivation Molecules. *ACS Appl. Mater. Interfaces* **2019**, *11*, 44233–44240.
- (90) Kodigala, S. R. *Cu(In_{1-x}Ga_x)Se₂ Based Thin Film Solar Cells*; Academic Press, 2011.
- (91) Liu, X.; Wang, Y.; Wu, T.; He, X.; Meng, X.; Barbaud, J.; Chen, H.; Segawa, H.; Yang, X.; Han, L. Efficient and Stable Tin Perovskite Solar Cells Enabled by Amorphous-Polycrystalline Structure. *Nat. Commun.* **2020**, *11*, 2678.
- (92) Zhao, Z.; Gu, F.; Li, Y.; Sun, W.; Ye, S.; Rao, H.; Liu, Z.; Bian, Z.; Huang, C. Mixed-Organic-Cation Tin Iodide for Lead-Free Perovskite Solar Cells with an Efficiency of 8.12%. *Adv. Sci.* **2017**, *4*, 1700204.
- (93) Huang, L.; Zhou, X.; Xue, R.; Xu, P.; Wang, S.; Xu, C.; Zeng, W.; Xiong, Y.; Sang, H.; Liang, D. Low-Temperature Growing Anatase TiO₂/SnO₂ Multi-Dimensional Heterojunctions at MXene Conductive Network for High-Efficient Perovskite Solar Cells. *Nano-Micro Lett.* **2020**, *12*, 44.

- (94) Lau, C. F. J.; Zhang, M.; Deng, X.; Zheng, J.; Bing, J.; Ma, Q.; Kim, J.; Hu, L.; Green, M. A.; Huang, S.; Ho-Baillie, A. Strontium-Doped Low-Temperature-Processed CsPbI₂Br Perovskite Solar Cells. *ACS Energy Lett.* **2017**, *2*, 2319–2325.
- (95) Mollar-Cuni, A.; Ventura-Espinosa, D.; Martín, S.; Mayoral, Á.; Borja, P.; Mata, J. A. Stabilization of Nanoparticles Produced by Hydrogenation of Palladium-N-Heterocyclic Carbene Complexes on the Surface of Graphene and Implications in Catalysis. *ACS Omega* **2018**, *3*, 15217–15228.
- (96) Sezen, H.; Suzer, S. Communication: Enhancement of Dopant Dependent x-Ray Photoelectron Spectroscopy Peak Shifts of Si by Surface Photovoltage. *J. Chem. Phys.* **2011**, *135*, 162110.
- (97) Kim, H.; Lee, J. W.; Han, G. R.; Kim, S. K.; Oh, J. H. Synergistic Effects of Cation and Anion in an Ionic Imidazolium Tetrafluoroborate Additive for Improving the Efficiency and Stability of Half-Mixed Pb-Sn Perovskite Solar Cells. *Adv. Funct. Mater.* **2021**, *31*, 2008801.
- (98) Rocks, C.; Svrcek, V.; Velusamy, T.; Macias-Montero, M.; Maguire, P.; Mariotti, D. Type-I Alignment in MAPbI₃ Based Solar Devices with Doped-Silicon Nanocrystals. *Nano Energy* **2018**, *50*, 245–255.
- (99) Rajendra Kumar, G.; Dennyson Savariraj, A.; Karthick, S. N.; Selvam, S.; Balamuralitharan, B.; Kim, H. J.; Viswanathan, K. K.; Vijaykumar, M.; Prabakar, K. Phase Transition Kinetics and Surface Binding States of Methylammonium Lead Iodide Perovskite. *Phys. Chem. Chem. Phys.* **2016**, *18*, 7284–7292.
- (100) Ahmad, Z.; Najeeb, M. A.; Shakoor, R. A.; Alashraf, A.; Al-, S. A.; Al-Muhtaseb, S. A.; Soliman, A.; Nazeeruddin, M. K. Instability in CH₃NH₃PbI₃ Perovskite Solar Cells Due to Elemental Migration and Chemical Composition Changes. *Sci. Rep.* **2017**, *7*, 1–8.
- (101) Pellet, N.; Gao, P.; Gregori, G.; Yang, T. Y.; Nazeeruddin, M. K.; Maier, J.; Grätzel, M. Mixed-Organic-Cation Perovskite Photovoltaics for Enhanced Solar-Light Harvesting. *Angew. Chem.* **2014**, *126*, 3215–3221.
- (102) Luo, P.; Zhou, S.; Zhou, Y.; Xia, W.; Sun, L.; Cheng, J.; Xu, C.; Lu, Y. Fabrication of Cs_xFA_{1-x}PbI₃ Mixed-Cation Perovskites via Gas-Phase-Assisted Compositional Modulation for Efficient and Stable Photovoltaic Devices. *ACS Appl. Mater.*

Interfaces **2017**, *9*, 42708–42716.

- (103) Frost, J. M.; Butler, K. T.; Brivio, F.; Hendon, C. H.; Van Schilfgaarde, M.; Walsh, A. Atomistic Origins of High-Performance in Hybrid Halide Perovskite Solar Cells. *Nano Lett.* **2014**, *14*, 2584–2590.
- (104) Xu, Z.; Zhao, Y.; Zhang, J.; Chen, K.; Brabec, C. J.; Feng, Y. Phase Diagram and Stability of Mixed-Cation Lead Iodide Perovskites: A Theory and Experiment Combined Study. *Phys. Rev. Mater.* **2020**, *4*, 095401.
- (105) Lyu, M.; Park, N. G. Effect of Additives AX (A = FA, MA, Cs, Rb, NH₄, X = Cl, Br, I) in FAPbI₃ on Photovoltaic Parameters of Perovskite Solar Cells. *Sol. RRL* **2020**, *4*, 2000331.
- (106) Ma, C.; Park, N. G. Paradoxical Approach with a Hydrophilic Passivation Layer for Moisture-Stable, 23% Efficient Perovskite Solar Cells. *ACS Energy Lett.* **2020**, *5*, 3268–3275.
- (107) Snaith, H. J.; Abate, A.; Ball, J. M.; Eperon, G. E.; Leijtens, T.; Noel, N. K.; Stranks, S. D.; Tse, J.; Wang, W.; Wojciechowski, K.; Zhang, W. Anomalous Hysteresis in Perovskite Solar Cells. *J. Phys. Chem. Lett* **2014**, *5*, 1511-1515.
- (108) Son, D.-Y.; Kim, S.-G.; Seo, J.-Y.; Lee, S.-H.; Shin, H.; Lee, D.; Park, N.-G. Universal Approach toward Hysteresis-Free Perovskite Solar Cell via Defect Engineering. *J. Am. Chem. Soc.* **2018**, *140*, 1358–1364
- (109) Li, C.; Guerrero, A.; Zhong, Y.; Huettner, S. Origins and Mechanisms of Hysteresis in Organometal Halide Perovskites. *J. Phy.: Condens. Matter.* **2017**, *29*, 193001.
- (110) Son, D.-Y.; Lee, J.-W.; Ji Choi, Y.; Jang, I.-H.; Lee, S.; Yoo, P. J.; Shin, H.; Ahn, N.; Choi, M.; Kim, D.; Park, N.-G. Self-Formed Grain Boundary Healing Layer for Highly Efficient CH₃NH₃PbI₃ Perovskite Solar Cells. *Nat. Energy* **2016**, *1*, 16081.
- (111) Lee, J.-W.; Kim, S.-G.; Bae, S.-H.; Lee, D.-K.; Lin, O.; Yang, Y.; Park, N.-G. The Interplay between Trap Density and Hysteresis in Planar Heterojunction Perovskite Solar Cells. *Nano Lett.* **2017**, *17*, 4270–4276
- (112) Yuce, H.; LaFollette, D. K.; Demir, M. M.; Perini, C. A. R.; Correa-Baena, J.-P.

Effects of Alkaline Earth Metal Additives on Methylammonium-Free Lead Halide Perovskite Thin Films and Solar Cells. *Sol. RRL* **2022**, 2100999.

- (113) Shannon, R. D. Revised Effective Ionic Radii and Systematic Studies of Interatomic Distances in Halides and Chalcogenides. *Acta Crystallogr. Sect. A* **1976**, *32*, 751–767.
- (114) Wang, J. T.-W. W.; Wang, Z.; Pathak, S.; Zhang, W.; deQuilettes, D. W.; Wisnivesky-Rocca-Rivarola, F.; Huang, J.; Nayak, P. K.; Patel, J. B.; Mohd Yusof, H. A.; Vaynzof, Y.; Zhu, R.; Ramirez, I.; Zhang, J.; Ducati, C.; Grovenor, C.; Johnston, M. B.; Ginger, D. S.; Nicholas, R. J.; Snaith, H. J.; Yusof, H. A. M. Efficient Perovskite Solar Cells by Metal Ion Doping. *Energy Environ. Sci.* **2016**, *9*, 2892–2901.
- (115) Phung, N.; Félix, R.; Meggiolaro, D.; Al-Ashouri, A.; Sousa e Silva, G.; Hartmann, C.; Hidalgo, J.; Köbler, H.; Mosconi, E.; Lai, B.; Köbler, H.; Mosconi, E.; Lai, B.; Gunder, R.; Li, M.; Wang, K. L.; Wang, Z. K.; Nie, K.; Handick, E.; Wilks, R. G.; Marquez, J. A.; Rech, B.; Unold, T.; Correa-Baena, J. P.; Albrecht, S.; De Angelis, F.; Bär, M.; Abate, A.; Köbler, H.; Mosconi, E.; Lai, B.; Köbler, H.; Mosconi, E.; Lai, B.; Gunder, R.; Li, M.; Wang, K. L.; Wang, Z. K.; Nie, K.; Handick, E.; Wilks, R. G.; Marquez, J. A.; Rech, B.; Unold, T.; Correa-Baena, J. P.; Albrecht, S.; De Angelis, F.; Bär, M.; Abate, A. The Doping Mechanism of Halide Perovskite Unveiled by Alkaline Earth Metals. *J. Am. Chem. Soc.* **2020**, *142*, 2364–2374.
- (116) Chen, Q.; Zhou, H.; Song, T.-B.; Luo, S.; Hong, Z.; Duan, H.-S.; Dou, L.; Liu, Y.; Yang, Y. Controllable Self-Induced Passivation of Hybrid Lead Iodide Perovskites toward High Performance Solar Cells. *Nano Lett* **2014**, *14*, 31.
- (117) Yang, K.; Zhong, L.; Guan, R.; Xiao, M.; Han, D.; Wang, S.; Meng, Y. Carbon Felt Interlayer Derived from Rice Paper and Its Synergistic Encapsulation of Polysulfides for Lithium-Sulfur Batteries. *Appl. Surf. Sci.* **2018**, *441*, 914–922.
- (118) Tang, Y.; Elzinga, E. J.; Jae Lee, Y.; Reeder, R. J. Coprecipitation of Chromate with Calcite: Batch Experiments and X-Ray Absorption Spectroscopy. *Geochim. Cosmochim. Acta* **2007**, *71*, 1480–1493.
- (119) Murugadoss, G.; Thangamuthu, R. Metals Doped Cesium Based All Inorganic Perovskite Solar Cells: Investigations on Structural, Morphological and Optical

- Properties. *Sol. Energy* **2019**, *179*, 151–163.
- (120) Yuan, L.; Luo, H.; Wang, J.; Xu, Z.; Li, J.; Jiang, Q.; Yan, K. Quantifying the Energy Loss for a Perovskite Solar Cell Passivated with Acetamidine Halide. *J. Mater. Chem. A* **2021**, *9*, 4781-4788.
- (121) Wussler, M.; Mayer, T.; Das, C.; Mankel, E.; Hellmann, T.; Prabowo, C.; Zimmermann, I.; Nazeeruddin, M. K.; Jaegermann, W.; Prawobo, C.; Zimmermann, I.; Nazeeruddin, M. K.; Jaegermann, W. Tapered Cross-Section Photoelectron Spectroscopy of State-of-the-Art Mixed Ion Perovskite Solar Cells: Band Bending Profile in the Dark, Photopotential Profile Under Open Circuit Illumination, and Band Diagram. *Adv. Funct. Mater.* **2020**, *30*, 1910679.
- (122) Allen, L. C. Electronegativity Is the Average One-Electron Energy of the Valence-Shell Electrons in Ground-State Free Atoms. *J. Am. Chem. Soc.* **1989**, *111*, 9003-9014.
- (123) Yi, A.; Chae, S.; Lee, H.; Kim, H. J. The Synergistic Effect of Cooperating Solvent Vapor Annealing for High-Efficiency Planar Inverted Perovskite Solar Cells. *J. Mater. Chem. A* **2019**, *7*, 27267–27277.
- (124) Aktas, E.; Phung, N.; Kö, H.; Gonzá Lez, D. A.; Mé Ndez, M.; Kafedjiska, I.; Turren-Cruz, S.-H.; Wenisch, R.; Lauermann, I.; Abate, A.; Palomares, E. Understanding the Perovskite/Self-Assembled Selective Contact Interface for Ultra-Stable and Highly Efficient p-i-n Perovskite Solar Cells. *Energy Environ. Sci.* **2021**, *14*, 3976.
- (125) Leijtens, T.; Eperon, G. E.; Barker, A. J.; Grancini, G.; Zhang, W.; Ball, J. M.; Ram, A.; Kandada, S.; Snaith, H. J.; Petrozza, A. Carrier Trapping and Recombination: The Role of Defect Physics in Enhancing the Open Circuit Voltage of Metal Halide Perovskite Solar Cells. *Energy Environ. Sci.* **2016**, *9*, 3472.
- (126) Yun, J. S.; Seidel, J.; Kim, J.; Soufiani, A. M.; Huang, S.; Lau, J.; Jeon, N. J.; Seok, S. Il; Green, M. A.; Ho-Baillie, A. Critical Role of Grain Boundaries for Ion Migration in Formamidinium and Methylammonium Lead Halide Perovskite Solar Cells. *Adv. Energy Mater.* **2016**, *6*, 1600330.
- (127) Yuan, F.; Ran, C.; Zhang, L.; Dong, H.; Jiao, B.; Hou, X.; Li, J.; Wu, Z. A Cocktail

- of Multiple Cations in Inorganic Halide Perovskite toward Efficient and Highly Stable Blue Light-Emitting Diodes. *ACS Energy Lett.* **2020**, *5*, 1062–1069.
- (128) De Marco, N.; Zhou, H.; Chen, Q.; Sun, P.; Liu, Z.; Meng, L.; Yao, E.-P.; Liu, Y.; Schiffer, A.; Yang, Y. Guanidinium: A Route to Enhanced Carrier Lifetime and Open-Circuit Voltage in Hybrid Perovskite Solar Cells. *Nano Lett.* **2016**, *16*, 1009-1016
- (129) Chen, K.; Jin, W.; Zhang, Y.; Yang, T.; Reiss, P.; Zhong, Q.; Bach, U.; Li, Q.; Wang, Y.; Zhang, H.; Bao, Q.; Liu, Y. High Efficiency Mesoscopic Solar Cells Using CsPbI₃ Perovskite Quantum Dots Enabled by Chemical Interface Engineering. *J. Am. Chem. Soc.* **2020**, *142*, 3775–3783.
- (130) Zhang, X.; Zhang, J.; Phuyal, D.; Du, J.; Tian, L.; Öberg, V. A.; Johansson, M. B.; Cappel, U. B.; Karis, O.; Liu, J.; Rensmo, H.; Boschloo, G.; Johansson, E. M. J. Inorganic CsPbI₃ Perovskite Coating on PbS Quantum Dot for Highly Efficient and Stable Infrared Light Converting Solar Cells. *Adv. Energy Mater.* **2018**, *8*, 1–11.
- (131) Yakunin, S.; Protesescu, L.; Krieg, F.; Bodnarchuk, M. I.; Nedelcu, G.; Humer, M.; De Luca, G.; Fiebig, M.; Heiss, W.; Kovalenko, M. V. Low-Threshold Amplified Spontaneous Emission and Lasing from Colloidal Nanocrystals of Caesium Lead Halide Perovskites. *Nat. Commun.* **2015**, *6*, 8056.
- (132) Huang, X.; Guo, Q.; Yang, D.; Xiao, X.; Liu, X.; Xia, Z.; Fan, F.; Qiu, J.; Dong, G. Reversible 3D Laser Printing of Perovskite Quantum Dots inside a Transparent Medium. *Nat. Photonics* **2020**, *14*, 82–88.
- (133) Bao, C.; Yang, J.; Bai, S.; Xu, W.; Yan, Z.; Xu, Q.; Liu, J.; Zhang, W.; Gao, F. High Performance and Stable All-Inorganic Metal Halide Perovskite-Based Photodetectors for Optical Communication Applications. *Adv. Mater.* **2018**, *30*, 1–8.
- (134) Wu, D.; Zhou, H.; Song, Z.; Zheng, M.; Liu, R.; Pan, X.; Wan, H.; Zhang, J.; Wang, H.; Li, X.; Zeng, H. Welding Perovskite Nanowires for Stable, Sensitive, Flexible Photodetectors. *ACS Nano* **2020**, *14*, 2777–2787.
- (135) Akkerman, Q. A.; D’Innocenzo, V.; Accornero, S.; Scarpellini, A.; Petrozza, A.; Prato, M.; Manna, L. Tuning the Optical Properties of Cesium Lead Halide

- Perovskite Nanocrystals by Anion Exchange Reactions. *J. Am. Chem. Soc.* **2015**, *137*, 10276–10281.
- (136) Brown, A. A. M.; Damodaran, B.; Jiang, L.; Tey, J. N.; Pu, S. H.; Mathews, N.; Mhaisalkar, S. G. Lead Halide Perovskite Nanocrystals: Room Temperature Syntheses toward Commercial Viability. *Adv. Energy Mater.* **2020**, *10*, 2001349
- (137) Yang, D.; Li, X.; Zhou, W.; Zhang, S.; Meng, C.; Wu, Y.; Wang, Y.; Zeng, H. CsPbBr₃ Quantum Dots 2.0: Benzenesulfonic Acid Equivalent Ligand Awakens Complete Purification. *Adv. Mater.* **2019**, *31*, 1900767.
- (138) Seth, S.; Ahmed, T.; De, A.; Samanta, A. Tackling the Defects, Stability, and Photoluminescence of CsPbX₃ Perovskite Nanocrystals. *ACS Energy Lett.* **2019**, *4*, 1610–1618.
- (139) Veldhuis, S. A.; Tay, Y. K. E.; Bruno, A.; Dintakurti, S. S. H.; Bhaumik, S.; Muduli, S. K.; Li, M.; Mathews, N.; Sum, T. C.; Mhaisalkar, S. G. Benzyl Alcohol-Treated CH₃NH₃PbBr₃ Nanocrystals Exhibiting High Luminescence, Stability, and Ultralow Amplified Spontaneous Emission Thresholds. *Nano Lett.* **2017**, *17*, 7424–7432.
- (140) Huang, H.; Bodnarchuk, M. I.; Kershaw, S. V.; Kovalenko, M. V.; Rogach, A. L. Lead Halide Perovskite Nanocrystals in the Research Spotlight: Stability and Defect Tolerance. *ACS Energy Lett.* **2017**, *2*, 2071–2083.
- (141) Ng, C. K.; Wang, C.; Jasieniak, J. J. Synthetic Evolution of Colloidal Metal Halide Perovskite Nanocrystals. *Langmuir* **2019**, *35*, 2021.
- (142) Van der Stam, W.; Geuchies, J. J.; Altantzis, T.; Van Den Bos, K. H. W.; Meeldijk, J. D.; Van Aert, S.; Bals, S.; Vanmaekelbergh, D.; De Mello Donega, C. Highly Emissive Divalent-Ion-Doped Colloidal CsPb_{1-x}M_xBr₃ Perovskite Nanocrystals through Cation Exchange. *J. Am. Chem. Soc.* **2017**, *139*, 4087–4097.
- (143) Vashishtha, P.; White, T.; Hanna, J. V.; Griffith, B. E.; Brown, A. A. M.; Hooper, T. J. N.; Fang, Y.; Ansari, M. S.; Bruno, A.; Pu, S. H.; Mhaisalkar, S. G. Performance Enhanced Light-Emitting Diodes Fabricated from Nanocrystalline CsPbBr₃ with in Situ Zn²⁺ Addition. *ACS Appl. Electron. Mater.* **2020**, *2*, 4002–4011.

- (144) Imran, M.; Ramade, J.; Di Stasio, F.; De Franco, M.; Buha, J.; Van Aert, S.; Goldoni, L.; Lauciello, S.; Prato, M.; Infante, I.; Bals, S.; Manna, L. Alloy CsCd_xPb_{1-x}Br₃ Perovskite Nanocrystals: The Role of Surface Passivation in Preserving Composition and Blue Emission. *Chem. Mater.* **2020**, *32*, 10641–10652.
- (145) Liu, W.; Lin, Q.; Li, H.; Wu, K.; Robel, I.; Pietryga, J. M.; Klimov, V. I. Mn²⁺-Doped Lead Halide Perovskite Nanocrystals with Dual-Color Emission Controlled by Halide Content. *J. Am. Chem. Soc.* **2016**, *138*, 14954–14961.
- (146) Parobek, D.; Dong, Y.; Qiao, T.; Son, D. H. Direct Hot-Injection Synthesis of Mn-Doped CsPbBr₃ Nanocrystals. *Chem. Mater.* **2018**, *30*, 2939–2944.
- (147) Li, M.; Zhang, X.; Matras-Postolek, K.; Chen, H. S.; Yang, P. An Anion-Driven Sn²⁺ Exchange Reaction in CsPbBr₃ Nanocrystals towards Tunable and High Photoluminescence. *J. Mater. Chem. C* **2018**, *6*, 5506–5513.
- (148) Yao, J. S.; Ge, J.; Han, B. N.; Wang, K. H.; Yao, H. Bin; Yu, H. L.; Li, J. H.; Zhu, B. S.; Song, J. Z.; Chen, C.; Zhang, Q.; Zeng, H. B.; Luo, Y.; Yu, S. H. Ce³⁺-Doping to Modulate Photoluminescence Kinetics for Efficient CsPbBr₃ Nanocrystals Based Light-Emitting Diodes. *J. Am. Chem. Soc.* **2018**, *140*, 3626–3634.
- (149) Begum, R.; Parida, M. R.; Abdelhady, A. L.; Murali, B.; Alyami, N. M.; Ahmed, G. H.; Hedhili, M. N.; Bakr, O. M.; Mohammed, O. F. Engineering Interfacial Charge Transfer in CsPbBr₃ Perovskite Nanocrystals by Heterovalent Doping. *J. Am. Chem. Soc.* **2017**, *139*, 731–737.
- (150) Zhang, X.; Wang, H.; Hu, Y.; Pei, Y.; Wang, S.; Shi, Z.; Colvin, V. L.; Wang, S.; Zhang, Y.; Yu, W. W. Strong Blue Emission from Sb³⁺-Doped Super Small CsPbBr₃ Nanocrystals. *J. Phys. Chem. Lett.* **2019**, *10*, 1750–1756.
- (151) Liu, M.; Zhong, G.; Yin, Y.; Miao, J.; Li, K.; Wang, C.; Xu, X.; Shen, C.; Meng, H. Aluminum-Doped Cesium Lead Bromide Perovskite Nanocrystals with Stable Blue Photoluminescence Used for Display Backlight. *Adv. Sci.* **2017**, *4*, 1700335.
- (152) Pradeep, K. R.; Viswanatha, R. Mechanism of Mn Emission: Energy Transfer vs Charge Transfer Dynamics in Mn-Doped Quantum Dots. *APL Mater.* **2020**, *8*, 020901.

- (153) Huang, G.; Wang, C.; Xu, S.; Zong, S.; Lu, J.; Wang, Z.; Lu, C.; Cui, Y. Postsynthetic Doping of MnCl_2 Molecules into Preformed CsPbBr_3 Perovskite Nanocrystals via a Halide Exchange-Driven Cation Exchange. *Adv. Mater.* **2017**, *29*, 1700095.
- (154) Shao, H.; Bai, X.; Cui, H.; Pan, G.; Jing, P.; Qu, S.; Zhu, J.; Zhai, Y.; Dong, B.; Song, H. White Light Emission in $\text{Bi}^{3+}/\text{Mn}^{2+}$ Ion Co-Doped CsPbCl_3 Perovskite Nanocrystals. *Nanoscale* **2018**, *10*, 1023–1029.
- (155) Cao, Z.; Li, J.; Wang, L.; Xing, K.; Yuan, X.; Zhao, J.; Gao, X.; Li, H. Enhancing Luminescence of Intrinsic and Mn Doped CsPbCl_3 Perovskite Nanocrystals through Co^{2+} Doping. *Mater. Res. Bull.* **2020**, *121*, 110608.
- (156) Xing, K.; Yuan, X.; Wang, Y.; Li, J.; Wang, Y.; Fan, Y.; Yuan, L.; Li, K.; Wu, Z.; Li, H.; Zhao, J. Improved Doping and Emission Efficiencies of Mn-Doped CsPbCl_3 Perovskite Nanocrystals via Nickel Chloride. *J. Phys. Chem. Lett.* **2019**, *10*, 4177–4184.
- (157) Cai, T.; Wang, J.; Li, W.; Hills-Kimball, K.; Yang, H.; Nagaoka, Y.; Yuan, Y.; Zia, R.; Chen, O. $\text{Mn}^{2+}/\text{Yb}^{3+}$ Codoped CsPbCl_3 Perovskite Nanocrystals with Triple-Wavelength Emission for Luminescent Solar Concentrators. *Adv. Sci.* **2020**, *7*, 2001317.
- (158) Zhang, J.; Zheng, Y.; Liu, G.; Ma, Y.; Gong, L.; Guan, R.; Cui, X.; Yan, J.; Zhao, J.; Yang, J. Pressure-Engineered Optical and Charge Transport Properties of $\text{Mn}^{2+}/\text{Cu}^{2+}$ Codoped CsPbCl_3 Perovskite Nanocrystals via Structural Progression. *ACS Appl. Mater. Interfaces* **2020**, *12*, 48225–48236.
- (159) Yuce, H.; Mandal, M.; Yalcinkaya, Y.; Andrienko, D.; Demir, M. M. Improvement of Photophysical Properties of CsPbBr_3 and $\text{Mn}^{2+}:\text{CsPb}(\text{Br},\text{Cl})_3$ Perovskite Nanocrystals by Sr^{2+} Doping for White Light-Emitting Diodes. *J. Phys. Chem. C* **2022**.
- (160) Lv, W.; Tang, X.; Li, L.; Xu, L.; Li, M.; Chen, R.; Huang, W. Assessment for Anion-Exchange Reaction in CsPbX_3 ($\text{X} = \text{Cl}, \text{Br}, \text{I}$) Nanocrystals from Bond Strength of Inorganic Salt. *J. Phys. Chem. C* **2019**, *123*, 24313–24320.
- (161) Luo, Y. R. Comprehensive Handbook of Chemical Bond Energies. *Compr. Handb. Chem. Bond Energies* **2007**.

- (162) Yao, J. S.; Ge, J.; Wang, K. H.; Zhang, G.; Zhu, B. S.; Chen, C.; Zhang, Q.; Luo, Y.; Yu, S. H.; Yao, H. Bin. Few-Nanometer-Sized α -CsPbI₃ Quantum Dots Enabled by Strontium Substitution and Iodide Passivation for Efficient Red-Light Emitting Diodes. *J. Am. Chem. Soc.* **2019**, *141*, 2069–2079.
- (163) Dong, Y.; Qiao, T.; Kim, D.; Parobek, D.; Rossi, D.; Son, D. H. Precise Control of Quantum Confinement in Cesium Lead Halide Perovskite Quantum Dots via Thermodynamic Equilibrium. *Nano Lett.* **2018**, *18*, 3716–3722.
- (164) Stoumpos, C. C.; Malliakas, C. D.; Peters, J. A.; Liu, Z.; Sebastian, M.; Im, J.; Chasapis, T. C.; Wibowo, A. C.; Chung, D. Y.; Freeman, A. J.; Wessels, B. W.; Kanatzidis, M. G. Crystal Growth of the Perovskite Semiconductor CsPbBr₃: A New Material for High-Energy Radiation Detection. *Cryst. Growth Des.* **2013**, *13*, 2722–2727.
- (165) Becker, M. A.; Vaxenburg, R.; Nedelcu, G.; Sercel, P. C.; Shabaev, A.; Mehl, M. J.; Michopoulos, G.; Lambrakos, S. G.; Bernstein, N.; Lyons, L.; Stöferle, T.; Mahrt, F.; Kovalenko, M. V.; Norris, D. J.; Rainò, G.; Efros, A. L. Bright Triplet Excitons in Caesium Lead Halide Perovskites. *Nature* **2018**, *553*, 189-193.
- (166) Ahmed, G. H.; El-Demellawi, J. K.; Yin, J.; Pan, J.; Velusamy, D. B.; Hedhili, M. N.; Alarousu, E.; Bakr, O. M.; Alshareef, H. N.; Mohammed, O. F. Giant Photoluminescence Enhancement in CsPbCl₃ Perovskite Nanocrystals by Simultaneous Dual-Surface Passivation. *ACS Energy Lett.* **2018**, *3*, 2301–2307.
- (167) Ahmed, T.; Seth, S.; Samanta, A. Boosting the Photoluminescence of CsPbX₃ (X = Cl, Br, I) Perovskite Nanocrystals Covering a Wide Wavelength Range by Postsynthetic Treatment with Tetrafluoroborate Salts. *Chem. Mater.* **2018**, *30*, 3633–3637.
- (168) Bohn, B. J.; Tong, Y.; Gramlich, M.; Lai, M. L.; Döblinger, M.; Wang, K.; Hoye, R. L. Z.; Müller-Buschbaum, P.; Stranks, S. D.; Urban, A. S.; Polavarapu, L.; Feldmann, J. Boosting Tunable Blue Luminescence of Halide Perovskite Nanoplatelets through Postsynthetic Surface Trap Repair. *Nano Lett.* **2018**, *18*, 5231–5238.
- (169) Parobek, D.; Roman, B. J.; Dong, Y.; Jin, H.; Lee, E.; Sheldon, M.; Son, D. H. Exciton-to-Dopant Energy Transfer in Mn-Doped Cesium Lead Halide Perovskite

- Nanocrystals. *Nano Lett.* **2016**, *16*, 7376–7380.
- (170) Li, F.; Xia, Z.; Gong, Y.; Gu, L.; Liu, Q. Optical Properties of Mn²⁺ Doped Cesium Lead Halide Perovskite Nanocrystals via a Cation-Anion Co-Substitution Exchange Reaction. *J. Mater. Chem. C* **2017**, *5*, 9281.
- (171) Marronnier, A.; Roma, G.; Boyer-Richard, S.; Pedesseau, L.; Jancu, J. M.; Bonnassieux, Y.; Katan, C.; Stoumpos, C. C.; Kanatzidis, M. G.; Even, J. Anharmonicity and Disorder in the Black Phases of Cesium Lead Iodide Used for Stable Inorganic Perovskite Solar Cells. *ACS Nano* **2018**, *12*, 3477–3486.
- (172) Sutton, R. J.; Filip, M. R.; Haghighirad, A. A.; Sakai, N.; Wenger, B.; Giustino, F.; Snaith, H. J. Cubic or Orthorhombic? Revealing the Crystal Structure of Metastable Black-Phase CsPbI₃ by Theory and Experiment. *ACS Energy Lett* **2018**, *3*, 1787–1794.
- (173) Eperon, G. E.; Paternò, G. M.; Sutton, R. J.; Zampetti, A.; Haghighirad, A. A.; Cacialli, F.; Snaith, H. J. Inorganic Caesium Lead Iodide Perovskite Solar Cells. *J. Mater. Chem. A* **2015**, *3*, 19688–19695.
- (174) Sun, J. K.; Huang, S.; Liu, X. Z.; Xu, Q.; Zhang, Q. H.; Jiang, W. J.; Xue, D. J.; Xu, J. C.; Ma, J. Y.; Ding, J.; Ge, Q. Q.; Gu, L.; Fang, X. H.; Zhong, H. Z.; Hu, J. S.; Wan, L. J. Polar Solvent Induced Lattice Distortion of Cubic CsPbI₃ Nanocubes and Hierarchical Self-Assembly into Orthorhombic Single-Crystalline Nanowires. *J. Am. Chem. Soc.* **2018**, *140*, 11705–11715.
- (175) De Roo, J.; Iba, M.; Geiregat, P.; Nedelcu, G.; Walravens, W.; Maes, J.; Martins, J. C.; Van Driessche, I.; Kovalenko, M. V.; Hens, Z. Highly Dynamic Ligand Binding and Light Absorption Coefficient of Cesium Lead Bromide Perovskite Nanocrystals. *ACS Nano* **2016**, *10*, 18.
- (176) Chen, K.; Zhong, Q.; Chen, W.; Sang, B.; Wang, Y.; Yang, T.; Liu, Y.; Zhang, Y.; Zhang, H. Short-Chain Ligand-Passivated Stable α -CsPbI₃ Quantum Dot for All-Inorganic Perovskite Solar Cells. *Adv. Funct. Mater.* **2019**, *29*.
- (177) Liu, F.; Ding, C.; Zhang, Y.; Ripolles, T. S.; Kamisaka, T.; Toyoda, T.; Hayase, S.; Minemoto, T.; Yoshino, K.; Dai, S.; Yanagida, M.; Noguchi, H.; Shen, Q. Colloidal Synthesis of Air-Stable Alloyed CsSn_{1-x}Pb_xI₃ Perovskite Nanocrystals for Use in Solar Cells. *J. Am. Chem. Soc.* **2017**, *139*, 16708–16719.

- (178) Akkerman, Q. A.; Meggiolaro, D.; Dang, Z.; De Angelis, F.; Manna, L. Fluorescent Alloy $\text{CsPb}_x\text{Mn}_{1-x}\text{I}_3$ Perovskite Nanocrystals with High Structural and Optical Stability. *ACS Energy Lett.* **2017**, *2*, 2183–2186.
- (179) Liu, F.; Zhang, Y.; Ding, C.; Kobayashi, S.; Izuishi, T.; Nakazawa, N.; Toyoda, T.; Ohta, T.; Hayase, S.; Minemoto, T.; Yoshino, K.; Dai, S.; Shen, Q. Highly Luminescent Phase-Stable CsPbI_3 Perovskite Quantum Dots Achieving Near 100% Absolute Photoluminescence Quantum Yield. *ACS Nano* **2017**, *11*, 10373–10383.
- (180) Kim, J.; Cho, S.; Dinic, F.; Choi, J.; Choi, C.; Jeong, S. M.; Lee, J. S.; Voznyy, O.; Ko, M. J.; Kim, Y. Hydrophobic Stabilizer-Anchored Fully Inorganic Perovskite Quantum Dots Enhance Moisture Resistance and Photovoltaic Performance. *Nano Energy* **2020**, *75*, 104985.
- (181) Sun, Y.; Zheng, W. Surface Molecular Imprinting on Polystyrene Resin for Selective Adsorption of 4-Hydroxybenzoic Acid. *Chemosphere* **2021**, *269*, 128762.
- (182) Yi, C.; Liu, C.; Wen, K.; Liu, X. K.; Zhang, H.; Yu, Y.; Fan, N.; Ji, F.; Kuang, C.; Ma, B.; Tu, C.; Zhang, Y.; Xue, C.; Li, R.; Gao, F.; Huang, W.; Wang, J. Intermediate-Phase-Assisted Low-Temperature Formation of $\gamma\text{-CsPbI}_3$ Films for High-Efficiency Deep-Red Light-Emitting Devices. *Nat. Commun.* **2020**, *11*, 1–8.
- (183) Steele, J. A.; Prakasam, V.; Huang, H.; Solano, E.; Chernyshov, D.; Hofkens, J.; Roeffaers, M. B. J. Trojans That Flip the Black Phase: Impurity-Driven Stabilization and Spontaneous Strain Suppression in $\gamma\text{-CsPbI}_3$ Perovskite. *J. Am. Chem. Soc.* **2021**, *143*, 10500–10508.
- (184) Zhu, C.; Niu, X.; Fu, Y.; Li, N.; Hu, C.; Chen, Y.; He, X.; Na, G.; Liu, P.; Zai, H.; Ge, Y.; Lu, Y.; Ke, X.; Bai, Y.; Yang, S.; Chen, P.; Li, Y.; Sui, M.; Zhang, L.; Zhou, H.; Chen, Q. Strain Engineering in Perovskite Solar Cells and Its Impacts on Carrier Dynamics.
- (185) Jena, A. K.; Kulkarni, A.; Sanehira, Y.; Ikegami, M.; Miyasaka, T. Stabilization of $\alpha\text{-CsPbI}_3$ in Ambient Room Temperature Conditions by Incorporating Eu into CsPbI_3 . *Chem. Mater.* **2018**, *30*, 6668–6674.
- (186) Nath, D.; Singh, F.; Das, R. X-Ray Diffraction Analysis by Williamson-Hall,

- Halder-Wagner and Size-Strain Plot Methods of CdSe Nanoparticles-a Comparative Study. *Mater. Chem. Phys.* **2020**, *239*, 122021.
- (187) Kumar, Y.; Regalado-Pérez, E.; Ayala, A. M.; Mathews, N. R.; Mathew, X. Effect of Heat Treatment on the Electrical Properties of Perovskite Solar Cells. *Sol. Energy Mater. Sol. Cells* **2016**, *157*, 10–17.
- (188) Urbach, F. The Long-Wavelength Edge of Photographic Sensitivity and of the Electronic Absorption of Solids. *Phys. Rev.* **1953**, *92*, 1324.
- (189) Studenyak, I.; Kranjčec, M.; Kurik, M. Urbach Rule in Solid State Physics. *Int. J. Opt. Appl.* **2014**, *4*, 96–104.
- (190) Imran, M.; Caligiuri, V.; Wang, M.; Goldoni, L.; Prato, M.; Krahne, R.; De Trizio, L.; Manna, L. Benzoyl Halides as Alternative Precursors for the Colloidal Synthesis of Lead-Based Halide Perovskite Nanocrystals. *J. Am. Chem. Soc.* **2018**, *140*, 2656–2664.

APPENDIX A

SUPPORTING INFORMATION

Supplementary Note 1: Williamson-Hall (W-H) method to calculate microstrain and crystallite size.

The crystallite size and the lattice strain in the films can be calculated by using Williamson-Hall method (W-H) in equations (S1) and (S2)^{79,112,159,186,187}.

$$\beta = (\beta_{measured}^2 - \beta_{instrumental}^2)^{1/2} \quad (S1)$$

$$\beta \cos\theta = \frac{k\lambda}{D} + 4 \epsilon \sin\theta \quad (S2)$$

Where D , λ , β , θ and k ($= 0.9$) is crystallite size, the wavelength of the radiation, the FWHM, the peak position and is a constant, respectively. The microstrain in the lattice is notated by ϵ . Even though $\beta_{instrumental}$ was not determined, micro-strain, ϵ and crystallite size, D for the samples can be comparable according to the equation (S2).

The microstrain (ϵ) and crystallite size (D) were calculated respectively from slope and y-intercept of the graph obtained by plotting $\beta \cos(\theta)$ against $4 \sin(\theta)$. Here, the slope is equal to ϵ , and $\frac{k\lambda}{D}$ gives y-intercept.

Supplementary Note 2: Tauc plot calculations.

By using the absorbance spectra of the perovskite films, the optical bandgap (E_g) was calculated from Tauc's plot^{79,90,112,159}; $\alpha hv = \beta(hv - E_g)^x$; where $x = 1/2$ for the direct bandgap. In the equation, α , hv , and β are absorption coefficient, the energy of the photon, and a constant, respectively.

Supplementary Note 3: Urbach energy calculations.

The energetic disorder at the band edge is defined by the Urbach energy (E_u). Absorption coefficient (α) is dependent on the energy ($E = h\nu$) and temperature (T) by the equation (S3)^{79,188,189}

$$(h\nu, T) = \alpha_0 \cdot \exp\left[\frac{\sigma (h\nu - E_0)}{kT}\right] = \alpha_0 \cdot \exp\left[\frac{h\nu - E_0}{E_U(T)}\right] \quad (\text{S3})$$

In the equation, σ is the steepness parameter of the absorption edge. α_0 and E_0 refer to the coordinates of the convergence point of the Urbach bundle. Urbach energy (E_u) can be obtained by the following equation (S4);

$$\frac{1}{E_U} = \frac{\Delta(\ln\alpha)}{\Delta(h\nu)} \quad (\text{S4})$$

Supplementary Note 4: *Time Resolved Spectroscopic Characterization*

The PL decays of perovskite NCs showed triple/double exponential behavior and fitted accordingly. The decay lifetimes of all samples exhibits a complex multi-exponential decay trend which were fitted with a two/three-exponential relation^{159,190} (equation S5):

$$I(t) = A_1 \cdot e^{-\frac{t}{\tau_1}} + A_2 \cdot e^{-\frac{t}{\tau_2}} + A_3 \cdot e^{-\frac{t}{\tau_3}} \quad (\text{S5})$$

In equation S5, A_1 , A_2 and A_3 are the amplitudes of decay time components and τ_1 , τ_2 and τ_3 are the related decay time constants. The average decay lifetime was calculated by using these values, as equation (S6):

$$\tau_{average} = \frac{A_1 \cdot \tau_1^2 + A_2 \cdot \tau_2^2 + A_3 \cdot \tau_3^2}{A_1 \cdot \tau_1 + A_2 \cdot \tau_2 + A_3 \cdot \tau_3} \quad (\text{S6})$$

Data Analyses of Chapter 2:

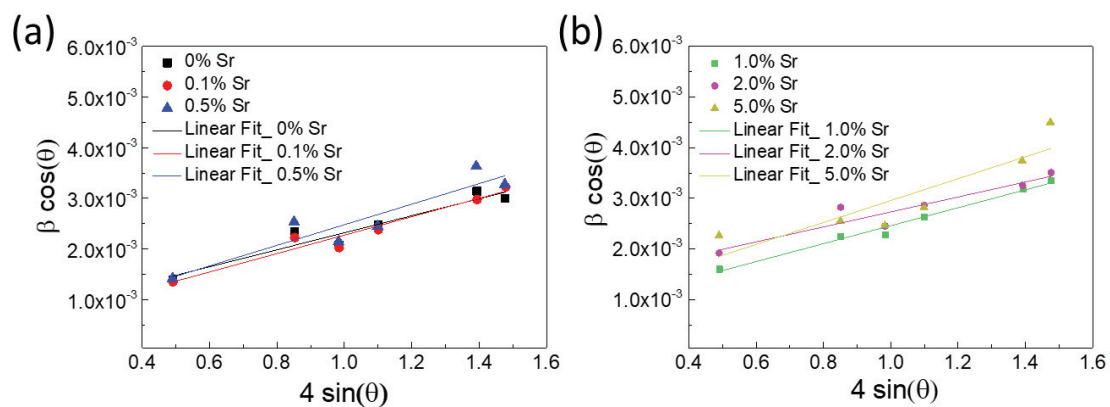


Figure S2.1. W-H plot of a) pristine, 0.1%, and 0.5% and b) 1.0%, 2.0%, and 5.0% SrI₂ added perovskite films.

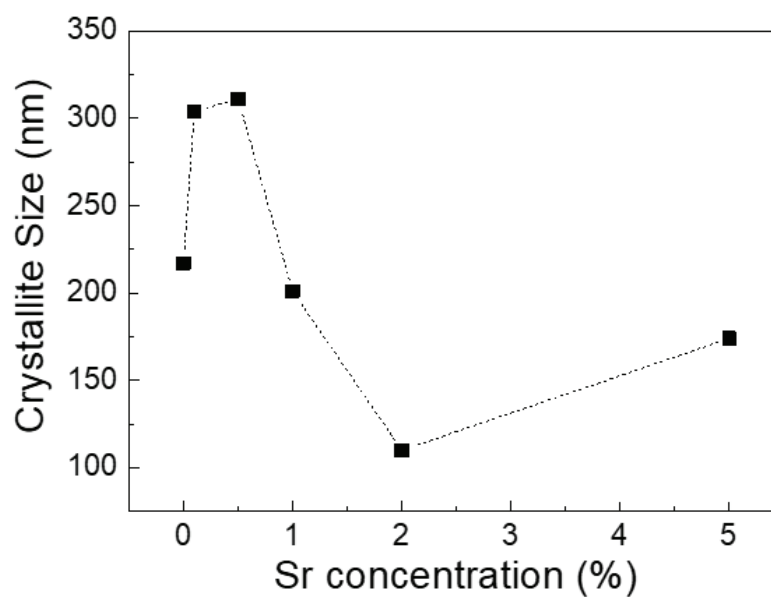


Figure S2.2. Crystallite size of each perovskite film calculated from W-H plot.

Table S2.1. Calculated strain (ϵ), y-intercept, and correlation coefficient (R^2), crystallite size of perovskite films from W-H plot.

Sr concentration	" ϵ " Strain (%)	Standard Error for ϵ	y-intercept	Standard Error for y-intercept	" R^2 " Correlation coefficient	"D" crystallite size (nm)
0%	0.168	2.53E-04	6.39E-04	2.79E-04	0.89595	217.0
0.1%	0.182	2.03E-04	4.56E-04	2.24E-04	0.94036	304.1
0.5%	0.203	4.04E-04	4.45E-04	4.44E-04	0.82957	311.3
1.0%	0.177	1.02E-04	6.87E-04	1.13E-04	0.98351	201.7
2.0%	0.148	2.56E-04	0.00125	2.81E-04	0.86602	110.8
5.0%	0.216	5.42E-04	7.93E-04	5.96E-04	0.74884	174.7

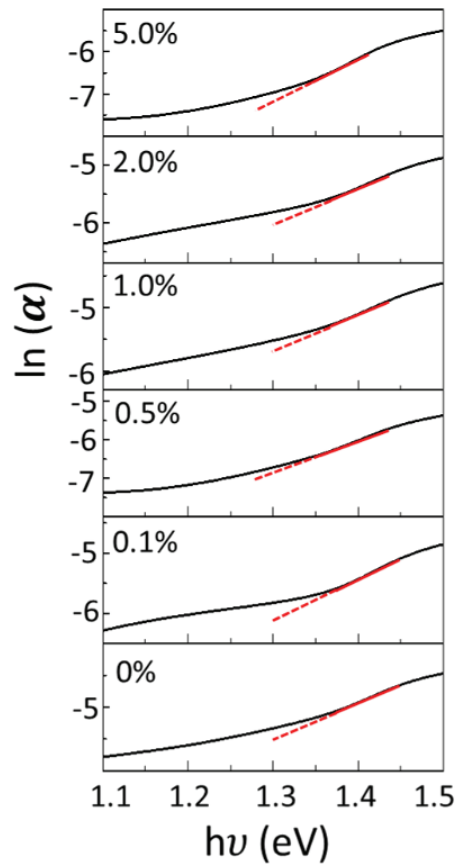


Figure S2.3. Urbach tails of the perovskite samples.

Table S2.2. Calculated Urbach energy of the perovskite films from linear fitting of Urbach tail.

Sr concentration	Slope	Standard Error of the slope	“R ² ” Correlation coefficient	“E _u ” Urbach Energy (eV)
0%	5.47189	0.0312	0.99841	0.182
0.1%	6.92985	0.02713	0.99942	0.144
0.5%	8.37974	0.03344	0.99909	0.119
1.0%	5.80626	0.0159	0.99968	0.172
2.0%	6.31708	0.01794	0.99967	0.158
5.0%	10.01557	0.04737	0.99897	0.099

Data Analyses of Chapter 3:

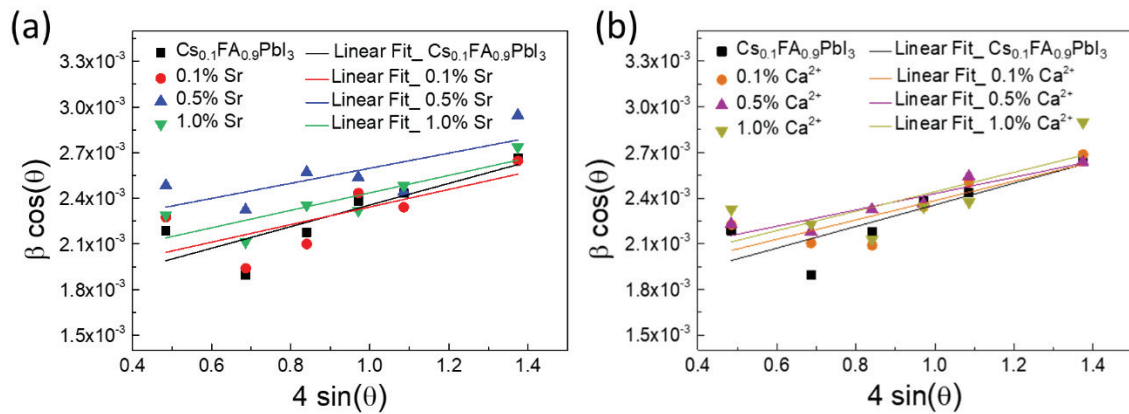


Figure S3.1. Williamson-Hall plot of a) Sr²⁺ and b) Ca²⁺ added perovskite films.

Table S3.1. Calculated strain (ϵ) and y-intercept of perovskite films from W-H plot.

Perovskite Materials	“ ϵ ” Strain (%)	Standard Error for ϵ	y- intercept	Standard Error for y- intercept
$\text{Cs}_{0.1}\text{FA}_{0.9}\text{PbI}_3$	7.11E-02	2.32E-04	0.00165	2.20E-04
0.1% Sr^{2+}	5.78E-02	2.75E-04	0.00176	2.62E-04
0.5% Sr^{2+}	4.96E-02	2.32E-04	0.0021	2.20E-04
1.0% Sr^{2+}	5.74E-02	1.76E-04	0.00186	1.68E-04
0.1% Ca^{2+}	6.36E-02	2.04E-04	0.00175	1.94E-04
0.5% Ca^{2+}	5.36E-02	1.02E-04	0.00189	9.69E-05
1.0 % Ca^{2+}	6.40E-02	2.87E-04	0.0018	2.73E-04

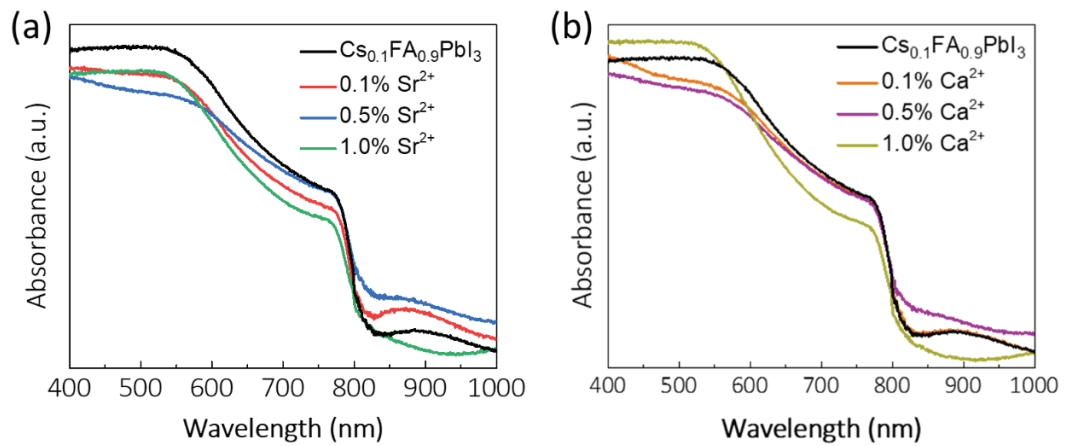


Figure S3.2. Absorption spectra of a) Sr^{2+} and b) Ca^{2+} additive perovskite series.

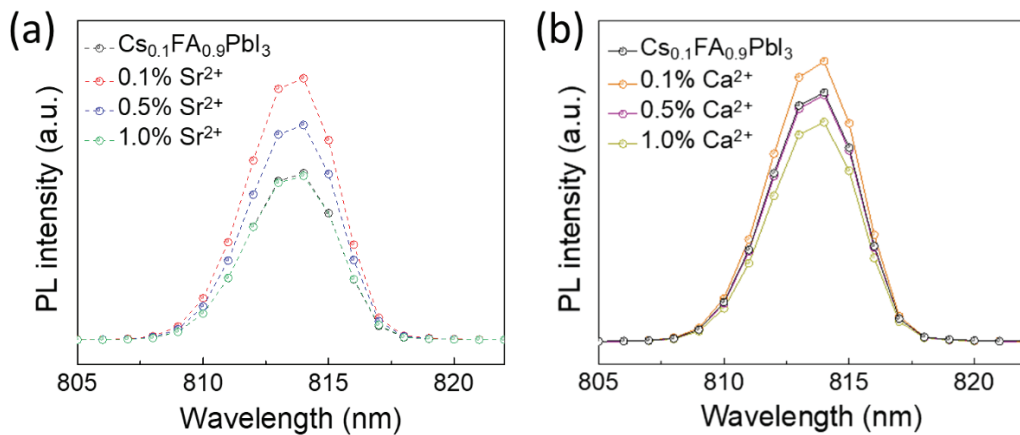


Figure S3.3. PL spectra of a) Sr^{2+} and b) Ca^{2+} additive perovskite series.

Data Analyses of Chapter 4:

Table S4.1. Lattice parameters of perovskite NCs.

Sample	a(Å)	b(Å)	c(Å)
CsPbBr ₃	8.2768	11.7667	8.19181
1% Sr ²⁺ :CsPbBr ₃	8.2976	11.7626	8.17733
2% Sr ²⁺ :CsPbBr ₃	8.38	11.7262	8.36262
5% Sr ²⁺ :CsPbBr ₃	8.2832	11.7747	8.18562
10% Sr ²⁺ :CsPbBr ₃	8.2704	11.7444	8.21592
0% Sr ²⁺ : Mn ²⁺ :CsPb(Br,Cl) ₃	8.1324	11.4667	8.11694
2% Sr ²⁺ : Mn ²⁺ :CsPb(Br,Cl) ₃	8.1324	11.4774	8.10173

The parameters of pristine and Sr²⁺:CsPbBr₃ were calculated from the XRD signals at the angle of ~15° (101), ~21° (200), and ~43° (242). Those of 0% and 2% Sr²⁺:Mn²⁺:CsPb(Br,Cl)₃ were calculated from XRD peaks at ~22° (200), ~31° (202), and ~43° (242). For these calculations, three peaks at the highest intensities were chosen.

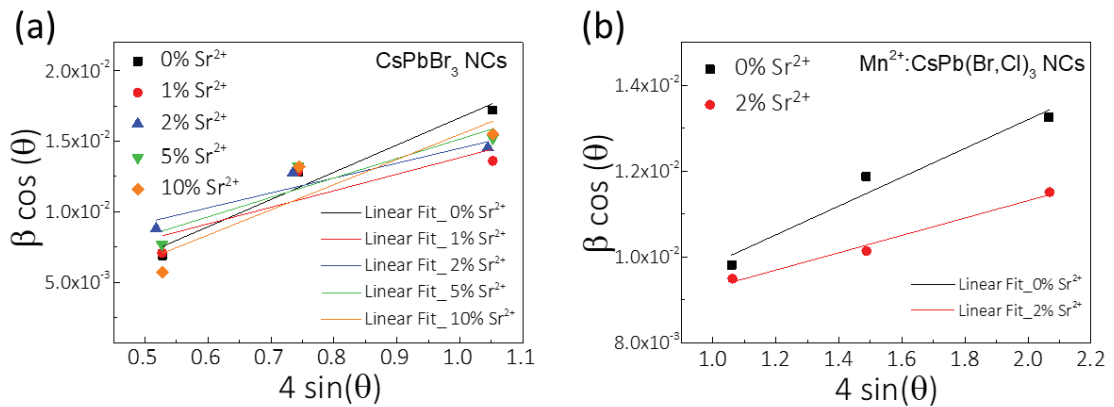


Figure S4.1. W-H plots of a) pristine and Sr²⁺:CsPbBr₃ NCs and b) Mn²⁺:CsPb(Br,Cl)₃ and 2% Sr²⁺:Mn²⁺:CsPb(Br,Cl)₃ NCs. Peaks at high intensities for the fitting were (101) ~15.2°, (200) ~21.4°, (202) ~30.6° for CsPbBr₃ and (101) ~15.4°, (200) ~22.0°, (202) ~31.1° for Mn²⁺:CsPb(Br,Cl)₃ NCs.

Table S4.2. Calculated strain (ϵ) and linear fit parameters of perovskite NCs from W-H plots.

Samples	Strain, ϵ	Standard error, E	R value	Adj R²	R² (COD)	Root MSE (SD)
CsPbBr ₃	0.01932	0.00364	0.9827	0.93139	0.96569	0.00136
1% Sr ²⁺ : CsPbBr ₃	0.01173	0.00673	0.86748	0.50504	0.75252	0.00251
2% Sr ²⁺ : CsPbBr ₃	0.01055	0.00339	0.95214	0.81315	0.90658	0.00127
5% Sr ²⁺ : CsPbBr ₃	0.01378	0.00535	0.93229	0.73831	0.86916	0.002
10% Sr ²⁺ : CsPbBr ₃	0.01785	0.00752	0.92149	0.69828	0.84914	0.00281
0% Sr ²⁺ : Mn ²⁺ : CsPb(Br,Cl) ₃	0.00336	6.85197E-4	0.97981	0.92004	0.96002	4.89566 E-4
2% Sr ²⁺ : Mn ²⁺ : CsPb(Br,Cl) ₃	0.00202	2.34983E-4	0.99332	0.97337	0.98668	1.67756 E-4

Table S4.3. The average lifetime parameters of all perovskite samples with their amplitudes and related decay time constants taken into account.

Samples	A ₁	τ_1 (ns)	A ₂	τ_2 (ns)	A ₃	τ_3 (ns)	τ_{Avg} (ns)
CsPbBr ₃	2264.89	0.89	2388.62	3.75	545.07	13.96	7.62
1% Sr ²⁺ : CsPbBr ₃	2634.18	0.71	1834.48	3.20	570.90	14.04	8.42
2% Sr ²⁺ : CsPbBr ₃	1703.66	1.03	2619.26	4.30	731.90	17.16	10.39
5% Sr ²⁺ : CsPbBr ₃	1601.57	1.04	2669.50	3.80	715.96	12.45	7.30
10% Sr ²⁺ : CsPbBr ₃	1844.66	0.88	2579.43	3.28	755.94	11.44	6.84
0% Sr ²⁺ : Mn ²⁺ : CsPb(Br,Cl) ₃	1113.39	1.00	2851.95	4.51	975.35	15.16	9.85
2% Sr ²⁺ : Mn ²⁺ : CsPb(Br,Cl) ₃	945.51	0.87	2838.23	4.36	1051.62	15.07	10.10

Data Analyses of Chapter 5:

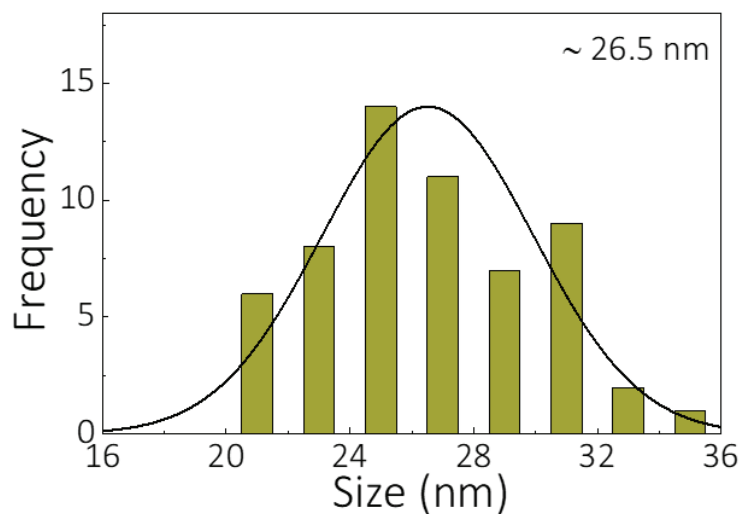


Figure S5.1. Size distribution of CsPbI₃ NCs

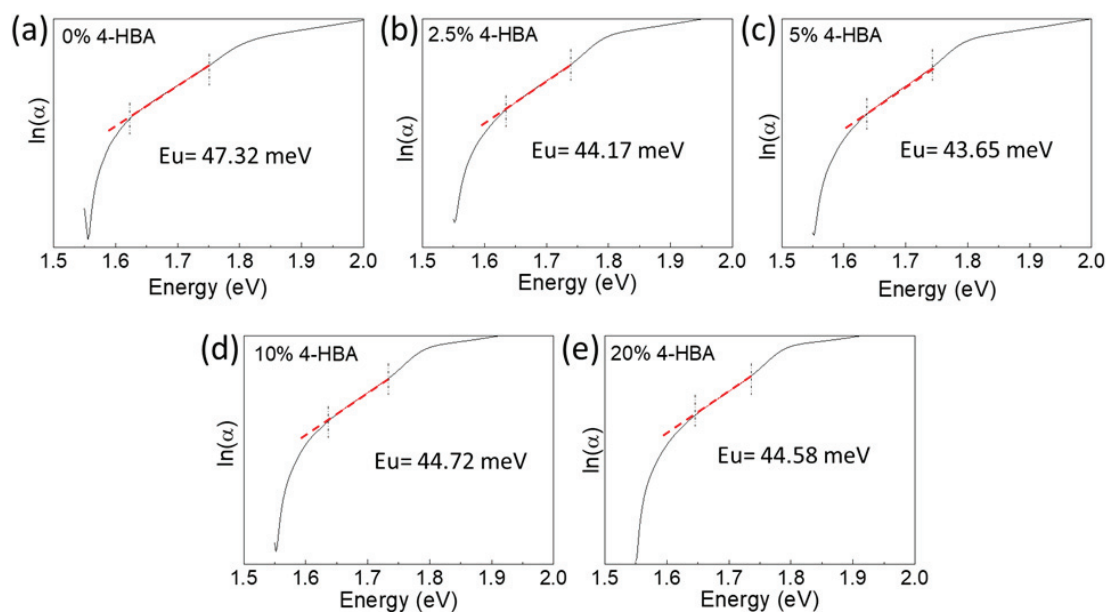


Figure S5.2. Urbach tails of CsPbI₃ perovskite samples with different 4-HBA concentrations

Table S5.1. Calculated Urbach energy of the perovskite films from linear fitting of Urbach tail.

4-HBA concentration	Slope	Standard Error	“R ² ” Correlation coefficient	“E _U ” Urbach Energy (meV)
0%	21.13	0.10675	0.9986	47.32
2.5%	22.64	0.10227	0.9990	44.17
5.0%	22.91	0.08398	0.9994	43.65
10%	22.36	0.06467	0.9997	44.72
20%	22.43	0.06245	0.9997	44.58

Table S5.2. Fitting parameters of TRPL decay of CsPbI₃ NCs with various 4-HBA amounts.

Sample	A ₁	τ ₁ (ns)	A ₂	T ₂ (ns)	<τ> (ns)
CsPbI ₃ -0% HBA	608.322	30.8822	238.571	135.5374	97
CsPbI ₃ -2.5% HBA	412.975	40.7376	476.962	189.6387	166
CsPbI ₃ -5.0% HBA	477.504	55.3569	425.953	241.7866	203
CsPbI ₃ -10% HBA	467.09	29.4833	333.604	222.5369	192
CsPbI ₃ -20% HBA	366.743	28.5436	380.997	198.1038	177

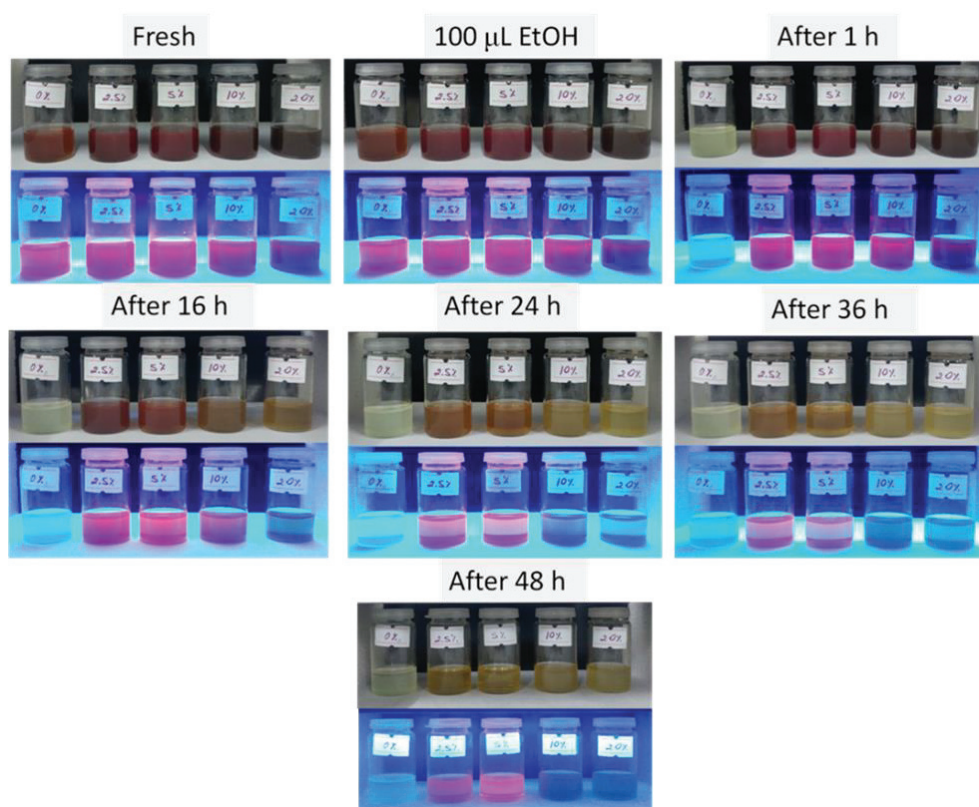


Figure S5.3. Images of CsPbI₃ NCs with varying 4-HBA concentrations after 1 h, 16 h, 24 h, 36 h, and 48 h ethanol exposure under daylight and UV light. The vials are ordered with the concentration of 4-HBA at 0%, 2.5%, 5%, 10%, and 20%, respectively from left to right.

VITA

Full Name: Hürriyet YÜCE ÇAKIR

Education

<u>Degree</u>	<u>Institution, Department</u>	<u>Year</u>
M.Sc.	Izmir Institute of Technology, Physics	2015
B.Sc.	Balikesir University, Physics	2011

Work Experience

<u>Year</u>	<u>Place</u>	<u>Enrollment</u>
2018-2022	Izmir Institute of Technology	Research Assistant
2019-2020	Georgia Institute of Technology	Research Scholar
2014-2017	Izmir Institute of Technology	Research Scholar

Scholarships: Council of Higher Education of Turkey (CoHE)-YUDAB Research Scholarship and 100/2000 CoHE Doctoral Scholarship.

Publications

1. **H. Yuce**, M. Mandal, Y. Yalcinkaya, D. Andrienko, M. M. Demir, Improvement of Photophysical Properties of CsPbBr₃ and Mn²⁺:CsPb(Br,Cl)₃ Perovskite Nanocrystals by Sr²⁺ Doping for White Light-Emitting Diodes. *J. Phys. Chem. C*. 2022. Accepted.
2. **H. Yuce**, D.K. Lafollette, M.M. Demir, C. A.R. Perini, J.-P. Correa-Baena, Effects of Alkaline Earth Metal Additives on Methylammonium-Free Lead Halide Perovskite Thin Films and Solar Cells. *Sol. RRL*, 2022, 2100999.
3. **H. Yuce**, J. Hidalgo, C.A.R. Perini, A.F. Castro-Méndez, C. Evans, P. Franco Betancur, J. N. Vagott, Y. An, K.Bairley, M.M. Demir, J.-P. Correa-Baena, Understanding the Impact of SrI₂ Additive on the Properties of Sn-based Halide Perovskites. *Opt. Mater.* 2022, 123, 111806.
4. **H. Yuce**, T. Guner, S. Dartar, B. U. Kaya, M Emrullahoglu, M. M. Demir, BODIPY-based organic color conversion layers for WLEDs. *Dyes Pigm.* 2020, 173, 107932.
5. T. Guner, **H. Yuce**, D. Tascioglu, E. Simsek, U. Savaci, A. Genc, S. Turan, M. M. Demir, Optimization and performance of nitrogen-doped carbon dots as a color conversion layer for white-LED applications. *Beilstein J. Nanotechnol.* 2019, 10, 2004.
6. **H. Yuce**, T. Guner, S. Balci, M.M. Demir, Phosphor-based white LED by various glassy particles: control over luminous efficiency. *Opt. Lett.* 2019, 44, 479.
7. **H. Yuce**, H. Alaboz, Y. Demirhan, M. Ozdemir, L. Ozyuzer, G. Aygun, Investigation of electron beam lithography effects on metal-insulator transition behavior of vanadium dioxide. *Phys. Scr.* 2017, 92, 114007.
8. H. Alaboz, Y. Demirhan, **H. Yuce**, G. Aygun, L. Ozyuzer, Comparative study of annealing and gold dopant effect on DC sputtered vanadium oxide films for bolometer applications. *Opt. Quantum Electron.* 2017, 49, 238.